Investigation of Slowing Down and Charge-Exchange of Nickel and Uranium Ions in Gases and Solids in the Energy Range (60 - 200) MeV/u

Inauguraldissertation
zur
Erlangung des Doktorgrades
der Naturwissenschaften
der Justus-Liebig-Universität Gießen
Fachbereich 07
Physik, Mathematik und Informatik, Geographie

vorgelegt von

André Fettouhi

aus Odense, Dänemark

Gießen, den 31. März 2006

Summary

In this thesis new slowing down and charge-state measurements will be presented in the energy range of (60 - 200) MeV/u. These measurements were done using the Fragment Separator (FRS) facility at GSI in Darmstadt. The presented data were taken during two experimental runs.

The experiments were divided into two parts. In the first part a 200 MeV/u Ni^{27+} beam was used. The evolution of charge states as a function of the target thickness was investigated covering both the non-equilibrium and equilibrium region. This was done with various mono-atomic materials (Z_2 = 6, 7, 10, 13, 18, 22) and compound materials (ethylene, polyethylene and polypropylene). From the measured charge-state distributions the one-electron ionization and capture cross sections have been extracted. A 40 % gas-solid difference is observed in the ionization cross sections for the mono-atomic materials. In the compound materials a 30 % difference is observed between ethylene and the polymers.

The experimental cross sections for the mono-atomic materials have been compared with theoretical calculations [1, 2]. The theoretical ionization cross sections agree quite well with the corresponding experimental ionization cross sections. In the gaseous targets the agreement between experiment and theory is better than 3 %. For the capture cross sections the agreement between experiment and theory is also very good for the lighter target materials ($Z_2 \leq 7$). For the heavier targets large deviations up to one order of magnitude are observed. These deviations are due to the increasing importance of the non-radiative capture channel in heavier target materials which is quite difficult to calculate accurately. The results motivate for further refinement of the theory in this energy region.

In the second part 3 different uranium beams were used with initial energies of 61 MeV/u (U^{86+} incident), 85 MeV/u (U^{73+} incoming) and 200 MeV/u (U^{81+} incident) to measure the evolution of the charge states again and the energy loss as a function of the target thickness in the same materials as used in the first part plus some additional mono-atomic materials Z_2 = 29, 36, 47, 54. From the measured charge-state distributions and energy losses the mean charges and stopping forces have been extracted. At 61 MeV/u we observe a gas-solid difference in the mean charge of up to 4 charge states for the mono-atomic materials. The corresponding stopping powers (forces) at the same specific energy only show a gas-solid difference for light materials ($Z_2 \leq 7$). The stopping forces are compared with calculations done with the PASS code [3, 4], ATIMA code [5] and the Hubert *et al.* tables [6]. The agreement is quite good between experiment and theory. The PASS code predicts by using the experimental mean charges a gas-solid difference in the stopping force for the heavier target materials. In the data at 200 MeV/u there is a gas-solid difference in the ionization rate for U^{81+}

ions similar to the Ni^{27+} results.

Zusammenfassung

In dieser Dissertation werden neue Ladungsverteilungen und Energieverlustmessungen präsentiert. Diese Messungen wurden am Fragment Separator (FRS) bei der GSI in Darmstadt durchgeführt. Die Daten, die hier vorgestellt werden, wurden in zwei Experimenten aufgenommen.

Die Experimente bestanden aus zwei Teilen. Im ersten Teil wurde mit einem 200 MeV/u Ni^{27+} Strahl gemessen. Ziel dieser Messung war die Entwicklung der Ladungsverteilung als Funktion der Targetdicke vom Nichtgleichgewicht bis Gleichgewicht zu untersuchen. Dies wurde mit verschiedenen Targets gemacht ($Z_2 = 6$, 7, 10, 13, 18, 22, Äthylen, Polyäthylen und Polypropylen). Von den gemessenen Ladungsverteilung konnten die Umladungsquerrschnitte für Elektroneneinfang und -verlust extrahiert werden. Ein Gas-Festkörper Effekt von 40 % wurde im Ionizationsquerrschnitt für die monoatomaren (reinen Elemente) Targets gemessen. Im Äthylen und den Polymeren (Polyäthylen und Polypropylen) war ein Effekt von 30 % zu sehen.

Die experimentellen Umladungsquerrschnitte für die monoatomaren Targets wurden mit theoretischen Rechnungen von A. Surzhykov und S. Fritzsche [1] und V. P. Shevelko [2] verglichen. In der Ionization stimmen die theoretischen Rechnungen mit den experimentellen Werten gut überein. In den Gastargets ist die Übereinstimmung besser als 3 %. Im Elektroneneinfang gibt es gute Übereinstimmung zwischen Experiment und Theorie bei den leichten Targets ($Z_2 \leq 7$), bei den schweren Targets gibt es grosse Abweichungen bis zu einer Grössenordnung. Diese Abweichung kommt zustande, weil der nicht-radiative Querrschnitt einen grösseren Anteil hat bei den schweren Targets und dieser Teil sehr schwer theoretisch zu rechnen ist. Die Ergebnisse sind eine Motivation für Verbesserungen in der Theorie im diesen Energiebereich.

Im zweiten Teil wurde ein Uranstrahl bei drei verschiedenen Energien benutzt, diese waren 61 MeV/u mit 86^+ als Eingangsladungszustand, 85 MeV/u mit 73^+ als Eingangsladungszustand und 200 MeV/u mit 81^+ als Eingangsladungszustand. Ziel dieser Messung war es wiederum, die Entwicklung der Ladungsverteilung zu untersuchen und auch Energieverluste zu messen. Dieselben Targets wurden benutzt und zusätzlich wurden folgende Targets vermessen $Z_2 = 29$, 36, 47, 54. Von den gemessenen Ladungsverteilungen und Energieverlusten wurde die mittlere Ladung und das Bremsvermögen bestimmt. Bei 61 MeV/u ist ein Gas-Festkörper Effekt in der mittleren Ladung bei den monoatomaren Targets zu sehen. Der Effekt hat eine Grösse von fast 4 Ladungen. Das dazu gehörige Bremsvermögen zeigt nur einen Gas-Festkörper Effekt bei den leichteren Targets ($Z_2 \leq 7$). Die experimentellen Werte wurden mit dem PASS Programm [3, 4], dem ATIMA Programm [5] und den Hubert *et al.* Tabellen [6] verglichen. Die theoretischen Rechnungen von den Programmen stimmen mit den experimentellen Werten gut überein. PASS sagt einen Gas-Festkörper Effekt bei den

schwereren Targets voraus, weil experimentelle Ladungen als Eingangsparameter benutzt wurden. Bei der 200 MeV/u Messung wurde ein Gas-Festkörper Unterschied in der Ionizationsrate in der Entwicklung des U^{81+} Ladungszustand beobachtet, ähnlich wie in der Ni^{27+} Messung.

Contents

Chapter 1

Introduction

1.1 Ion Penetration Through Matter

It has been a longstanding tradition at GSI to measure energy loss of heavy ions. The initial work started in the end of 1970's using the newly build (at that time) UNILAC accelerator. In the early 1980's the systematic studies led to the discovery of the gas-solid effect in the stopping force [7], three decades after the effect was discovered in the mean charge by Lassen [8]. These studies covered an projectile energy range from 0.1 - 10 MeV/u. The discovery of the gas-solid effect in the stopping force led to even more studies of the effect at even higher energies which were done in the late 1980's and early 1990's [9] at the GANIL facility in France.

With the advent of the Heavy-Ion Synchrotron (SIS) and Fragment Separator (FRS) in the early 1990's at GSI it became possible to measure energy losses at beam energies up to 1 GeV/u. New studies done at these high energies showed that the Bethe-Bloch formula [10, 11] is insufficient to describe the stopping force of heavy ions. This discovery led to the development of the Lindhard-Sørensen theory [12] in 1996. Since then more systematic studies have been done covering the energy range 100 - 1000 MeV/u for various heavy projectiles and targets [13, 14, 15]. Figure 1.1 displays the experimental stopping forces that have been measured at GSI and GANIL over the last 3 decades plotted versus the projectile atomic number. The high energy region (above 100 - 200 MeV/u) has been well covered and similar is seen for energies below 50 - 100 MeV/u. But measurements with heavy projectiles such as uranium in the energy region 50 - 200 MeV/u are missing. This is the main motivation of this thesis to measure energy losses of heavy ions in that region. The red dots display the new experimental stopping forces which have been obtained. The last extensive investigation of the gas-solid effect in the stopping force was done at roughly 20 MeV/u in the case of uranium ions by Bimbot and coworkers [9]. With the Fragment Separator it is possible to measure both charge state distribution and energy loss at the same time. This can help in understanding the gas-solid effect in the stopping force in more detail plus it allows testing of the scaling properties of the stopping force.

Measuring the evolution of charge state distributions can give information about a more basic quantity namely the charge-exchange cross sections. If there is gas-solid effect in the charge state distribution then there is a gas-solid effect in the charge-exchange cross sections. In order to extract the cross sections from charge state mea-

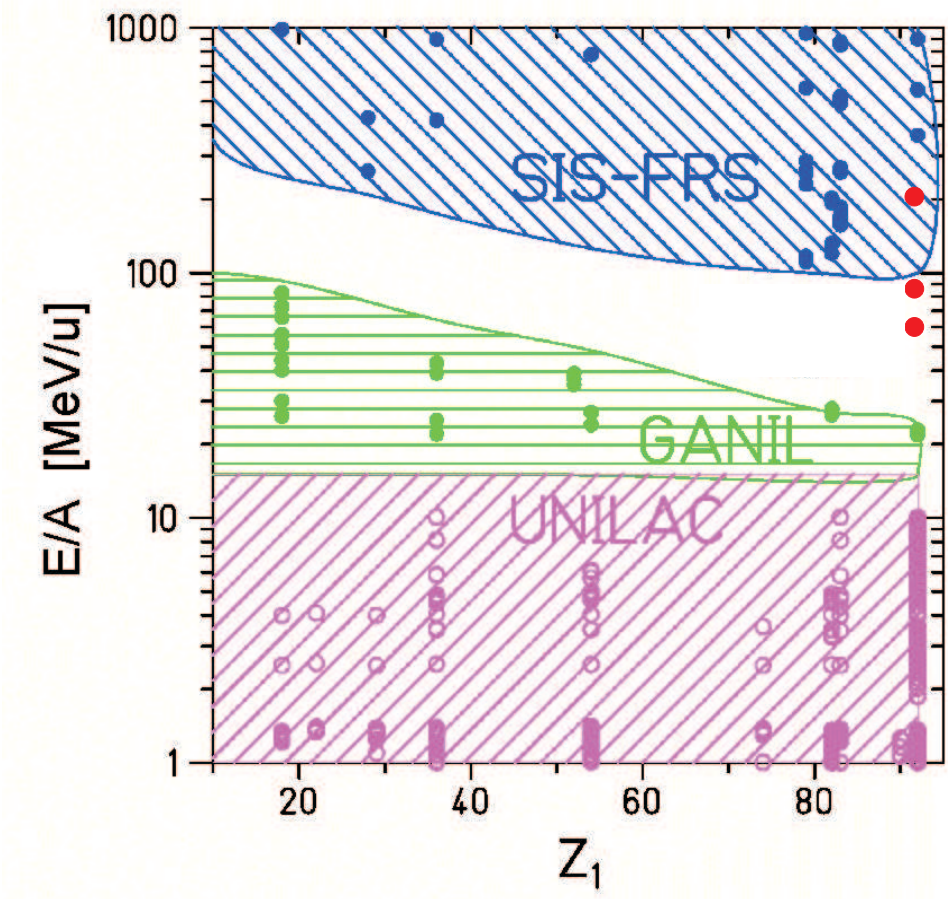

Figure 1.1: Experimental stopping forces measured at the UNILAC and with the FRS facility at GSI in Darmstadt and at GANIL in France versus the projectile atomic number. The red dots display the experimental stopping forces presented in this thesis.

surements one has to measure the whole distribution from the non-equilibrium to the equilibrium region. Measurement of the non-equilibrium is very difficult because very thin foils are needed (in the case of solids) depending on the projectile energy and target material. Woods and coworkers [16] did investigations in different compound materials with a 36 MeV carbon beam and they observed a gas-solid difference in the cross sections derived from the charge state measurements.

The goal of this thesis is to extend the gas-solid effect measurements in the stopping force done by Geissel *et al.* [7] and Bimbot *et al.* [9] to higher energies plus to do charge state measurements in order to investigate the charge-exchange cross sections in this energy region.

Chapter 2

Theory

2.1 Slowing Down Theory

2.1.1 Definition

In the following discussion [17] we assume that the penetrating particle is always moving with a velocity greater than the Bohr velocity v_0. The term stopping force will be used throughout the thesis for describing the energy loss per unit length dE/dx. Consider a homogeneous stopping medium with a thickness x. Let a projectile penetrate the medium with an energy E. We wish to determine the energy loss ΔE of the projectile when it has penetrated a layer of thickness Δx. Assuming that the projectile loses energy in discrete bits T_j, with $j = 1, 2, \ldots$ and $T_j \ll E$, the energy loss can then be written as

$$\Delta E = \sum_j n_j T_j, \tag{2.1}$$

where n_j is the number of collisions of type j, each leading to an energy loss of T_j.

The above argument considered only one projectile. Let us now consider multiple projectiles. The average energy loss $\langle \Delta E \rangle$ is then given by

$$\langle \Delta E \rangle = \sum_j \langle n_j \rangle T_j. \tag{2.2}$$

Then the average number of events is given by

$$\langle n_j \rangle = N \Delta x \sigma_j, \tag{2.3}$$

N is the density of the medium and σ_j is the 'energy loss cross section'. Combining (2.2) and (2.3) yields

$$\langle \Delta E \rangle = N \Delta x \sum_j T_j \sigma_j. \tag{2.4}$$

Now we define the stopping cross section S as

$$S = \sum_j T_j \sigma_j, \tag{2.5}$$

the stopping force is then

$$\frac{\langle \Delta E \rangle}{\Delta x} = N \sum_j T_j \sigma_j. \tag{2.6}$$

Going over to the case of continuous energy loss in individual encounters, we may replace

$$\sigma_j = \frac{d\sigma(T)}{dT} \Delta T_j. \tag{2.7}$$

Letting the size of ΔT_j be sufficiently small, the sum in (2.6) can be replaced by an integral (continuous slowing down approximation) and one arrives at

$$\begin{aligned} -\frac{dE}{dx} &= N \int T d\sigma \\ &= NS. \end{aligned} \tag{2.8}$$

The added minus sign signals that the projectile energy decreases.

The energy loss of the projectile can be deposited either in the target electrons or nucleus. This means that we can write the stopping cross section as

$$S = S_e + S_n. \tag{2.9}$$

S_e is the electronic stopping cross section and S_n is the elastic stopping cross section. Elastic stopping becomes important when $v < v_0$. For that reason we neglect this contribution to the nucleus.

2.1.2 Slowing Down in a Coulomb Field

Assume an electron initially at rest and a projectile ($Z_1 > 2$) moving with a velocity v. From classical scattering theory one can derive an expression for the energy transferred to the electron (for $v \ll c$)

$$T = 2m_e v^2 \sin^2\left(\frac{\Theta}{2}\right), \tag{2.10}$$

Θ is the scattering angle in the center-of-mass frame and m_e is the mass of the electron. For $\Theta = \pi$ we have a maximum energy transfer of $2m_e v^2$. The scattering angle and the impact parameter p (perpendicular distance between projectile and target, see Figure 2.1) are related to each other through the following equation [17]

$$\tan\left(\frac{\Theta}{2}\right) = \frac{b}{2p}, \tag{2.11}$$

where $b = 2|Z_1| e^2/m_e v^2$ is the distance of closest approach (collision diameter), Z_1 is the projectile atomic number. Figure 2.1 below demonstrates the connection between the differential cross section and the impact parameter. Because of the azimuthal symmetry we get

$$d\sigma = 2\pi p dp \tag{2.12}$$

$$= \left|\frac{d(\pi p^2)}{dT}\right| dT \tag{2.13}$$

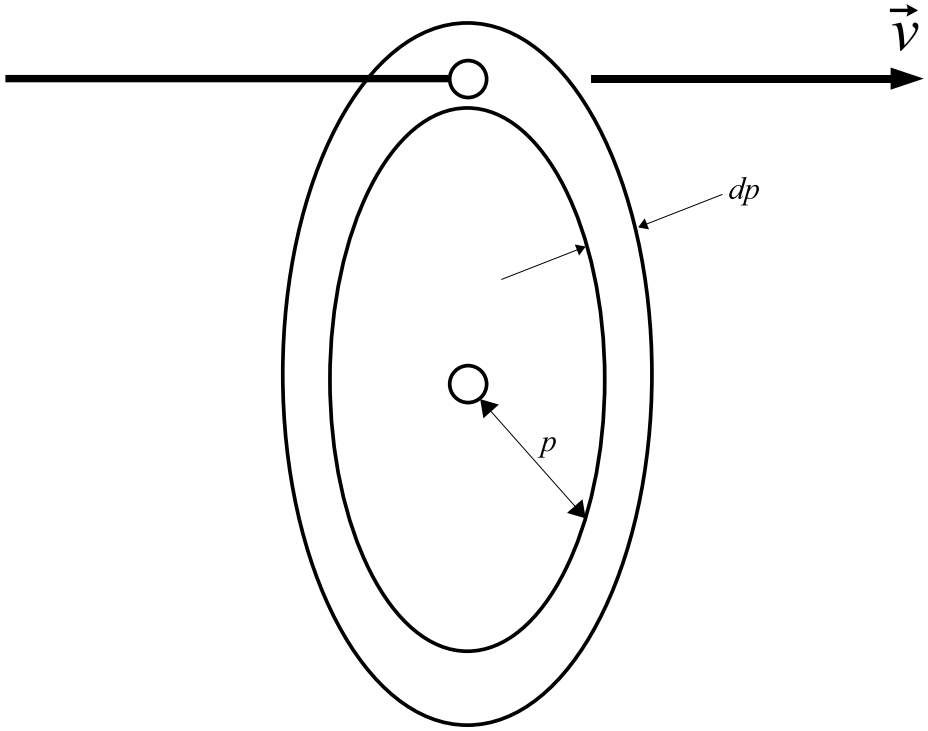

Figure 2.1: Definition of differential cross section $d\sigma$ and impact parameter p [17].

Inserting (2.11) into (2.10) gives Thomson's formula [18]

$$T_{\text{free}} = \frac{2m_e v^2}{1+(2p/b)^2}. \tag{2.14}$$

The differential cross section is found by inverting and differentiating equation (2.14) and using (2.13). The result is

$$d\sigma_R = \frac{2\pi Z_1^2 e^4}{m_e v^2}\frac{dT}{T^2}. \tag{2.15}$$

The above formula is Rutherford's scattering law (though not in standard notation) and the stopping cross section is then

$$S_e = \frac{2\pi Z_1^2 e^4}{m_e v^2}\int_0^{2m_e v^2}\frac{dT}{T}. \tag{2.16}$$

Equation (2.14) has a singularity that arises from ignoring the binding of the electron. A simple solution suggested by Thomson [18] was to introduce a cutoff and setting that equal to the lowest ionization energy. This suggestion leads to a stopping force that is a factor 2 too small. It was Bohr [19] who later solved this problem. Bohr used the classical harmonic oscillator to describe the binding of the electron to the nucleus. This led Bohr to divide the interaction into close collisions (large momentum transfer) and distant collisions (small momentum transfer).

When an external force F acts on an oscillator during a limited time period τ, the exchange of momentum depends essentially on the magnitude of τ compared to the

oscillation period $2\pi/\omega$, where ω is the resonance frequency of the oscillator. When $\tau \ll 2\pi/\omega$, the oscillator takes up a momentum of $F \cdot \tau$ as if it were a free particle, thereby making equation (2.13) valid. For $\tau \gg 2\pi/\omega$, the oscillator will respond adiabatically to the external force and it will calm down as the disturbance vanishes. Thus, the takeup of momentum will be much smaller than that experienced by a free particle. The collision time for free Coulomb scattering is roughly $\tau \sim 2p/v$. The adiabatic cutoff will occur at an impact parameter where $2p/v \ll 2\pi/\omega$, i.e.

$$a_{ad} \sim \frac{v}{\omega}. \tag{2.17}$$

This quantity is known as Bohr's adiabatic radius.

2.1.3 Energy Loss due to Bound Electrons

As mentioned above Bohr used the harmonic oscillator in an electric field to investigate the energy transfer for distant collisions. The electric field is given by

$$\mathbf{E}(\mathbf{r},t) = -\nabla\Phi(\mathbf{r},t) \tag{2.18}$$

where Φ is the Coulomb potential, i.e.

$$\Phi(\mathbf{r},t) = \frac{Z_1 e}{|\mathbf{r}-\mathbf{R}(t)|}. \tag{2.19}$$

$\mathbf{R}(t)$ is the trajectory of the projectile

$$\mathbf{R}(t) = \mathbf{p} + \mathbf{v}t, \tag{2.20}$$

where $\mathbf{p}$ is the impact parameter (vector). For a classical electron bound by a force $-k\mathbf{r} = -m_e\omega^2\mathbf{r}$ the classical equation of motion is given by

$$\frac{d^2\mathbf{r}}{dt^2} + \omega^2\mathbf{r} = -\frac{e}{m_e}\mathbf{E}(\mathbf{r},t), \tag{2.21}$$

the energy transfer to a classical harmonic oscillator is the sum of the kinetic energy and potential energy which is given by

$$\begin{aligned} T_{\text{oscillator}} &= T_{kin} + T_{pot} \\ &= \frac{1}{2}m_e v^2 + \frac{1}{2}m_e\omega^2 r^2 \\ &= \frac{e^2}{2m_e}\left|\int_{-\infty}^{\infty} dt\mathbf{E}(t)e^{i\omega t}\right|^2 \\ &= \frac{2\pi^2 e^2}{m_e}\left|\mathbf{E}(\omega)\right|^2. \end{aligned} \tag{2.22}$$

The above equation still contains the unknown function $\mathbf{r}(t)$ (solution to equation (2.21)). We are interested in the energy transfer by the harmonic oscillator for distant collisions (weak interaction). The simplest approximation is to ignore all displacements, i.e. assuming that the electric field only depends on time and not displacement

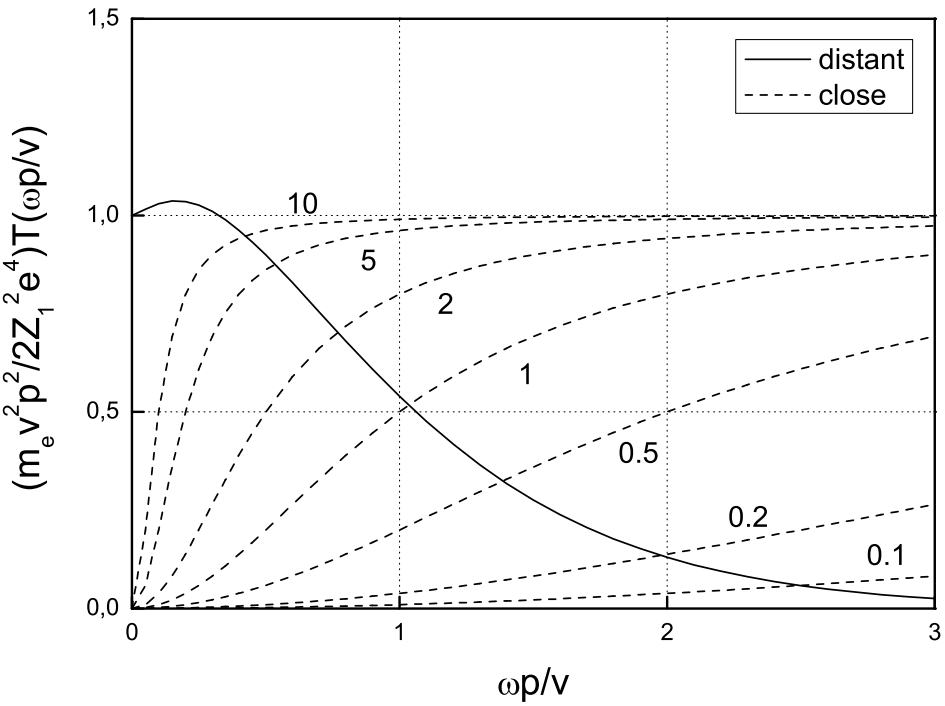

Figure 2.2: Energy transfer functions T_{free} (2.14) for $\xi = 0.1$ up to $\xi = 10$ and T_{bound} (2.24) versus the ratio $\omega p/v$ [22]. For large ξ T_{free} and T_{bound} can be smoothly connected.

$\mathbf{E}(\mathbf{r}(t), t) \simeq \mathbf{E}(t)$. By using the Fourier transform of the Coulomb potential (2.19) and equation (2.18) one finds in the case of weak interaction the Fourier component of the electric field to be

$$\mathbf{E}(\omega) = -\frac{Z_1 \omega}{\pi v^2}\left(iK_0\left(\frac{\omega p}{v}\right), K_1\left(\frac{\omega p}{v}\right), 0\right), \tag{2.23}$$

K_0 and K_1 are modified Bessel functions [20]. From the electric field we get the energy transfer

$$T_{\text{bound}} = \frac{2Z_1 e^4}{m_e v^2 p^2}\left(\left[\frac{\omega p}{v}K_0\left(\frac{\omega p}{v}\right)\right]^2 + \left[\frac{\omega p}{v}K_1\left(\frac{\omega p}{v}\right)\right]^2\right). \tag{2.24}$$

For large impact parameters T_{bound} goes towards zero in accordance with Bohr's adiabatic limit (2.17). Now we just need to carry out the remaining integral over all impact parameters, i.e.

$$S = \int 2\pi p\, dp T(p). \tag{2.25}$$

In figure 2.2 [22] we have plotted T_{free} and T_{bound} versus ratio $\omega p/v$. The function $(m_e v^2 p^2/2Z_1^2 e^4)T_{\text{bound}}$ is an universal function of $\omega p/v$, while $(m_e v^2 p^2/2Z_1^2 e^4)T_{\text{free}}$ depends on $\xi = m_e v^3/Z_1 e^2 \omega$. The figure suggests to split the integration into two parts at the intersection p_0, where $T_{\text{free}}(p_0) = T_{\text{bound}}(p_0)$. For sufficient large ξ the result must be independent of p_0 since both functions are ~ 1 over a comfortable interval. So

we get for the close collisions

$$\begin{aligned} S_{\text{free}} &= \int_0^{p_0} 2\pi p\, dp\, T_{\text{free}}(p) \\ &= \frac{2\pi Z_1^2 e^4}{m_e v^2} \ln\left(1 + \frac{4p_0^2}{b^2}\right), \end{aligned} \tag{2.26}$$

for distant collisions one finds with the help of partial integration and that $K_1(x) = -dK_0(x)/dx$ [20]

$$\begin{aligned} S_{\text{bound}} &= \int_{p_0}^{\infty} 2\pi p\, dp\, T_{\text{bound}}(p) \\ &= \frac{4\pi Z_1^2 e^4}{m_e v^2} \left(\frac{\omega p_0}{v}\right) K_0\left(\frac{\omega p_0}{v}\right) K_1\left(\frac{\omega p_0}{v}\right). \end{aligned} \tag{2.27}$$

Combining the two results and assuming that we are dealing with swift ions ($v \gg v_0$), we can use the asymptotic relations of the Bessel functions [20] for small arguments and then find Bohr's stopping formula

$$S = \frac{4\pi Z_1^2 e^4}{m_e v^2} \ln\left(\frac{C m_e v^3}{|Z_1|\, e^2 \omega}\right), \tag{2.28}$$

where $C = 2e^{-2\gamma} = 1.1229$. To determine the stopping force for an ion interacting with a target atom we need to sum over all target electrons (frequencies) weighted with their dipole oscillator strength f_j (quantum mechanical contribution) [21]

$$-\frac{dE}{dx} = \frac{4\pi Z_1^2 e^4}{m_e v^2} Z_2 N \sum_j f_j \ln\left(\frac{C m_e v^3}{|Z_1|\, e^2 \omega_j}\right) \tag{2.29}$$

$Z_2 N$ is the electron density of the target medium and the oscillator strengths are normalized to $\sum_j f_j = 1$. The above equation is Bohr's stopping formula in modern notation.

2.2 Binary Theory

The main problem of dividing into close and distant collisions is that these two regions do not join smoothly for all values of $\omega p/v$. For values $\omega p/v < 1$ (see figure 2.2) it is risky to interpolate and will most likely lead to significant errors. This has caused serious problems in the classical theory of the Barkas-Andersen effect [23]. The Barkas-Andersen effect is the difference in the stopping force between a particle and its antiparticle (will be discussed in detail later). Initial theoretical treatments [24, 25] of this effect neglected the close-collision regime. Lindhard derived a result for the close-collision regime [26] using dimensional arguments. A recent reinvestigation of the Barkas-Andersen effect [27] showed that without proper interpolation the Barkas-Andersen effect may grow as large as the leading terms in the stopping force. This indicates that an alternative approach is needed to describe the Barkas-Andersen effect correctly.

One alternative is a binary collision picture with an effective Coulomb potential [3]. The argument for using such an approach is quite simple. In the Bohr model the projectile-target interaction is described by Rutherford's law, truncated at impact parameters beyond the adiabatic radius a_{ad}. A mathematical interpretation of this could be an effective potential of the form

$$V_{\text{eff}}(r) = -\frac{Z_1 e^2}{r} e^{-r/a_{ad}}. \tag{2.30}$$

The choice of a Yukawa potential was justified by Lindhard [26] in the case of an electron gas. The potential corresponds to a dynamical screening by the electron gas extended over an area of a_{ad}. A remarkable feature of this potential is that one can reproduce the second part of the Bohr result for distant collisions T_{bound} (2.24). In a binary collision the momentum transfer is given by $P_\perp(p,v) = m_e v\theta(p,v)$ (perpendicular to the beam) in the small-angle approximation. The c.m.s. scattering angle θ, with the effective potential given above, is [28]

$$\theta(p,v) = -\frac{2Z_1 e^2}{a_{ad} m_e v} K_1\left(\frac{p}{a_{ad}}\right). \tag{2.31}$$

From this follows directly the energy transfer

$$T_\perp(p,v) = \frac{2Z_1^2 e^4 \omega^2}{m_e v^4}\left[K_1\left(\frac{p}{a_{ad}}\right)\right]^2, \tag{2.32}$$

which is identical to the second part of equation (2.24). The first part of eq. (2.24) has no direct analogue in binary scattering, but it represents the energy transfer $T_\parallel(p,v)$ along the beam. Nevertheless we wish to determine its magnitude, for this we need to return to the physical origin of that term. Figure 2.3 shows the electron trajectory following a distant collision. Due to the two Bessel functions entering in equation (2.24) the asymptotic orbit will be elliptical. Since the potential is harmonic $T_\parallel(p,v)$ may alternatively be expressed as the potential $(1/2)m\omega^2 r_0(p,v)^2$ at a distance

$$r_0(p,v) = \frac{2Z_1 e^2}{m_e v^2} K_1\left(\frac{\omega p}{v}\right) \tag{2.33}$$

from the origin. Note that the electron has received an angular momentum of

$$J(p,v) = r_0(p,v) P_\perp(p,v). \tag{2.34}$$

Now in figure 2.4 the same process is illustrated in the binary-scattering picture (not limited to the small-angle approximation). The electron has received momentum $2m_e v \sin(\theta(p,v)/2)$ and angular momentum

$$J(p,v) = 2m_e r_{\text{eff}}(p,v) v \sin\left(\frac{\theta(p,v)}{2}\right), \tag{2.35}$$

where $r_{\text{eff}}(p,v)$ is the asymptotic impact parameter in the laboratory frame. Sigmund [3] has shown that $r_{\text{eff}}(p,v)$ is given by

$$r_{\text{eff}}(p,v) = 2\tau(p,v)\cos\left(\frac{\theta(p,v)}{2}\right) - 2p\sin\left(\frac{\theta(p,v)}{2}\right), \tag{2.36}$$

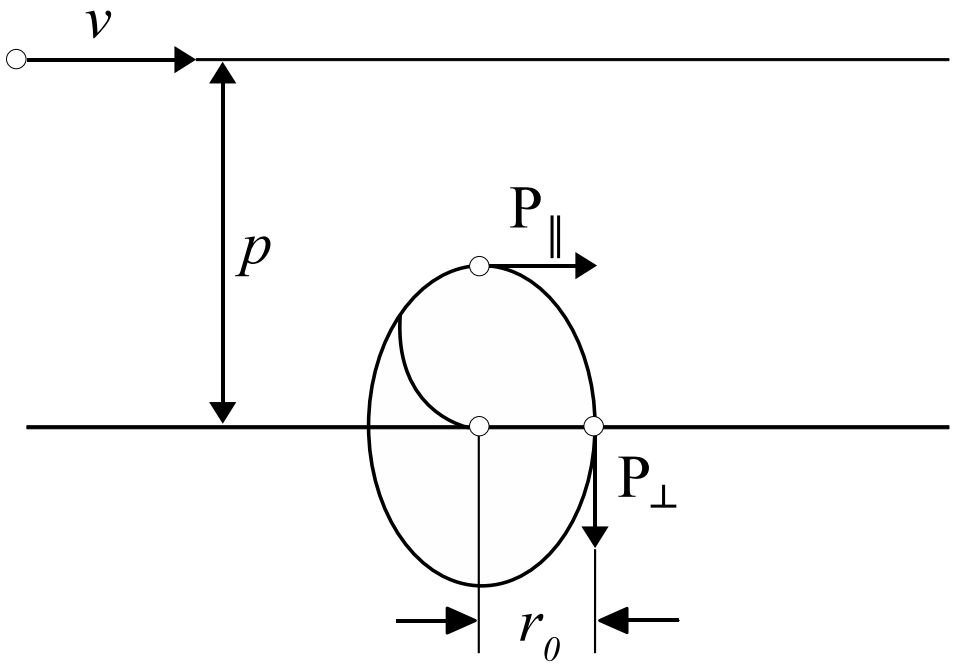

Figure 2.3: Orbit of an excited target electron in the Bohr model [3].

where $\tau(p,v)$ is the time integral [29, 30] given by

$$\begin{aligned}\tau(p,v) &= \sqrt{r_m^2-p^2}-\int_{r_m}^{\infty}dr \\ &\quad\times\left(\frac{1}{\sqrt{1-2V_{\rm eff}(r)/m_ev^2-p^2/r^2}}-\frac{1}{\sqrt{1-p^2/r^2}}\right),\end{aligned} \tag{2.37}$$

with r_m defined as the root of $1-2V_{\rm eff}(r)/m_ev^2-p^2/r^2=0$. Within first-order perturbation theory Sigmund [3] has shown that equation (2.36) reduces to (2.33). Thus the screened Coulomb potential reproduces the predictions of Bohr for distant collisions for $T_\perp(p,v)$ and $J(p,v)$ through $r_{\rm eff}(p,v)$. This defines a procedure to specify the potential energy transfer in the binary collision picture by adding the extra term

$$W_0(p,v) = \frac{1}{2}m_e\omega^2 r_{\rm eff}(p,v)^2 \tag{2.38}$$

to the kinetic-energy transfer. The above term reduces to $T_\parallel(p,v)$ in the limit of distant collisions. So the total energy transfer is given by

$$T(p,v) = 2m_ev^2\sin^2\left(\frac{\theta(p,v)}{2}\right)+\frac{1}{2}m_e\omega^2 r_{\rm eff}(p,v)^2. \tag{2.39}$$

In the limit of close collisions (large momentum transfer) the above equation reduces to the Rutherford result ($T=2m_ev^2$). This can be seen by setting $p=0\Rightarrow\theta=\pi$, this yields by insertion into equation (2.38) $r_{\rm eff}(0,v)=0$ and hence the potential-energy term vanishes. A small correction needs to be added, for intermediate impact

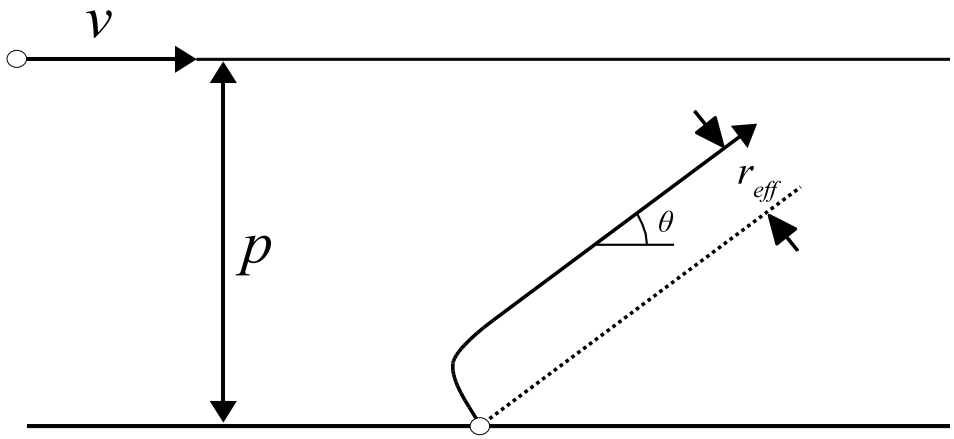

Figure 2.4: Orbit of an excited target electron in the binary-scattering model [3].

parameters the potential-energy transfer $W_0(p,v)$ can exceed the ionization energy. This unphysical behavior can be removed by the *ansatz*

$$\frac{1}{W(p,v)} = \frac{1}{W_0(p,v)} + \frac{1}{U}, \tag{2.40}$$

where U is the ionization energy. Then the total energy transfer becomes

$$T(p,v) = 2m_e v^2 \sin^2\left(\frac{\theta(p,v)}{2}\right) + W(p,v). \tag{2.41}$$

Now we have an equation (no perturbation expansion employed so higher order terms in Z_1 are taken into account) for determining the energy transfer that smoothly connects close and distant interactions by the use of an effective potential. In both limits the Bohr results are derived.

2.2.1 Screening

So far we have been dealing with fully stripped ions. In most experiments the projectile ions are not fully stripped. This requires taking projectile screening into account. Bohr showed in his famous monograph [31] that screening is important when $v \leq Z_1^{2/3} v_0$. In the extended Bohr theory developed by Sigmund [32] the following interaction potential was employed

$$V(r) = -\frac{q_1 e^2}{r} - \frac{(Z_1 - q_1)e^2}{r} e^{-r/a_s}, \tag{2.42}$$

where $q_1 e$ is the ion charge and a_s is the screening radius. The above potential was originally proposed by Brandt and Kitagawa [33]. The following screening radius is used (differs from [33])

$$a_s = \left(1 - \frac{q_1}{Z_1}\right)^r a_{TF} \tag{2.43}$$

with the Thomas-Fermi radius $a_{TF} = 0.8853 a_0 / Z_1^{1/3}$ of a neutral projectile atom, r is a numerical coefficient often set equal to 1 [32].

Using the above potential (2.42) within the binary theory yields the following effective potential

$$V_{\text{eff}}(r) = -\frac{q_1 e^2}{r} e^{-r/a_{ad}} - \frac{(Z_1 - q_1)e^2}{r} e^{-r/a} \tag{2.44}$$

with

$$\frac{1}{a^2} = \frac{1}{a_{ad}^2} + \frac{1}{a_s^2}. \tag{2.45}$$

The qualitative grounds for such an *ansatz* were argued by Schinner and Sigmund [3, 4].

Mean Equilibrium Charge

Ions interacting with matter do not have one fixed charge when exiting the matter, they form a charge state distribution. A simple way to include the charge state distribution into the stopping force calculations is to replace replace q_1 with the mean equilibrium charge $\langle q_1 \rangle$. Several models/fit functions exist for $\langle q_1 \rangle$, the simplest being the Thomas-Fermi formula

$$\langle q_1 \rangle = Z_1 \left(1 - e^{-v/Z_1^{2/3} v_0}\right). \tag{2.46}$$

For light projectiles the formula has proven to be very useful [3, 4].

2.2.2 Shell Corrections

When the velocity of the projectile becomes sufficiently small one has to consider the motion of the target electron during the collision. The effect becomes important when $v < Z_2^{2/3} v_0$. Sigmund [34] has shown that for binary collisions, shell corrections can be included by performing the following integration

$$S_j(v) = \int d^3 v_e f_j(\mathbf{v}_e) \frac{\mathbf{v} \cdot (\mathbf{v} - \mathbf{v}_e)}{v|\mathbf{v} - \mathbf{v}_e|} S_{0j}(|\mathbf{v} - \mathbf{v}_e|), \tag{2.47}$$

where $S_{0j}(v)$ is the stopping cross section for a stationary target electron in the jth shell or subshell, $f_j(\mathbf{v}_e)$ is the velocity distribution of the electrons in the jth shell or subshell. The above equation states that the only knowledge needed to incorporate shell corrections is the velocity distribution of target electrons. These can be obtained from Fourier transformation of the wave functions. Shell corrections in the Bethe and Bohr model have been derived by Walske [35, 36] and Sigmund [37], respectively using higher-order perturbation theory.

2.2.3 Barkas-Andersen Effect

As previously mentioned the Barkas-Andersen effect is the difference in the stopping force of a projectile ion its corresponding anti-ion. Within the basic Bethe [21] and Bohr (2.28) theory this difference is not accounted for because of the strict proportionality

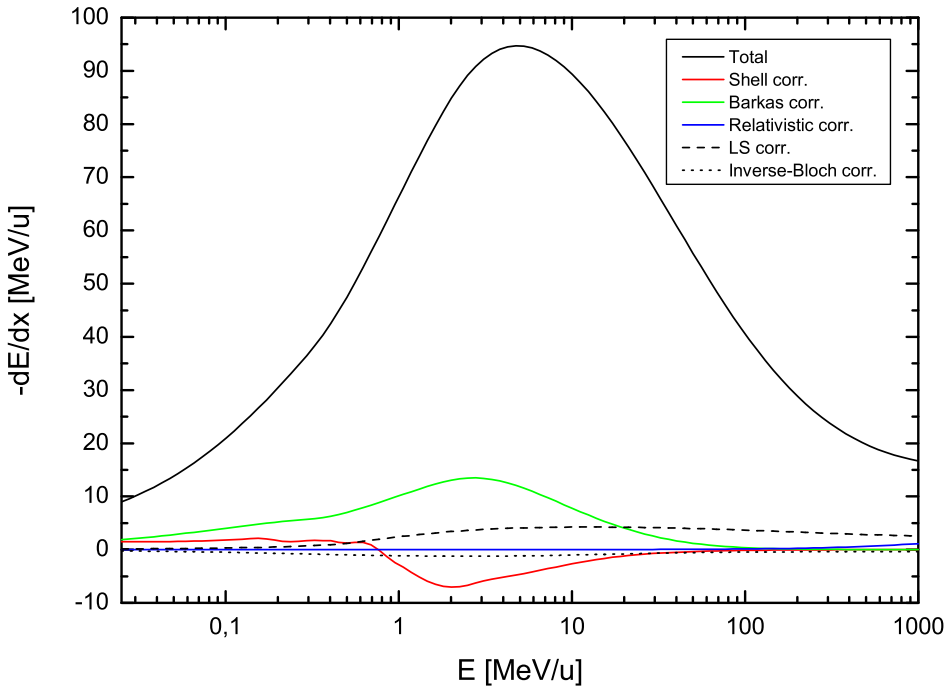

Figure 2.5: Theoretical stopping force of uranium ions in aluminum (solid curve) calculated with the PASS code. The colored curves show the contributions from shell, Barkas-Andersen and relativity corrections, respectively. The dashed and dotted curves are contributions from the LS [12] and inverse-Bloch [22] corrections, respectively.

to the square of the projectile charge in the stopping force. The effect was discovered by Smith and coworkers [23] for mesons and subsequent work by the same qroup which demonstrated deviations from this strict proportionality to the square of the charge. The phenomenon was ascribed to higher-order perturbations and quantified by a contribution proportional to the third power of the charge of the penetrating particle. This contribution was later verified by Andersen *et al.* [38] for protons, alpha particles and lithium ions. Theoretical calculations of the Barkas-Andersen effect (classical and quantum mechanical [24, 39, 40]) have been based on extensions of the perturbation approaches by Bethe and Bohr in order to include terms proportional to Z_1^3. It was believed that the effect arised because of the relaxation of the target electron during the interaction with the projectile ion. Hence, the effect must mainly come from distant collisions where binding is important. For close collisions, where the binding can safely be ignored, the Barkas-Andersen must vanish. It was long discussed how to accurately determine the Barkas-Andersen effect for close collisions [24, 26]. Lindhard's suggestion [26] viewing the Barkas effect as an deviation from free-Coloumb scattering provided a key to quantitatively determine effect independent of the impact parameter. The binary theory does not involve an expansion in Z_1, neither is the term close and distant interaction used because the binding of the target electron has been replaced by screening. Hence the Barkas-Andersen effect is well approximated for all impact parameters. Application of the binary theory has shown that the Barkas-Andersen effect is larger for protons than heavier ions [41]. The magnitude of the Barkas-Andersen effect is shown in figure 2.5 for the case of uranium ions penetrating

aluminum.

2.2.4 PASS Code

The PASS code has been developed by Schinner and Sigmund and is the numerical implementation of the binary theory plus shell corrections [34], Bethe relativity correction [42], LS correction [12] and the inverse-Bloch correction [22] which is by given

$$-\Delta\left(\frac{dE}{dx}\right) = \frac{4\pi Z_1^2 Z_2 e^4}{m_e v^2} N \sum_j f_j \left[\ln\left(\frac{|Z_1|\, e^2\omega_j}{\hbar v}\right) - \Re\psi\left(1 + i\frac{Z_1 e^2}{\hbar v}\right)\right] \quad (2.48)$$

where $\psi(\zeta) = d\ln\Gamma(\zeta)/d\zeta$ logarithmic derivative of the gamma function [20]. The code evaluates the stopping number L as a function of the Bohr variable $\xi = m_e v^3/|Z_1|e^2\omega$. Shell corrections are calculated as given by (2.47). An efficient procedure was developed to economize the computation of the shell corrections (see [4] for further details). There are two different types of wave functions available in the PASS code, hydrogen-like or Hartree-Fock [43, 44]. The following corrections are available as options in PASS, the inverse-Bloch correction [22] which extends the binary theory into the Bethe region, the relativity correction [42] and finally the LS correction [12] (only for pointlike nuclei). The magnitude of these effects is illustrated above in figure 2.5. Projectile excitation is treated as explained by Sigmund [32], two different schemes are available (see [4] for details). The mean equilibrium charge is calculated by the Thomas-Fermi formula. As a second option a modified Thomas-Fermi formula is included

$$\langle q_1\rangle = Z_1\left(1 - e^{-Av/Z_1^{0.45}v_0}\right)^C \quad (2.49)$$

with parameters A and C that can be adjusted to each projectile-target combination. Frozen charge can also be chosen. Capture and loss contributions are also added according to [45]. One can add the capture or loss contributions as a separate option or together as one option.

The PASS code has been written in FORTRAN 77, CPU time is roughly 70 seconds per shell for 100 data points for the energy of the projectile ion on a 1.7 GHz PC. The computation times are governed mainly by the number of target and projectile shells to be treated.

Input

For each projectile-target combination a database is set up that holds the information for f_j, ω_j and U for each shell or subshell. The pairs of (f_j, ω_j) are extracted from various tables [46, 47, 48, 49]. Reference [46] is an electronic database (CD-ROM) of measured complex refractive indexes $\mathtt{n}(\omega) + i\,\mathtt{k}(\omega)$ (ω is the excitation frequency) for a large number of solids in the periodic table plus a small collection compounds. The database covers roughly excitation energies $E = \hbar\omega$ from 0.01 eV up to 10 keV.

In general the sum of dipole oscillator strengths f_j appearing in the Bohr (2.29) and Bethe formula [21] is replaced by an integral over a continuous spectrum of dipole oscillator strengths $f'(\omega)$ which is related to the dielectric function $\varepsilon(\omega)$

$$f'(\omega) = -\frac{2\epsilon_0 m}{\pi n_e e^2}\omega\Im\frac{1}{\varepsilon(\omega)}, \quad (2.50)$$

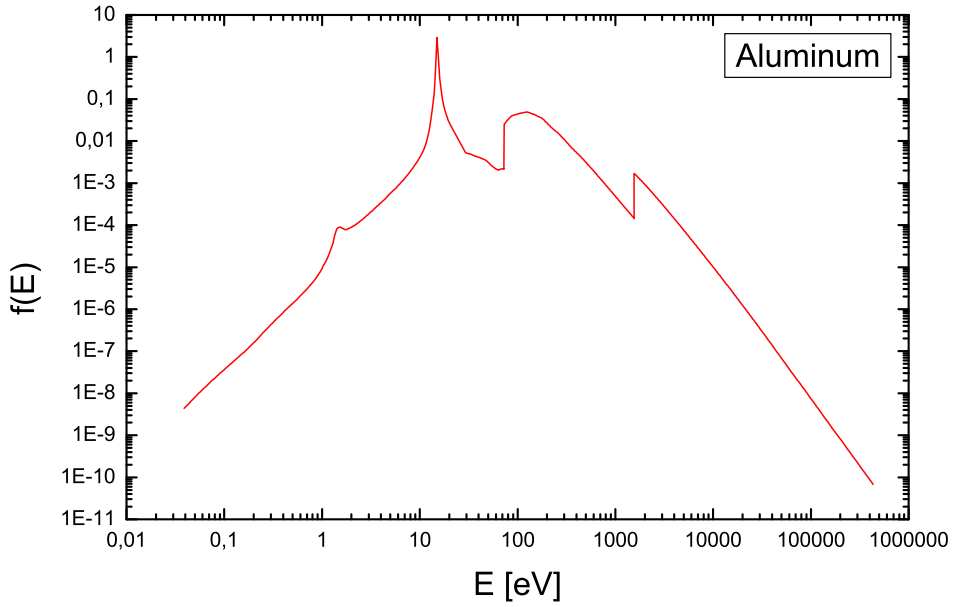

Figure 2.6: Oscillator strength spectrum as a function of the excitation energy $E = \hbar\omega$ for aluminum. The peak at 15 eV represents the plasma frequency ω_p.

where $\Im$ denotes the imaginary part,

$$\int_0^\infty d\omega f'(\omega) \quad = \quad 1, \tag{2.51}$$

and $n_e = nZ_2$ is the number of electrons per volume. Since $\varepsilon(\omega)$ can be expressed by the complex refractive index $\mathtt{n}(\omega) + i\,\mathtt{k}(\omega)$, the oscillator strength spectrum may be written in the form

$$f(\hbar\omega) \quad = \quad 1.5331 \cdot 10^{-3} \frac{A_2}{\rho} \frac{\hbar\omega \mathtt{nk}}{(\mathtt{n}^2 + \mathtt{k}^2)^2} \tag{2.52}$$

where ρ is the density in g/cm^3; $\hbar\omega$ is in eV; $f(\hbar\omega)$ is in eV^{-1} with the normalization

$$\int_0^\infty d(\hbar\omega) f(\hbar\omega) \quad = \quad Z_2. \tag{2.53}$$

The function f differs only from f' by the normalization. With the database from Palik [46] and equation (2.52) one can then construct the oscillator strength spectrum, such a spectrum is shown above in the case of aluminum. Since reference [46] only covers the excitation spectrum up to 10 keV other sources need to be considered. Henke *et al.* [47] have published a large database of complex atomic scattering factors $f = f_1 + if_2$ for 94 elements covering excitation frequencies from 30 eV up to 30 keV. The atomic scattering factor is defined by

$$\mathcal{E} \quad = \quad \mathcal{E}_e(f_1 + if_2) \tag{2.54}$$

where $\mathcal{E}$ is the amplitude scattered by the atom and $\mathcal{E}_e$ is the amplitude that would be scattered if the atom were replaced by a single, free Thomsonian electron. The

atomic scattering factors are derived from quantum dispersion relations from photo-absorption data (see [47]). The complex refractive index and atomic scattering factor are connected in the following way

$$\begin{aligned} \mathtt{n}(\omega) + i\,\mathtt{k}(\omega) &= (1-\delta) - i\beta \\ &= 1 - \frac{r_0}{2\pi}\lambda^2 N(f_1 + if_2), \end{aligned} \tag{2.55}$$

where λ is the wavelength, N is the number of atoms per volume and r_0 is the classical K-shell radius e^2/mc^2; f_1 and f_2 are the real and imaginary part of the atomic scattering factor. Similarly one can derive the oscillator strength spectrum

$$f(\hbar\omega) = \frac{2f_2(0)}{\pi\hbar\omega}\frac{1-\varepsilon f_1}{((1-\varepsilon f_1)^2 + \varepsilon^2 f_2^2)^2}, \tag{2.56}$$

where

$$\varepsilon = 415.07\frac{\rho}{A_2(\hbar\omega)^2}. \tag{2.57}$$

The Electronic Handbook of Optical Constants of Solids [46] can calculate the complex refractive indexes based on a simple model for energies above 30 keV, these are quite good and can be implemented into the spectrum in similar manner as the experimental data. The oscillator strength spectrum shown in figure 2.6 for aluminum is generated from combining these three different ways in calculating the oscillator strengths. Equation (2.53) is used as a criteria to check validity of the spectrum, i.e. must be fulfilled as close as possible. Shown below is the database that has been constructed for aluminum from the spectrum in figure 2.6 where n and l are the principal and angular quantum numbers.

Aluminium : $1s^2 2s^2 2p^6 3s^2 3p^1$ 5 shells				
$Z_2 = 13$		$A = 26.98154\,\mathrm{u}$	$I_{tabel} = 166 \pm 2\,\mathrm{eV}$	$\rho_{tabel} = 2.699\,\mathrm{g/cm^3}$
n	l	$f_{(n,l)}$	$I_{(n,l)}$ (eV)	$U_{(n,l)}$ (eV)
1	0	1.623	2701.0	1564.1
2	0	2.147	476.5	121.46
2	1	6.259	150.42	76.753
3	0	2.006	18.20	10.62
3	1	0.965	14.46	5.9858

The oscillator strengths $f_{(n,l)}$ are found by integration of the above spectrum

$$f_{(n,l)} = \int_{\text{shell}} d(\hbar\omega) f(\hbar\omega). \tag{2.58}$$

Determining the contribution to the K- and L-shells is simple because of the absorption edges. When dividing into subshells as in the case of the L-shell the nominal occupation numbers are used as a guideline. Similar approach is used for the valence electron. The mean excitation energy $I_{n,l}$ for each individual shell is found by constructing a spectrum showing $f(E)\ln(E)$ versus E, then integrating over the same regions as for

the oscillator strengths $f_{(n,l)}$. With the definition of I from Bethe theory [21] we can write the mean excitation energy for an individual shell as

$$\ln(I_{(n,l)}) = \frac{\int_{\text{shell}} d(\hbar\omega) f(\hbar\omega) \ln(\hbar\omega)}{\int_{\text{shell}} d(\hbar\omega) f(\hbar\omega)}. \tag{2.59}$$

For the inner electrons, division into principal shells is sufficient. In the case of valence electrons dividing into subshells is important. Binding energies $U_{(n,l)}$ are taken from [50].

2.3 Charge-exchange Theory

Another interesting quantity to study during atomic collisions are the cross sections for capture and loss. In this section we will focus on single charge-exchange cross sections, i.e. capture and ionization. Capturing of an electron can happen through two channels. The first one is direct capture into an electronic state, this is frequently called non-radiative electron capture (NRC, conservation of energy and momentum). The other channel is by capturing an electron and then releasing a photon (radiative electron capture, REC).

2.3.1 Radiative Electron Capture

Radiative electron capture can be described as the radiative recombination of a free electron when the target electrons are weakly bound. Radiative recombination of a free electron is the inverse process of the photoelectric effect. Stobbe [51] has solved this problem long ago within the non-relativistic dipole approximation. The result is for a (n, l) state of a fully ionized ion

$$\sigma_{RR} = \frac{\pi^2}{3}\alpha^2 a_0^2 \left(\frac{\nu_n^3}{1+\nu_n^2}\right)^2 \left[(l+1)(C_{nl}^{l+1}(\nu_n))^2 + l(C_{nl}^{l-1}(\nu_n))^2\right], \tag{2.60}$$

where $\nu_n = \alpha Z_1/(nv/c)$. The $C_{nl}^{l\pm1}$ matrix elements describe the probability for the dipole transition with an angular momentum $l \pm 1$. The REC cross section is derived by convolution with the momentum distribution $\rho(q)$ of the target atom in the center-of-mass system, i.e.

$$\sigma_{REC} = \int d^3q\, \sigma_{RR}(\mathbf{q})\rho(\mathbf{q})\delta(\hbar\omega + E_f - E_i). \tag{2.61}$$

For low Z_2 targets the momentum distribution can be neglected because of the low binding energy in that case $\sigma_{REC} = Z_{qf}\sigma_{RR}$, where Z_{qf} are the number of quasi-free electrons. An electron is considered to be quasi free when its orbital velocity is much smaller than the projectile velocity. Ichihara *et al.* [52] have extended the Stobbe formula to the relativistic regime. For swift ions the number of quasi-free electrons can be set equal to the target atomic number Z_2. REC is the dominant channel for capture in high-energy collisions of high-Z_1 projectiles with low-Z_2 targets.

2.3.2 Non-radiative Electron Capture

Calculation of REC cross sections is fairly simple since the process can be coupled to the photoelectric effect. This is not the case for NRC cross sections. NRC becomes the dominating channel when the nuclear charge of the target becomes sufficiently large. A precise theoretical description of the NRC process is difficult because the Coulomb field of the projectile leads to distortions of the atomic wave functions in the target even at infinite distances.

A classical approach to calculate capture cross sections is the classical trajectory Monte Carlo (CTMC) method. This method was developed by Abrines and Percival [53, 54]. One has a three-body system consisting of the projectile, the electron being transferred and the target particle. From this one sets up Hamilton's equation of motion (12 coupled equation). These are then solved for numerous trajectories where the impact parameter of the projectile, momentum and orientation of the target+electron is randomly selected by the Monte Carlo method. One then averages over all these trajectories and calculates the cross sections. The method applies also to calculate ionization cross sections.

A semi-classical approach to calculate NRC cross sections has been developed by Shevelko [55]. Shevelko uses the relation between the quasi-classical $a(\mathbf{p}, v)$ and quantum-mechanical $f(\mathbf{k}, v)$ exchange amplitudes which is given by

$$a(\mathbf{p}, v) = \frac{1}{4\pi^2 v} \int_P d^2k\, f(\mathbf{k}, v) e^{i\mathbf{k}\cdot\mathbf{p}}, \tag{2.62}$$

where the integral goes over the plane P is given by

$$\mathbf{k}\cdot\mathbf{v} - \omega_{01} - \frac{v^2}{2} = 0, \tag{2.63}$$

where ω_{01} is the difference in the binding energies of the captured electron in the initial (0) and and final state (1) and v is the relative velocity. The quasi-classical amplitude $a(\mathbf{p}, v)$ is given by

$$a(\mathbf{p}, v) = \int_0^\infty dt\, e^{-i\omega_{if}t} \int d^3\mathbf{r} \phi_1^*(\mathbf{r}_2) V(\mathbf{r}_1) \phi_0(\mathbf{r}_1) e^{i\mathbf{v}\cdot\mathbf{r}} \tag{2.64}$$

where $\mathbf{r} = (\mathbf{r}_1 + \mathbf{r}_2)/2$ and quantum-mechanical amplitude $f(\mathbf{k}, v)$ is given by

$$f(\mathbf{k}, v) = \int d^3\mathbf{r} V(\mathbf{r}) \phi_0(\mathbf{r}) e^{-i\mathbf{k}\cdot\mathbf{r}} \int d^3\mathbf{r}' \phi_1^*(\mathbf{r}') e^{i\mathbf{k}\cdot\mathbf{r}'}. \tag{2.65}$$

The capture cross section is given by

$$\sigma_{NRC}(v) = 2\pi \int_0^\infty d^2p\, W(p, v), \tag{2.66}$$

with $W(p, v) = |a(p, v)|^2$ as the exchange probability, this is then normalized to all electron capture channels (using the method of multichannel normalization), i.e.

$$W_n^{(N)}(p, v) = \frac{W_n(p, v)}{1 + \sum_{n'} W_{n'}(p, v)}, \tag{2.67}$$

so equation (2.66) turns into

$$\sigma_{NRC}(v) \;=\; 2\pi \int_0^\infty d^{\,2}p\, W_n^{(N)}(p,v). \tag{2.68}$$

An accurate way to calculate NRC cross sections quantum mechanically is the continuum distorted wave (CDW) approximation developed by Belkić *et al.* [56] where distorted wave functions are applied in the initial and final states. Since such a theory requires large computation time a approximate method might be useful. Meyerhof *et al.* [57] have developed the eikonal approximation (relativistic) which for $1s_{1/2}$-$1s_{1/2}$ transitions (summed over all spin states) can be written in a closed form. In the eikonal approximation the transition amplitude from an initial state to a final state is calculated within the impact-parameter approach. The capture cross section is found by taking the square of the amplitude and integrating over all impact parameters as in equation (2.66). The approximation requires that the collision time is small compared to the transition time between initial and final electronic states. Their formula reads [57]

$$\begin{aligned}
\sigma^{eik}_{1s-1s} &= \frac{2^8\pi Z_1^5 Z_2^5}{5v^2(Z_2^2+p_-^2)^5}\frac{\gamma+1}{2\gamma^2}\frac{\pi\eta Z_2'}{\sinh(\pi\eta Z_2')}e^{-2\eta Z_2'\tan^{-1}(-p_-/Z_2)} \\
&\quad \times(\mathcal{S}_{eik}+\mathcal{S}_{magn}+\mathcal{S}_{orb}), \\
\mathcal{S}_{eik} &= 1+\frac{5}{4}\eta\frac{Z_2'}{Z_2}p_- + \frac{5}{12}\eta^2\frac{(Z_2')^2}{Z_2^2}p_-^2 + \frac{1}{6}\eta^2(Z_2')^2, \\
\mathcal{S}_{magn} &= -\delta^2+\frac{5}{16}\delta^4+\frac{5}{8}\delta^2\frac{\gamma}{\gamma+1}\frac{Z_2'}{Z_2}+\frac{1}{4}\delta^2\eta^2(Z_2')^2+\frac{5}{48}\delta^4\eta^2(Z_2')^2, \\
\mathcal{S}_{orb} &= \frac{5\pi}{18}\delta\alpha(Z_1+Z_2)-\frac{5\pi}{36}\delta^3\alpha(Z_1+Z_2)-\frac{5}{8}\delta\alpha Z_2\eta Z_2'\left(1-\frac{1}{2}\delta^2\right) \\
&- \frac{5\pi}{18}\delta\frac{\gamma}{\gamma+1}\alpha Z_1\frac{Z_2'}{Z_2}+\frac{5\pi}{28}\delta\left(\frac{\gamma}{\gamma+1}\right)^2\alpha Z_1\frac{(Z_2')^2}{Z_2} \\
&- \frac{5\pi}{28}\delta\frac{\gamma}{\gamma+1}\alpha(Z_1+Z_2-\delta^2 Z_1)\frac{Z_2'}{Z_2},
\end{aligned} \tag{2.69}$$

where $\eta = 1/v$, $\delta = [(\gamma-1)/(\gamma+1)]^{1/2}$ and $p_- = \eta(E_f/\gamma - E_i)$ with $E_{i,f}$ as the energies of the initial and final states, setting $Z_2' = 0$ gives the first-order Born approximation and $Z_2' = Z_2$ gives the one electron eikonal approximation. Meyerhof *et al.* [57] have shown that the cross section scales approximately with Z/n where n is the principal quantum number. This allows them to extend the above formula to transitions over different states by replacing Z_1 with Z_1/n and Z_2 with Z_2/n. $\mathcal{S}_{eik}$ is the exact eikonal cross section for relativistic kinematics but with non-relativistic wave functions. $\mathcal{S}_{magn}$ is the magnetic contribution to the capture and $\mathcal{S}_{orb}$ describes the relativistic modification of the electronic orbitals. The NRC cross section scales roughly with (Z_2^5) [57] whereas REC has a much weaker scaling (Z_2).

2.3.3 Ionization Cross Sections

Ionization/excitation cross sections can be calculated within the first-order Born approximation. Let us assume that we have two colliding partners each carrying one

electron, then the scattering-matrix[1] element (in general) can be written simply as

$$S = -i\int_{-\infty}^{\infty} dt \int d^3x \varrho_I(\mathbf{x},t)\varphi_A(\mathbf{x},t), \tag{2.70}$$

$\varrho_I(\mathbf{x},t)$ is the transition charge density created by the projectile and $\varphi_A(\mathbf{x},t)$ is the transition scalar potential generated by the target atom. The indices A and I symbolize the target and projectile respectively. The scalar potential is a solution to the Poisson equation

$$\Box\varphi_A(\mathbf{x},t) = -4\pi\varrho_A(\mathbf{x},t), \tag{2.71}$$

where $\varrho_A(\mathbf{x},t)$ is the transition charge density of the target atom. The charge densities are given by

$$\begin{aligned}\varrho_I(\mathbf{x},t) &= \int d^3R_I d^3r\, \Psi^*_{I,f}(\mathbf{R}_I,\mathbf{r},t)[Z_1\delta(\mathbf{x}-\mathbf{R}_I) \\ &- \delta(\mathbf{x}-\mathbf{r})]\Psi_{I,i}(\mathbf{R}_I,\mathbf{r},t), \qquad (2.72)\\ \varrho_A(\mathbf{x},t) &= \int d^3R_A d^3\rho\, \Psi^*_{A,f}(\mathbf{R}_A,\mathbf{r},t)[Z_1\delta(\mathbf{x}-\mathbf{R}_A) \\ &- \delta(\boldsymbol{\rho}-\mathbf{x})]\Psi_{A,i}(\mathbf{R}_A,\mathbf{r},t). \qquad (2.73)\end{aligned}$$

$\mathbf{R}_I$ and $\mathbf{r}$ are the coordinates of the nucleus and electron (respect to the nucleus) in the projectile vice versa for the target ($\mathbf{R}_A$ and $\boldsymbol{\rho}$). Within the first-order Born approximation the Ψ_i and Ψ_f wave functions are set equal to the unperturbed initial and final states. These states are well known since they can be written as product of a plane wave (motion of the projectile-ion) and a function describing the internal motion of the electron in the projectile. The excitation cross section for transition of the projectile and target electrons can then easily be found

$$\sigma^{0\to m}_{0\to n} = \frac{4}{v^2}\int d^2q_\perp \frac{|F^I_{0n}(\mathbf{q})F^A_{0m}(-\mathbf{q})|^2}{q^4} \tag{2.74}$$

Here $\mathbf{q} = (\mathbf{q}_\perp, q_{min})$ is momentum transfer to the projectile and q_{min} is minimum momentum transfer

$$q_{min} = \frac{\varepsilon_n - \varepsilon_0 + \epsilon_m - \epsilon_0}{v}, \tag{2.75}$$

where ε_{n0} and ϵ_{m0} is the energy difference in the initial and final states of the projectile and target, respectively. The form factors in the above equation are given by

$$F^I_{0n}(\mathbf{q}) = Z_1\delta_{n0} - \int d^3r\, \psi^*_n(\mathbf{r})\exp(i\mathbf{q}\cdot\mathbf{r})\psi_0(\mathbf{r}), \tag{2.76}$$

$$F^A_{0m}(\mathbf{q}) = Z_2\delta_{m0} - \int d^3\rho\, u^*_n(\boldsymbol{\rho})\exp(i\mathbf{q}\cdot\boldsymbol{\rho})u_0(\boldsymbol{\rho}), \tag{2.77}$$

where ψ and u are the states for projectile and target. Equation (2.74) can be split into two parts, one being the screening part and the other is the anti-screening part.

[1]The S-matrix is the transition amplitude for finding a system at $t = +\infty$ in a state Ψ_f if it was known to have been in a state Ψ_i at $t = -\infty$.

The screening part is given by (summing over all final target states)

$$\sigma^{s}_{0\to n} = \frac{4}{v^2}\int d^{\,2}q_{\perp}(Z_2 - \langle u_0|\exp(i\mathbf{q}_0\cdot\boldsymbol{\rho})|u_0\rangle)^2 \times\frac{|\langle\psi_n|\exp(i\mathbf{q}_0\cdot\mathbf{r})|\psi_0\rangle|^2}{q^4}, \tag{2.78}$$

where $\mathbf{q}_0 = (\mathbf{q}_\perp, \varepsilon_{n0}/v)$ and we define the effective charge $Z_{2,eff}(\mathbf{q}_0) = Z_2 - \langle u_0|\exp(i\mathbf{q}_0\cdot\boldsymbol{\rho})|u_0\rangle$. The physical meaning of the above excitation cross section is the following, it is the contribution to the cross section when the target electron remains in its initial state. The effective charge $Z_{2,eff}(\mathbf{q}_0)$ is charge 'seen' by the projectile electron. The second part named the anti-screening part is given by

$$\sigma^{a}_{0\to n} = \frac{4}{v^2}\sum_{m\neq 0}\int d^{\,2}q_{\perp} \times\frac{|\langle u_m|\exp(-i\mathbf{q}\cdot\boldsymbol{\rho})|u_0\rangle\langle\psi_n|\exp(i\mathbf{q}\cdot\mathbf{r})|\psi_0\rangle|^2}{q^4}, \tag{2.79}$$

in this term the target electron also makes a transition. This then increases the cross section where as in screening part the cross section is lowered due to the screening hence the name anti-screening. For collisions with large momentum transfer one can ignore the contribution from the electrons, i.e. $Z_{2,eff} \approx Z_2$ and

$$\sigma^{a}_{0\to n} \simeq \frac{4}{v^2}\int d^{\,2}q_{\perp}\frac{|\langle\psi_n|\exp(i\mathbf{q}\cdot\mathbf{r})|\psi_0\rangle|^2}{q_0^4}, \tag{2.80}$$

then the total cross section is given by

$$\sigma_{0\to n} \approx (Z_2^2+1)\sigma^{pr}_{0\to n}, \tag{2.81}$$

where $\sigma^{pr}_{0\to n}$ is the excitation cross section for a projectile electron interacting with point-like unit charge. When the projectile has several electrons Z_2 then (Z_2^2+1) should be replaced with $(Z_2^2+Z_2)$. The ionization cross section is derived when the transition goes into the continuum (loss of electron). Like for capture cross sections a semi-classical approach can be applied based on the impact parameter p using the time-dependent Schödinger equation and expanding the wave function in a complete set of the initial wave function for the projectile-target system, then we have

$$\sigma^{0\to m}_{0\to n} = \int d^{\,2}p|a^{0\to m}_{0\to n}(\mathbf{p})|^2, \tag{2.82}$$

where $a^{0\to m}_{0\to n}(\mathbf{p})$ are the time-dependent coefficients of the initial wave function.

2.4 Charge-State Distribution (CSD)

When the charge changing cross sections are known one can then determine the charge-state distribution. Let us assume that we have an ion penetrating a material with a

thickness x. The penetrating ion has the initial charge state i. The rate equation [58, 59] describing the change in fraction of the charge states is given by

$$\frac{1}{N_t}\frac{dF_i}{dx}(x) = \sum_{j,j\neq i}\left[F_j(x)\sigma_{ji} - \sigma_{ij}F_i(x)\right], \tag{2.83}$$

F_i denotes the fraction of ions in the charge state i ($\sum_i F_i(x) = 1$), N_t is the density of the target (atoms/cm^3) and x is the penetration depth (cm). So one has to solve a set coupled differential equations in order to determine the thickness dependence of each charge state. The above equation can also be used to determine the cross sections if the thickness dependence of the charge-state distribution is known. In the case of 2 charge states the above equation can be solved analytically. Assume we have an ion carrying one electron penetrating a material (gas or solid) also we assume that the ionization process dominates, this means that the resulting charge-state distribution will consist of H-like (carrying one electron) ions and fully stripped (carrying zero electrons). The rate equation for H-like ions is then given by

$$\frac{1}{N_t}\frac{dF_1}{dx}(x) = F_0(x)\sigma_c - \sigma_l F_1(x), \tag{2.84}$$

F_0 and F_1 are the fractions of naked and H-like ions, σ_c and σ_l are the capture (from $0 \rightarrow 1$) and loss (from $1 \rightarrow 0$) cross sections. The solution with the initial condition $F_1(0) = 1$ is then

$$F_1(x) = e^{-N_t(\sigma_c+\sigma_l)x} + \frac{\sigma_c}{\sigma_c+\sigma_l}\left(1 - e^{-N_t(\sigma_c+\sigma_l)x}\right). \tag{2.85}$$

The above equation shows us that the capture and loss cross sections can be determined from the slope and equilibrium of the curve if the charge state distribution has been measured as function of the thickness. For the initial condition $F_0(0) = 1$ one derives for $F_1(x)$

$$F_1(x) = \frac{\sigma_c}{\sigma_c+\sigma_l}\left(1 - e^{-N_t(\sigma_c+\sigma_l)x}\right). \tag{2.86}$$

In the case of three charge states Allison [59] has derived an analytical solution long ago. When dealing with more charge states than three analytical solutions are available from Sigmund [60].

In the next section we will discuss the density effect in stopping forces, charge-changing cross sections and charge-state distributions.

2.5 Density Dependence in Slowing Down

The gas-solid effect was first experimentally observed in the mean charge of fission fragments penetrating different gases and solids. This work was performed by Lassen [8] in the early 1950s. Bohr and Lindhard made a simple model in 1954 [61] to explain the higher mean charge in the solid. In a solid the collision frequency becomes comparable to the lifetimes of the excited states of the projectile. This then leads to an enhanced

ionization cross section and thereby a higher mean charge. In a gas excited states that are created in the initial collision are de-excited before the next collision. For capture cross sections the situation is the opposite. Because of the high collision frequency in the solids the captured electron will more likely be ionized in the next collision before it can de-excite. This leads to a smaller capture cross section compared to the gas where the captured electron is more likely to reach the ground state before the next collision.

It was long believed that stopping force scales with the charge of the ion to the square, this then suggests that gas-solid difference in the mean charge should be even larger in the stopping force. Initial investigations of the stopping force in various gases and solids did not observe this difference. This then led Betz and Grodzin [62] to propose a different model. They suggest that the mean charge in a gas and solid are closely the same. The high collision frequency in the solid leads to an accumulation of excited states. After the ions exit the matter the excited electrons are released through Auger cascades.

The reason why it took nearly 30 years to observe the gas-solid difference in the stopping force [7] was the presence of Z_2-oscillations at lower velocities. At lower velocities the stopping force is very sensitive to the outer (incomplete) target shells. Screening lowers the effect, this suggest that the Z_2-oscillations are larger for anti-protons than for heavier ions [63]. The effect disappears when the projectile energy becomes sufficiently large. Which was verified with the UNILAC at GSI hence, were available that the gas-solid difference could be observed.

In the following chapter I will explain the experimental setup of the Fragment Separator at GSI Darmstadt, how the experiment was performed and how the data was analyzed.

Chapter 3

Experimental Setup

3.1 The Fragment Separator

The Heavy Ion Synchrotron (SIS) [64] in combination with the linear accelerator UNILAC at GSI provides projectile beams of all elements up to uranium with a maximum magnetic ridgity ($B\rho$) of 18 Tm corresponding to 1.9 GeV/u for ions with a mass-to-charge ratio of two. The accelerator system and the experimental areas are schematically plooted in figure 3.1. The UNILAC injects the ions into the SIS at an energy 11.4 MeV/u after passing two stripper stages. The energy of the beam in the SIS can be determined by Schottky frequency measurements. The projectiles have a momentum spread of a few 10^{-4} and a transverse emittance of about 1π mm mrad when the beam is cooled. The ions can then be extracted over a period of several seconds and directed onto a target. Such a target station exists in front of the Fragment Separator (FRS) [65]. With the FRS one can separate the ions coming from the SIS according to their charge and mass. At the same time the FRS can be used as a high-resolution magnetic spectrometer. Figure 3.2 displays the setup of the FRS. The FRS consists of 4 parts each with a dipole magnet with a sector angle of 30° and a bending radius of 11.25 m. The length of each magnet is about 6 m. Focusing of the ion beam is done with quadrupole magnets, these are placed before and after each dipole magnet (20 in total). Before and after each dipole there is a hexapole (8 in total) for correcting image aberrations. The dispersive focal planes F_1 to F_4 after each dipole stage are equipped with position-sensitive detectors to measure the momentum with magnetic rigidity analysis. At the entrance of the FRS a charge-exchange target was placed in order to select different charge states for the incoming ion beam before it hits the atomic collision target which was placed at F_2. The selection of the incoming charge state is done at F_1 with the slits. After interacting with the target at F_2 the beam is transported to F_3 where the resulting CSD is measured with a position-sensitive multi-wire proportional counter (MWPC).

3.1.1 FRS as a Spectrometer for Atomic-Collision Studies

The bending of an ion in a dispersive magnetic field is determined by its magnetic rigidity ($B\rho$), where ρ is the radius of the trajectory. The ion is deflected perpendicular to the magnetic field B. The magnetic rigidity depends on the momentum p of the ion

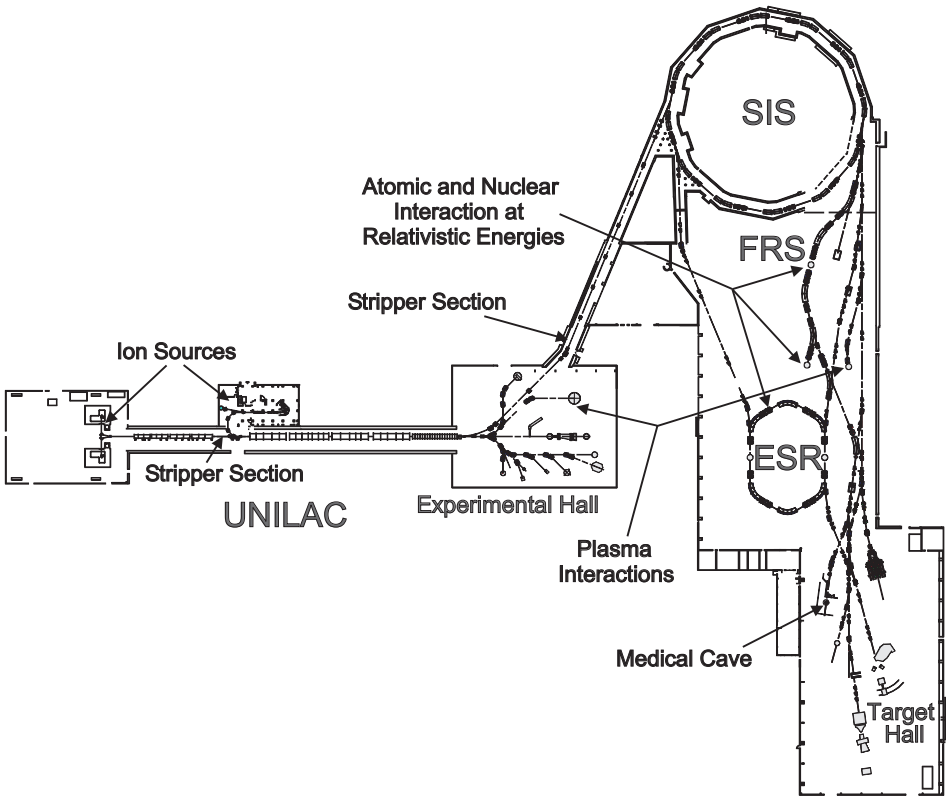

Figure 3.1: Overview of the accelerators and experimental facilities at GSI in Darmstadt.

in the laboratory frame and its charge q, i.e.

$$B\rho = \frac{p}{q} \tag{3.1}$$

$$= \frac{m\gamma v}{q} \tag{3.2}$$

$$= \frac{mc^2}{Qe}\sqrt{\gamma^2 - 1} \tag{3.3}$$

A beam of particles is described, in ion optics, in ion optical coordinates [66] which are defined as deviation from the absolute coordinates of a reference ion moving on the optical axis in the z-direction. Perpendicular to z we have the horizontal (x) and vertical (y) direction and the corresponding angles which are defined as the ratio of the transverse momentum and the momentum of the reference ion ($a = p_x/p_{ref}$, $b = p_y/p_{ref}$). The longitudinal momentum of an ion is given by the relative width of the momentum ($\delta = p/p_{ref} - 1$). These five coordinates are fully sufficient to describe the motion of an ion in the FRS. There are no time-dependent fields in the FRS.

One of the most important characteristics of a spectrometer is the resolution. This tells us how well the spectrometer can separate ions of different momenta without overlap in the spacial distribution. The width of the image is Δx. The resolution is defined as

$$R = \frac{(x, \delta)}{2\Delta x}, \tag{3.4}$$

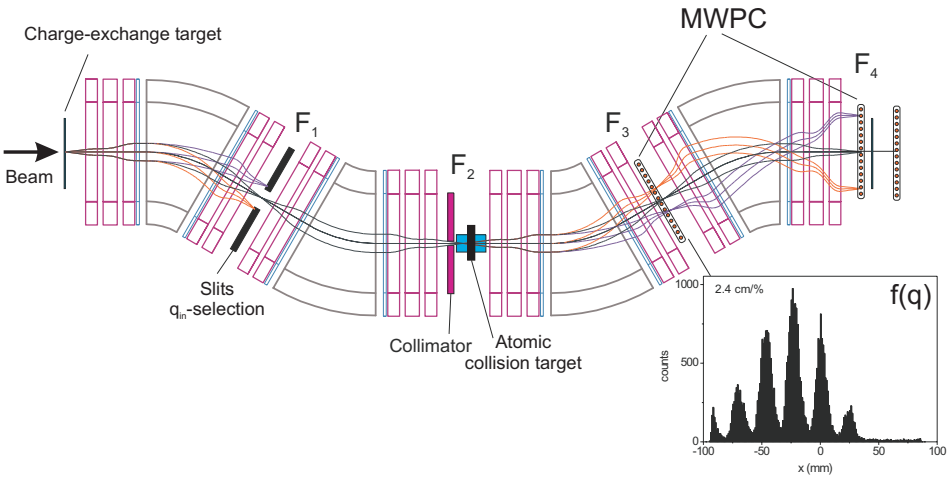

Figure 3.2: Setup of the FRS for the present experiment. The beam, coming from the SIS, interacts first with a charge-exchange target (5.2 mg/cm^2 Al foil) at F_0 to produce the desired charge state which is selected at the focal plane F_1. At the central focal plane F_2 the collision target is placed (solid foil or gas cell). The charge-state distribution $f(q)$ is measured at the third focal plane F_3 with a position sensitive detector (MWPC).

where (x, δ) is the dispersion coefficient. The width of the beam at an arbitrary plane is determined by the initial spacial distribution and the angle (neglecting the dispersion for now). This can very well be described by an ellipse where all positions and angles of the particles are included. The width of the beam is then given in first order by [66]:

$$\Delta x = \sqrt{[(x,x)\Delta x_0]^2 + [(x,a)\Delta a_0]^2}, \tag{3.5}$$

$$\Delta y = \sqrt{[(y,y)\Delta y_0]^2 + [(y,b)\Delta b_0]^2}. \tag{3.6}$$

Along the path of the ions (z), Δx and Δy describe the envelope of all possible beams. Planes where the envelope has its maximum or minimum diameter are named the "waist" of the beam. The plane where the image of the initial position is generated, is characterized in the transfer matrix by $(x, a) = 0$. The width is then $\Delta x = (x, x)\Delta x_0$.

The ion optical setup used for the FRS was calculated with the ion optical code GICO [67]. The ions are centered at F_2 and are separated in space at F_3. The dispersion curve for such a situation is shown in figure 3.3. In that way the broadening of the momentum done by a target at F_2 can be measured, independently from the momentum width from the SIS and from the momentum distribution created by the target at F_0. The momentum acceptance of the FRS is approximately ± 1 % after F_4.

3.1.2 Equipment & Detectors

Figure 3.4 below displays an illustration of the constructed gas cell equipped with 6 μm polypropylene foils in thickness and 5 mm in diameter as windows. These foils were put under several pressure tests in order to determine the maximum pressure they could withstand. The tests concluded that they could handle pressures up to 7 bar.

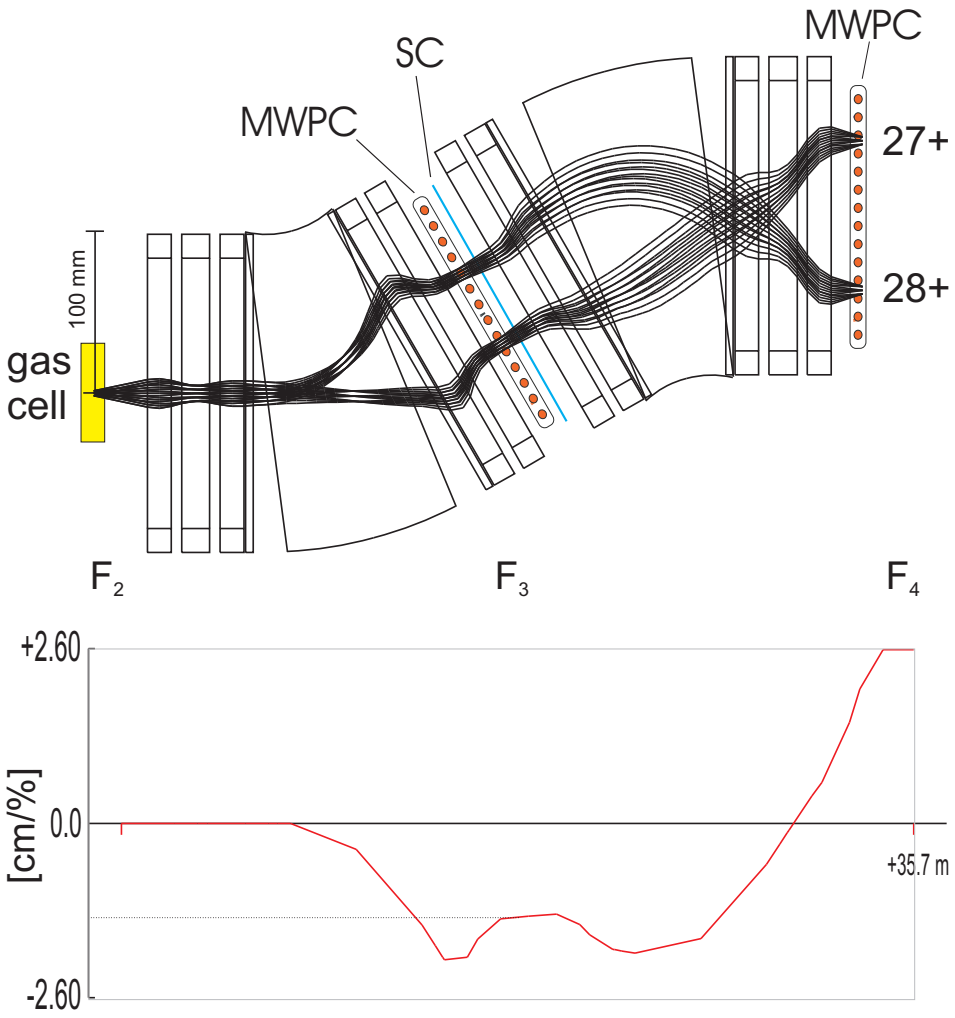

Figure 3.3: Upper part: Trajectories of ions emerging from the focal plane F_2 in different charge states up to F_4. Lower part: Dispersion coefficient (x, δ) from F_2 to F_4.

During the actual measurements the gas cell was never run at pressure higher than 2 bar. Simultaneously the magnitude of the bending of the windows was investigated. These tests showed that the interaction length of the gas cell is increased by 3.2×10^{-4} when the gas cell is run at its maximum of 2 bar. Hence during the experiment the bending of the windows could be ignored.

The gas cell was controlled by a gas controlling system. From there one could control the flow and pressure of the gas and exchange gases. In front of the gas cell a 1 mm collimator made of stainless steel was placed to insure the beam correctly penetrated the gas cell with a small beam spot. Using the collimator causes background in the recorded spectra coming from edge scattered ions that experience additional energy loss. In figure 3.5 a schematic illustration of the constructed gas handling system is presented. The system was placed outside the target area of the FRS.

The gas handling system, shown in figure 3.5, was based on flow control, which required a gas reservoir at vacuum provided by the pump. Two differential pumps

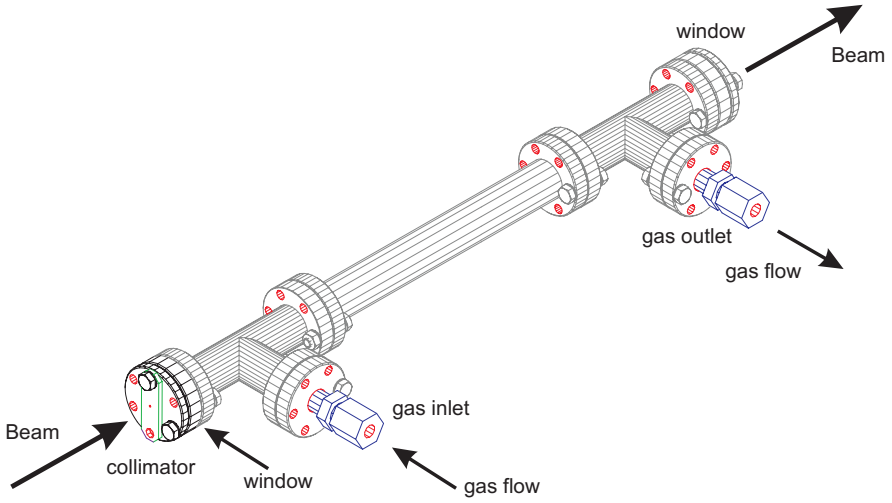

Figure 3.4: Schematic drawing of the gas cell with an interaction length of $\ell_{\mathrm{gas-cell}} = 31.2\,\mathrm{cm}$ equipped with windows of 6 μm polypropylene foils in thickness and 5 mm in diameter. A 1 mm stainless steel collimator was placed in front of the entrance window.

were used in the measurements; one for the flammable gases and one for the inert gases. The test line VTL was used to insure save operation of the gas flow. Setting the pressure in the gas cell was done by first setting the pressure of Pcont with the HP3245A to a desired value, e.g. 10 V corresponded roughly to 2 bar. Then the C1in valve is opened and the VTL valve is closed. Once the manometers reach the desired value the measurement can begin. The voltage outputs from the manometers were calibrated. This was done stepwise by varying the voltage of the HP3245A from 0 V to 10 V in steps of 0.1 from 0 V to 1 V and from thereon 0.25 V steps were used.

The solid targets were positioned on the three target ladders that are available at F_2. These ladders, placed in close distance, can hold up to 20 different targets and they are moved in and out by a remotely controlled step motor. With this setup it is possible to stack targets and thereby reach different thicknesses.

The multiwire proportional counter [68] used to measure the charge-state distribution consists of equally spaced anode wires centered between two cathode planes. The wire spacing is 2 mm with an anode-cathode gap of 7 or 8 mm. The signal from one of the cathode planes gives information on the first coordinate (x) of the ionizing event. Using a second detector where the cathode wires are oriented perpendicularly to the first gives information on the second coordinate (y). The chamber is filled with gas consisting of Ar (75 %), isobutane (24.5 %) and freon-13B1 (0.5 %), where the proportions refer to the volume [68]. The maximum count rate of the MWPC is about 10 kHz. Below this value the detector has an efficiency for heavy ions of almost 100 %. During the experiment the maximum number of particles hitting the detector was roughly 8000 events/spill, where 1 spill corresponds to 8 to 10 seconds.

The second detector used at F_3 right behind the MWPC was a plastic scintillator (SC see figure 3.3). A scintillator consists of a scintillating material which is optically coupled to a photomultiplier either directly or via a light guide. As radiation passes

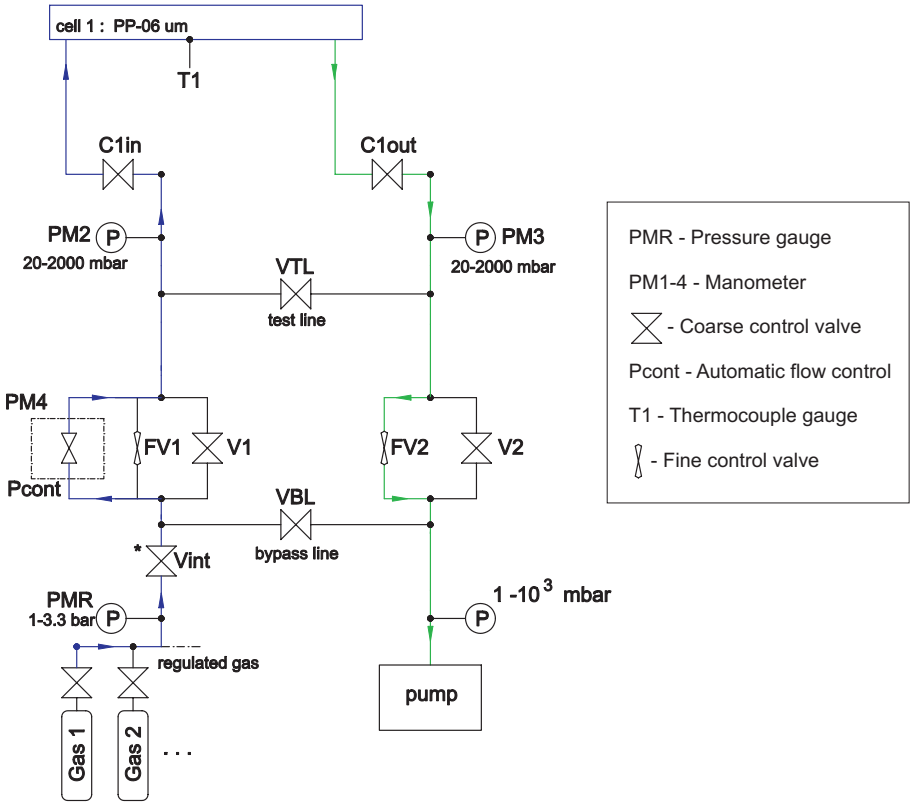

Figure 3.5: Schematic view of the gas handling system at F_2.

through the scintillator, it excites the molecules causing the light emission. The scintillation light in these compounds arises from transitions made by free valence electrons (π-electrons) of the molecule. The light is transmitted to the photomultiplier where it is converted into a weak current of photoelectrons which is then further amplified by an electron-multiplier system. The resulting current signal is then analyzed by a electronics system. These types of detectors have almost 100 % efficiency for heavy ions therefore they can be used to calibrate the efficiency.

3.1.3 Targets

In the nickel run the following solid targets were used C, Al, Ti, polypropylene $(C_3H_6)_n$ and polyethylene $(C_2H_4)_n$. The thicknesses of the targets covered the whole non-equilibrium region of the charge-state distribution and reached well into the equilibrium region. Gaseous targets were N_2, Ne and ethylene (C_2H_4). The purpose of the compound materials was to allow a direct comparison of the charge-exchange cross sections in gases and solids because ethylene, polyethylene and polypropylene have the same carbon-to-hydrogen ratio and to investigate the material dependence of the charge-exchange cross sections. The same thickness range was covered with the gases. The list of the target thicknesses used is given the Appendix A.1.

In the uranium run the target list for solids includes Be and C at 85.0 MeV/u and Be, C, Al, Ti, Cu, Ag, Au and polypropylene for the 61.3 MeV/u measurement. The used thicknesses cover both the non-equilibrium and equilibrium region. At 200.6

MeV/u only Al, Ti and polypropylene were measured. For gases N_2, Ne, Ar, Kr, Xe and ethylene were measured at 61.3 MeV/u and at 200.6 MeV/u Ne, Ar and ethylene were measured. The list of target thicknesses used is given the Appendix C.1.

The thickness of the foils was determined by weighing and measurement of the area. For some of the very thin foils the thickness could only be determined once by a direct thickness measurement with a mechanical sensor which is less accurate.

From the pressures p and temperatures T measured in the gas cell, the density ϱ of the gas was determined by using the Van der Waals gas law.

$$RT = (p + a\varrho^2)(1/\varrho - b), \tag{3.7}$$

where $R = 0.0831\,\mathrm{l \cdot bar/(mol \cdot K)}$ is the gas constant and a and b are the Van der Waals coefficients given in the table below for the measured gases [69].

Van der Waals Coefficients		
Material	a [$\mathrm{l^2 \cdot bar/mol^2}$]	b [l/mol]
N_2	1.3700	0.0387
Ne	0.2080	0.0167
Ar	1.3550	0.0320
Kr	5.1930	0.0106
Xe	4.1920	0.0516
C_2H_4	4.6120	0.0582

Once the gas density has been derived the gas thickness can easily be determined by multiplying the gas density ϱ with the interaction length of the gas cell (31.2 cm)

$$x_{\mathrm{gas}} = \varrho_{\mathrm{gas}} \cdot \ell_{\mathrm{gas-cell}}. \tag{3.8}$$

3.2 Energy Loss Measurement

The energy loss of ^{238}U at the three different energies was determined by the changes in the magnetic rigidity. The incident energies at F_2 were 60.23, 85.00 and 199.99 MeV/u after passing through the charge-exchange target. The different thicknesses of the various materials caused an energy loss of up to 15 % of the incident energy. A list of the measured energy losses can be found in Appendix C.1.

3.2.1 Principle

The energy loss of the individual ions was determined from the settings of the magnetic fields, position of the beam at F_3 and the determined dispersion (see Figure 3.6). Since the energy loss was fairly small, the change was in most cases determined by the change in the beam position at the position detector only. The relation between the position change and the magnetic rigidity is given by

$$\frac{(B\rho) - (B\rho)_0}{(B\rho)_0} = \frac{x - x_0}{(x, \delta)}, \tag{3.9}$$

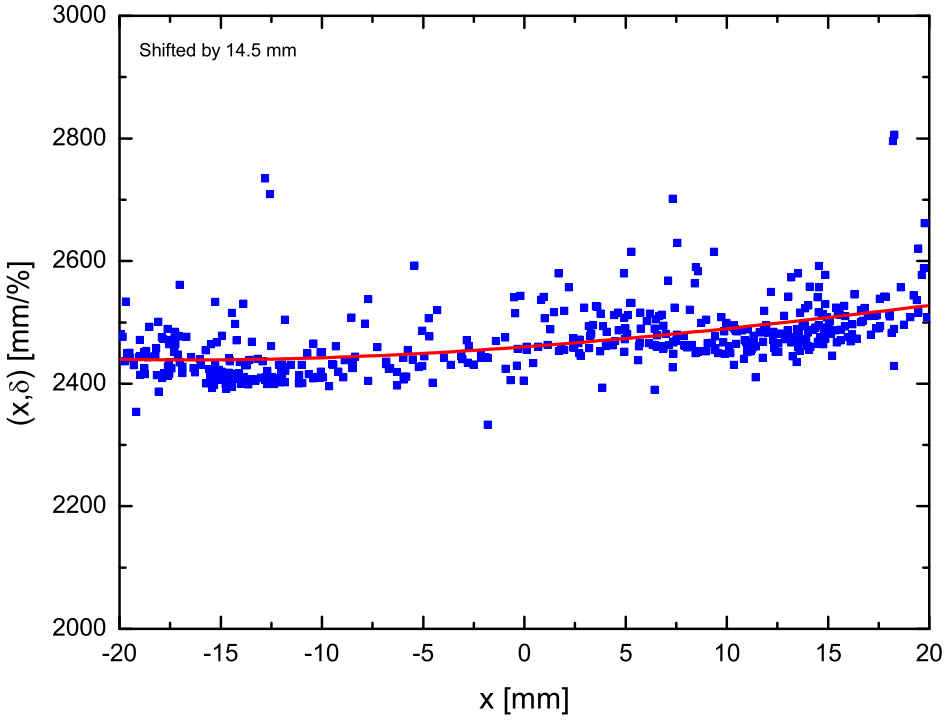

Figure 3.6: Measured dispersion coefficients (x, δ) from peaks of neighboring charge states within ± 20 mm in the center of the MWPC at F_3.

where $(B\rho)_0$ is magnetic rigidity of the beam without a target. Several of these blank measurements were done before and after the change in energy, in order to check if the beam was centered on the detector. The dispersion coefficient (x, δ) was determined from spectra with multiple charge states plus with the assumption that the projectile with different charge states emerged from the same targets has experienced the same energy loss. This assumption has shown to be valid for neighboring peaks within an accuracy of 10^{-3}. In the analysis of the data it was seen that the dispersion could vary up to a few percent depending on the position of the peaks. In order to include this position dependence of the dispersion, all the determined dispersions for all spectra where the peaks are within ± 20 mm were fitted to a polynomial (see figure 3.6). Outside this region the mean value of 2470 mm was used.

3.2.2 Charge-State Distribution (CSD)

The charge-state distribution was measured by position determination with the MWPC detector. In the uranium measurement 10 to 12 charge states could be observed in the distribution. This was too wide for the active detector area which could show only 6 to 7 charge states at once. In order to measure the complete distribution the parts were then combined in the offline analysis. The different parts of distribution were obtained by scaling the B-field. The field was changed to shift the spectrum by 3 charge states each time in order to cover the complete distribution. The principle of this scaling is the following, in order to achieve that the beam has the same position after the change in magnetic rigidity one can describe the deflection angle Φ by the integral of the dipole

fields along the optical axis, i.e.

$$\Phi = \frac{\int_0^L dl\, B(l)}{B\rho}, \tag{3.10}$$

instead of writing the full integral it is common to replace the geometrical length L of the dipole magnet with an effective length L_{eff}, so that the following holds

$$BL_{\text{eff}} = \int_0^L dl\, B(l). \tag{3.11}$$

The B-field is adjusted such that Φ remains constant for a new value of $B\rho$. A small correction is caused due to the fact that the bending radius ρ is proportional to B and the effective length can vary up to a few centimeters. This can lead to a small shift of the beam after scaling of only 0.01 mm because the beam is focused again at the focal plane.

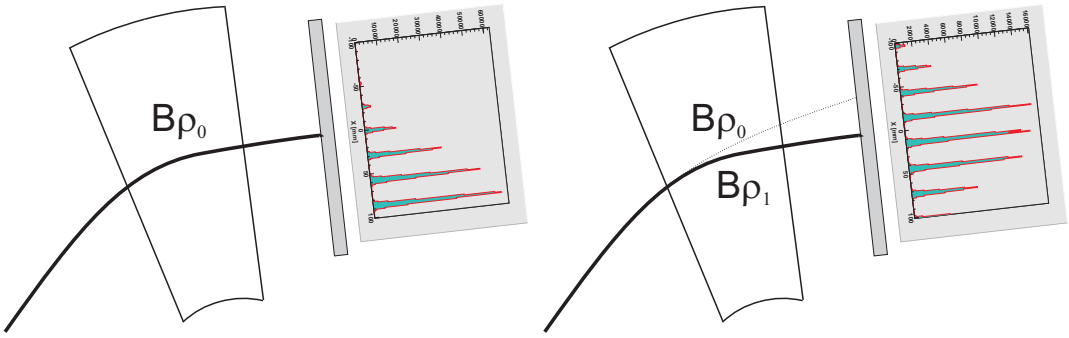

Figure 3.7: Scaling principle for CSD measurement. LEFT : measurement of the charge state distribution with a magnetic rigidity $B\rho_0$. RIGHT : Same measurement but now the magnetic rigidity has been scaled to $B\rho_1$ resulting in a shift of the charge state distribution.

3.2.3 Determination of $B\rho$

The $B\rho$ of the beam in the FRS can be derived in two different ways. The first method determines the B-fields by measurements with calibrated Hall probes (U_H). The other method makes use of the set of measured current-B-field values. All these values were written into log files before and after each single measurement. The relation between the currents, voltages and the $B\rho$ is the following

$$\frac{(B\rho)}{(B\rho)_0} = \frac{(BL_{eff})(I)}{(BL_{eff})(I_0)}, \tag{3.12}$$

or

$$\frac{(B\rho)}{(B\rho)_0} = \frac{U_H}{U_{H,0}}. \tag{3.13}$$

The analysis showed that the difference between the 2 methods of deriving the magnetic rigidity corresponds to an uncertainty for the energy determination of $5 \cdot 10^{-4}$.

3.2.4 Nickel Measurement

The purpose of this experiment was to measure the evolution of charge-state distributions as a function of the target thickness covering both the non-equilibrium and equilibrium region. From this evolution the capture and ionization cross sections can be extracted. An incident 200 MeV/u Ni^{27+} beam was chosen. At this energy the ionization channel dominates both for gases and solids. Hence only the charge states 27^+ and 28^+ of nickel will be populated during the interaction with the target material (26^+ can be neglected because $F_{Ni^{26+}}/F_{Ni^{27+}} \simeq 0.04$ according to charge state calculations with the GLOBAL code [70]). The cross sections can by extracted by fitting equation (2.85) to the experimental data.

There is a 4.5 mg/cm^2 Ti foil placed between the FRS and the SIS in order to separate the two vacua. For a 200 MeV/u Ni^{27+} beam more than 95 % would be ionized to Ni^{28+} after penetration of the Ti foil. In order to have the better experimental conditions for selecting the desired charge state the titanium window was replaced with a thin carbon window with a thickness of 0.035 mg/cm^2.

3.2.5 Uranium Measurement

In this experiment the goal was to measure charge state distributions and energy losses of uranium ions in gases and solids at 3 different energies as a function of the target thickness. The chosen incident energies were 61.3, 85.0 and 200.6 MeV/u. The incident charge state from the SIS was 73^+ for all energies. For the energies 61.3 and 200.6 MeV/u an additional charge-exchange target was used to select higher charge states. For the 61.3 MeV/u measurement 86^+ was the incident charge state at F_2 and in the 200 MeV/u measurement 81^+ was the incident charge state.

3.3 Analysis

3.3.1 Identification of the Charge States

In order to determine the energy loss and charge exchange cross sections for the uranium and nickel projectiles, the charge states in each recorded spectrum need to be identified. Roughly 600 spectra where recorded during the runs. From the FRS status files the B-field were known from these values the $B\rho$ at the center follows. With the help of the ATIMA code [5] which has been implemented into the LISE++ program [71], the energy loss and $B\rho$ was calculated for the applied target. The incoming charge is identified by comparing the calculated $B\rho$ with the experimental value. The calculation with the best agreement identifies the charge state. Once the first charge state is identified in a spectrum the rest follows directly. For nickel measurements the identification was very simple since only 2 charge states were observed as shown in figure 3.8.

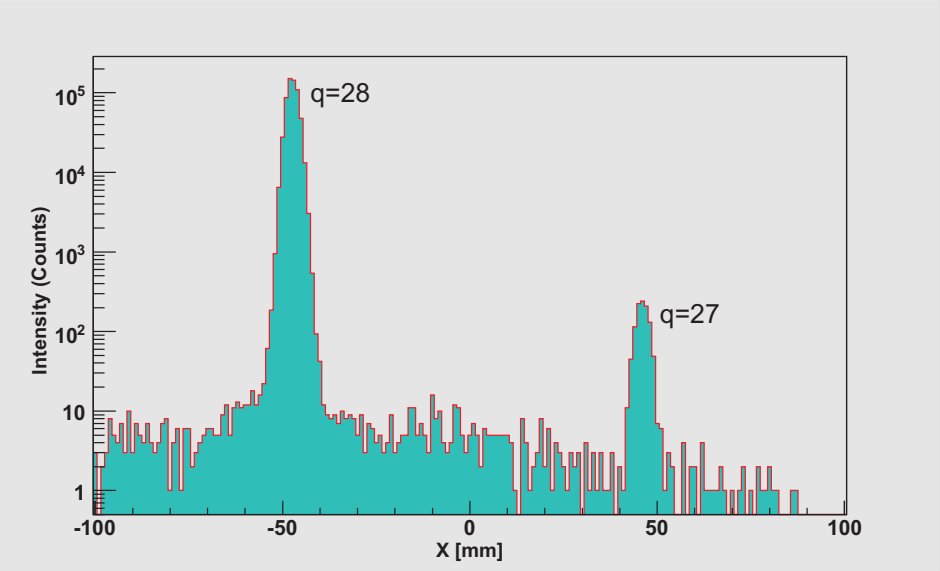

Figure 3.8: Charge-state distribution of an incident Ni^{27+} beam at 200 MeV/u after penetration of a 32 mg/cm^2 carbon foil. Ni^{28+} is the dominating charge state.

3.3.2 Charge-State Distribution (CSD)

Once the charge states in each spectrum have been identified the charge-state distribution can be found. This is done by integration of the peaks. For each peak a gaussian was fitted and then the integral was calculated as shown in figure 3.9. The integral over the gaussian gave the number of ions in the particular charge state. The 1 mm collimator in front of the gas cell produced background due to the particles that were scattered on the edge of the collimator resulting in additional energy loss. The background was subtracted by fitting a polynomial of 4th order to it and then subtracting the area below the peaks from the gaussian peaks. The different parts of the charge-state distributions were combined by normalizing the area of the overlapping peaks.

3.3.3 Energy Loss

Fitting a Gaussian to a peak determines at the same time its mean value. Once the position of a peak is known the corresponding $B\rho$ can be derived from equation (3.9). Then the γ factor can be determined with equation (3.3) and from that the exit energy can be found

$$E_{\text{exit}} = mc^2(\gamma - 1), \tag{3.14}$$

and the energy loss is then

$$\Delta E = E_{\text{entrance}} - E_{\text{exit}}. \tag{3.15}$$

When all the energy losses for one material have been extracted from the data the stopping force can be derived by plotting the energy loss versus the target thickness

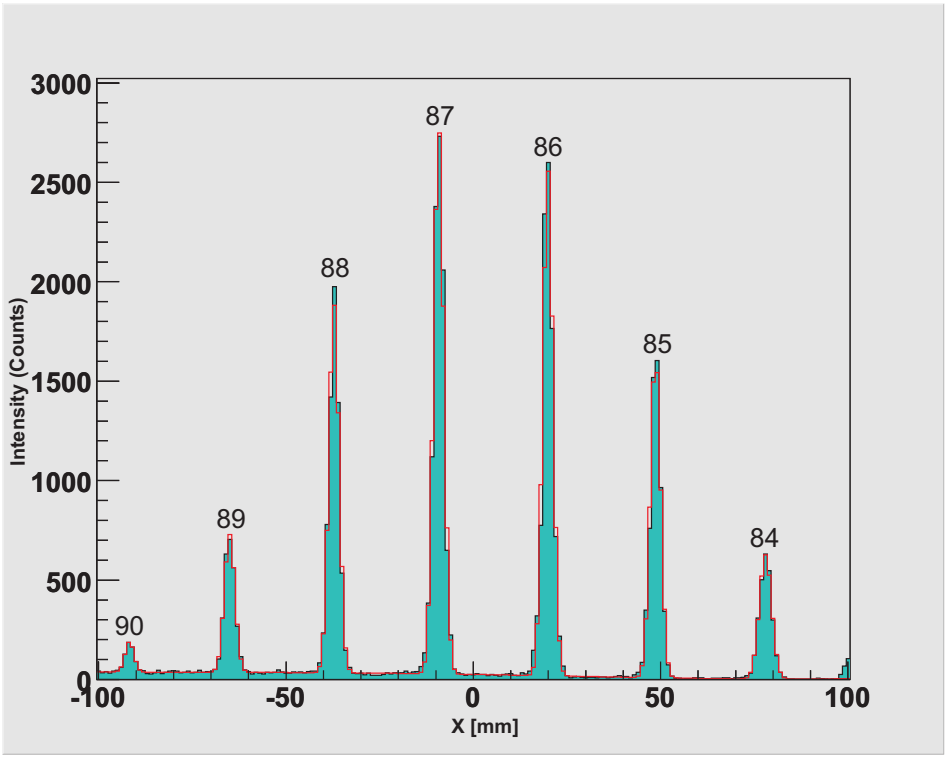

Figure 3.9: Charge-state distribution of an incident U^{86+} beam at 60.23 MeV/u after penetration of 11 mg/cm^2 ethylene (C_2H_4) gas.

of the material. For small energy losses a good assumption for the stopping force is simply

$$\Delta E = \frac{dE}{dx}\Delta x. \tag{3.16}$$

This means that the stopping force can be found from the slope of a linear fit through the energy loss data. In figure 3.10 this is shown for the case of uranium projectiles in aluminum. The data follow very well a straight line.

The stopping force is a function of the projectile energy, but in the assumption above the derived stopping force is independent of the energy (within the range of measured energy losses). This requires some convention to define at what energy the stopping force has been derived. In the analysis the stopping force has been derived at the mean energy given by

$$\langle E \rangle = E_{\text{entrance}} - \Delta E/2. \tag{3.17}$$

In the case of the gas targets the energy loss in the windows must be subtracted

$$\Delta E_{\text{gas}} = \Delta E_{\text{gas-cell}} - \Delta E_{\text{window}}. \tag{3.18}$$

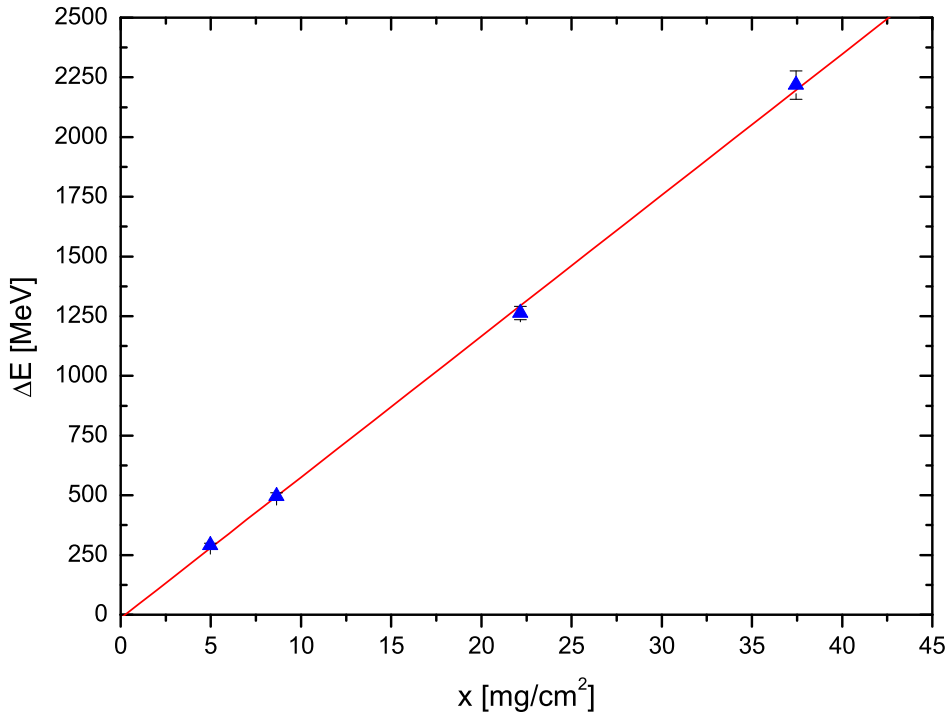

Figure 3.10: Measured energy loss vs. target thickness of an incident U^{86+} beam at 60.23 MeV/u penetrating aluminum foils of various thicknesses. The data are fitted with a straight line.

3.3.4 Experimental Errors for Energy Loss

Several experimental uncertainties characterize these experiments. In this subsection I will give a list of the most important ones. The energy of SIS can be determined with a precision of $\Delta E/E = 1.5 \times 10^{-4}$. The variation in the dispersion has an error of 2.5 %. The most important error in the analysis of the energy loss is the error in the target thickness (see Appendix B). Determining the center of the peaks has an error of 1×10^{-5} in $\Delta E/E$, hence it can safely be ignored.

Since the determined stopping forces in this energy range from energy losses from the non-equilibrium region to the equilibrium, this causes a problem for the comparison with other equilibrium stopping force data. For the gases the presence of the windows increase the mean charge because the polypropylene foils are good strippers. This adds an additional error to the mean charge that has to be estimated. With the GLOBAL code the effect of the windows[1] was calculated. For ethylene gas the mean charge is shifted by 0.1 and for xenon gas the mean charge is shifted by 1.0. Since this is a rough estimate of the effect 50 % of the correction for the mean charge has been added to the statistical error.

[1] Closest material to polypropylene available in GLOBAL is carbon.

Chapter 4

Experimental Results

4.1 Results for Nickel Projectiles

4.1.1 Evolution of Nickel Charge States

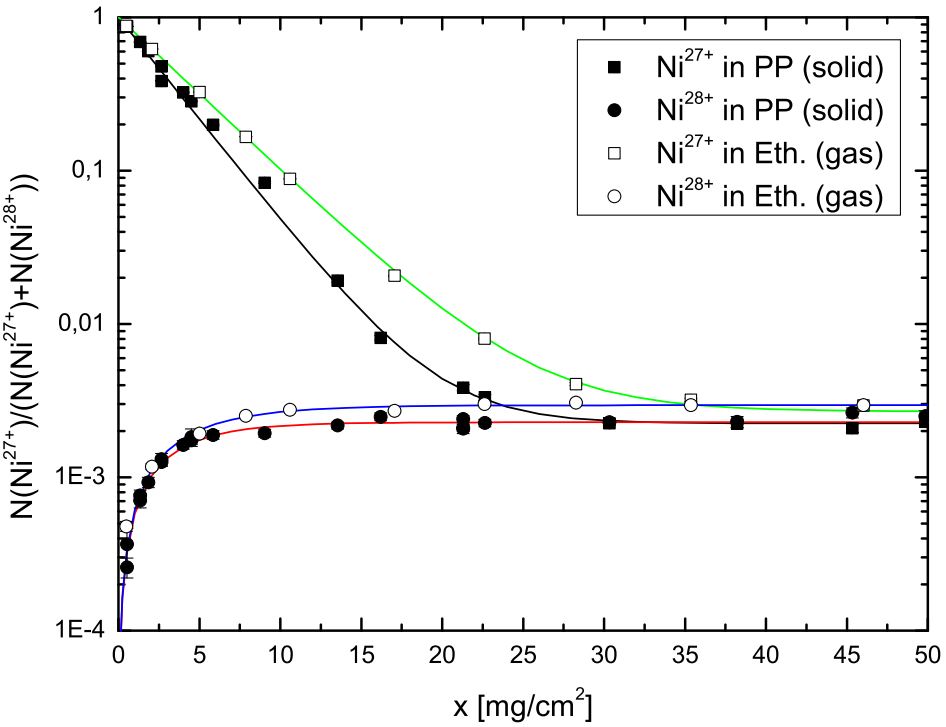

Figure 4.1: Evolution of the fraction of Ni^{27+} ions after interaction with ethylene (C_2H_4, Eth.) and polypropylene ($(C_3H_6)_n$, PP) targets of various thicknesses with a 200 MeV/u Ni^{27+} and a Ni^{28+} incident beam. $N(Ni^{27+})$ and $N(Ni^{28+})$ are the measured numbers of Ni^{27+} and Ni^{28+}, respectively. The lines represent the least square fits to the data, normalized to CH_2. The errors of experimental data are within the symbols.

In figure 4.1 and 4.2 the evolution of Ni^{27+} passing through the compound targets polypropylene (solid), polyethylene (solid) and ethylene (gas) is shown. In the two figures there are two regions characterizing the data of the projectile at incident charge

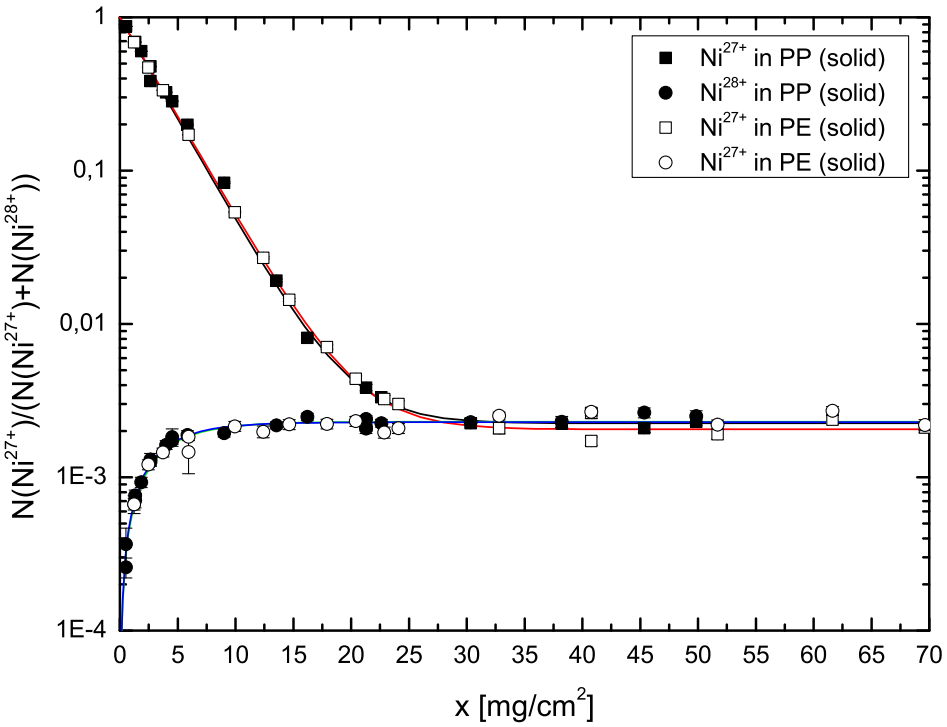

Figure 4.2: Evolution of the fraction of Ni^{27+} ions after interaction with polyethylene ($(C_2H_4)_n$, PE) and polypropylene ($(C_3H_6)_n$, PP) targets of various thicknesses with a 200 MeV/u Ni^{27+} and a Ni^{28+} incident beam. The lines represent the least square fits to the data, normalized to CH_2. The errors of experimental data are within the symbols.

of 27^+ and 28^+. The data showing an exponential decay (full and open squares) were measured for an incident 200 MeV/u Ni^{27+} beam. The data displaying an exponential increase (full and open circles) were measured for a 200 MeV/u Ni^{28+} beam. The measurements with the gas cell yield charge state distributions where the interaction with the window foils is included. The charge state distribution caused by the pure gas can be extracted from these measurements. Sigmund [60] has derived a general matrix formalism for the charge state distribution and the evolution of the charge states. With this formalism the charge state distribution after the gas cell can be written as the product of the matrices for window, gas and window, i.e.

$$\mathbf{F}^{exp}(x_{W,\mathrm{out}} + x_G + x_{W,\mathrm{in}}) \quad = \quad \mathbf{F}^W(x_{W,\mathrm{out}})\mathbf{F}^G(x_G)\mathbf{F}^W(x_{W,\mathrm{in}}), \tag{4.1}$$

where x_G and $x_{W,\mathrm{in}} = x_{W,\mathrm{out}}$ are the thicknesses of the gas and the window foils. The left side of equation (4.1) is a 2x2 matrix (only a 2x2 matrix is needed because only two charge states are observed in the measurement)

$$\mathbf{F}^{exp} \quad = \quad \begin{pmatrix} F_{00}^{exp} & F_{10}^{exp} \\ F_{01}^{exp} & F_{11}^{exp} \end{pmatrix}. \tag{4.2}$$

This describes the charge distribution of the complete gas cell, i.e. the actual measured distributions. In the first column the charge state distribution resulting from a Ni^{28+}

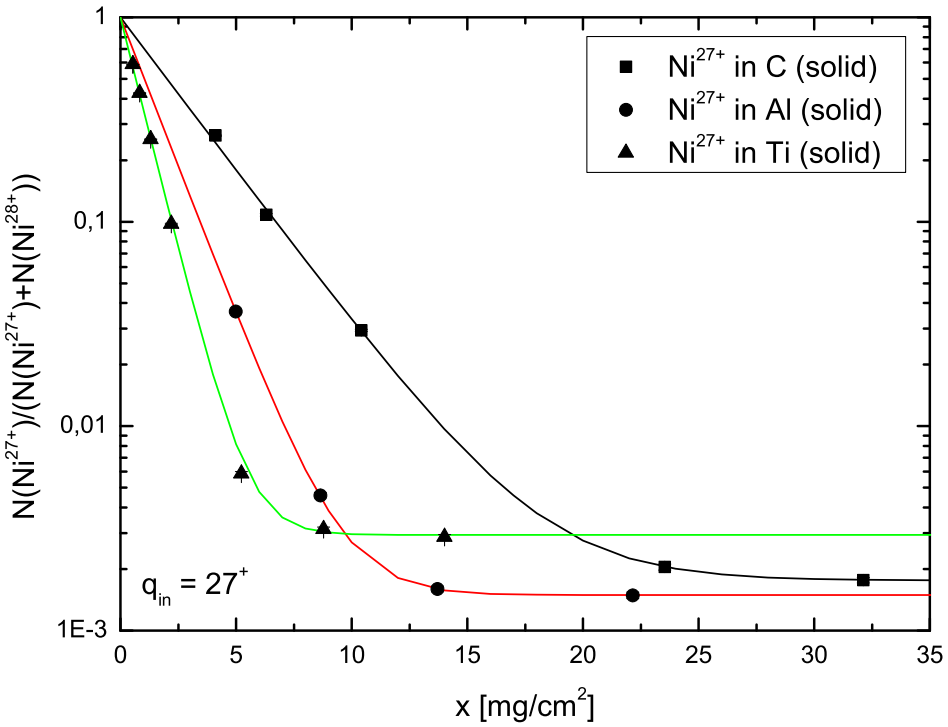

Figure 4.3: Evolution of the fraction of Ni^{27+} ions after interaction with carbon (C), aluminum (Al) and titanium (Ti) targets of various thicknesses. The lines represent the least square fits to the data. The errors of experimental data are within the symbols.

beam is shown and in the second column the charge state distribution resulting from a Ni^{27+} beam is shown. The matrices for the window foils and gas are given in the same manner. Equation (4.1) holds the assumption that the charge-exchange cross sections in the first and second window are equal, i.e. that the energy loss is negligible. At 200 MeV/u this is a good approximation. From equation (4.1) we derive the charge state distribution of the pure gas by inversion of the matrices of the windows, i.e.

$$\mathbf{F}^G = [\mathbf{F}^W]^{-1}\mathbf{F}^{exp}[\mathbf{F}^W]^{-1}. \tag{4.3}$$

The above equation states in order to know the charge state distribution caused by the pure gas the charge state distribution of the gas cell and the window foil need to be measured separately. This has to be done both with a Ni^{27+} and Ni^{28+} beam. This matrix analysis has been performed and the resulting data for the ethylene gas is shown in figure 4.1. The curves shown in the figures 4.1 and 4.2 are the least squares fits to the data. Equation (2.85) was used for the data measured with the Ni^{27+} beam and for the data taken with the Ni^{28+} beam equation (2.86) was used. The fits agree quite well with the experimental data. The separate measurements with Ni^{27+} and Ni^{28+} allow for independent consistency checks of the data, i.e. it is the same equilibrium value reached for both beams with the same target. Figure 4.2 also confirms that the chemical difference between polyethylene and polypropylene does not affect the evolution of the charge state distribution of nickel ions in solids at this energy. In the following figure 4.3 the evolution of the Ni^{27+} fraction in the different solid mono-atomic targets is shown along with the least square fits.

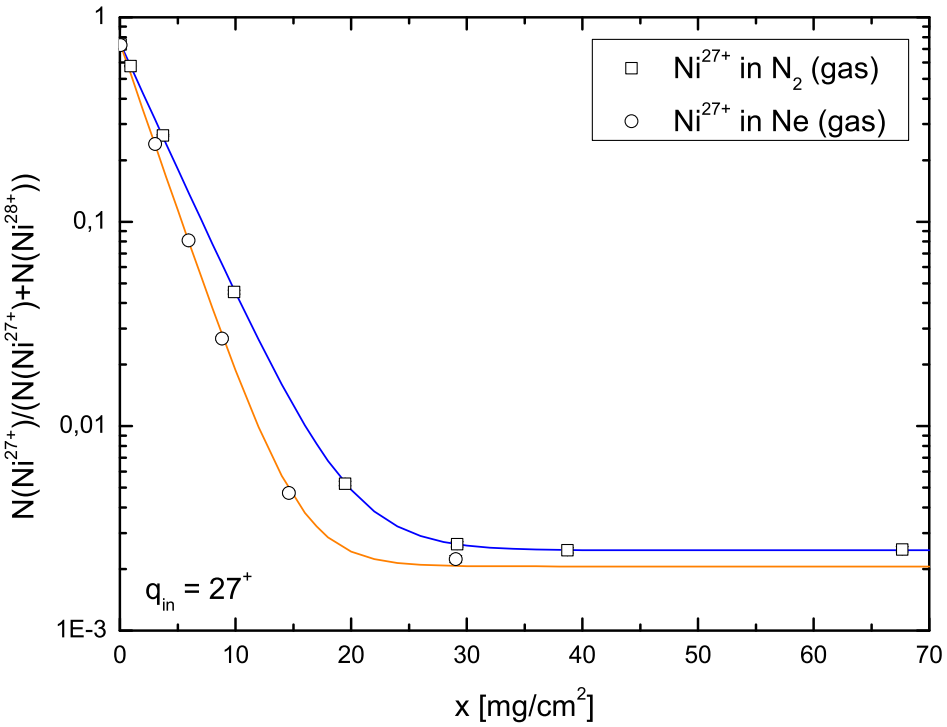

Figure 4.4: Evolution of the fraction of Ni^{27+} ions after interaction with nitrogen (N_2) and neon (Ne) targets of various thicknesses. The lines represent the least square fits to the data. The least square fit to N_2 has been normalized to N. The errors of experimental data are within the symbols.

Figure 4.4 displays the measured evolution of Ni^{27+} in the mono-atomic gases. These are the raw data that have been observed with the gas cell windows included. The charge-exchange cross sections for the pure gases can still be extracted. By using equation (4.1) the matrix element F_{11}^{exp} can be found. Doing the matrix multiplications yields

$$F_{11}^{exp} = F_{10}^{W}(F_{00}^{G}F_{01}^{W} + F_{01}^{G}F_{11}^{W}) + F_{11}^{W}(F_{10}^{G}F_{01}^{W} + F_{11}^{G}F_{11}^{W}). \tag{4.4}$$

The F_{ij} represent the solutions to equation (2.84) for H-like and bare nickel incoming and H-like and bare nickel outgoing. For completeness the solutions are listed below

$$\begin{aligned} F_{00} &= e^{-N_t(\sigma_c+\sigma_l)x} + \frac{\sigma_l}{\sigma_c+\sigma_l}\left(1 - e^{-N_t(\sigma_c+\sigma_l)x}\right) \\ F_{01} &= \frac{\sigma_c}{\sigma_c+\sigma_l}\left(1 - e^{-N_t(\sigma_c+\sigma_l)x}\right) \\ F_{10} &= \frac{\sigma_l}{\sigma_c+\sigma_l}\left(1 - e^{-N_t(\sigma_c+\sigma_l)x}\right) \\ F_{11} &= e^{-N_t(\sigma_c+\sigma_l)x} + \frac{\sigma_c}{\sigma_c+\sigma_l}\left(1 - e^{-N_t(\sigma_c+\sigma_l)x}\right). \end{aligned} \tag{4.5}$$

All the matrix elements for F_{ij}^{W} are already known since the cross sections have been determined from figure 4.1 and 4.2. Then the F_{ij}^{G} matrix elements are the only unknown in the above equation, hence by least square fitting equation (4.4) to the data the

capture and loss cross sections for the pure gas can be extracted. A detailed list of the measured fractions of Ni^{27+} in all target materials can be found in Appendix A.2.

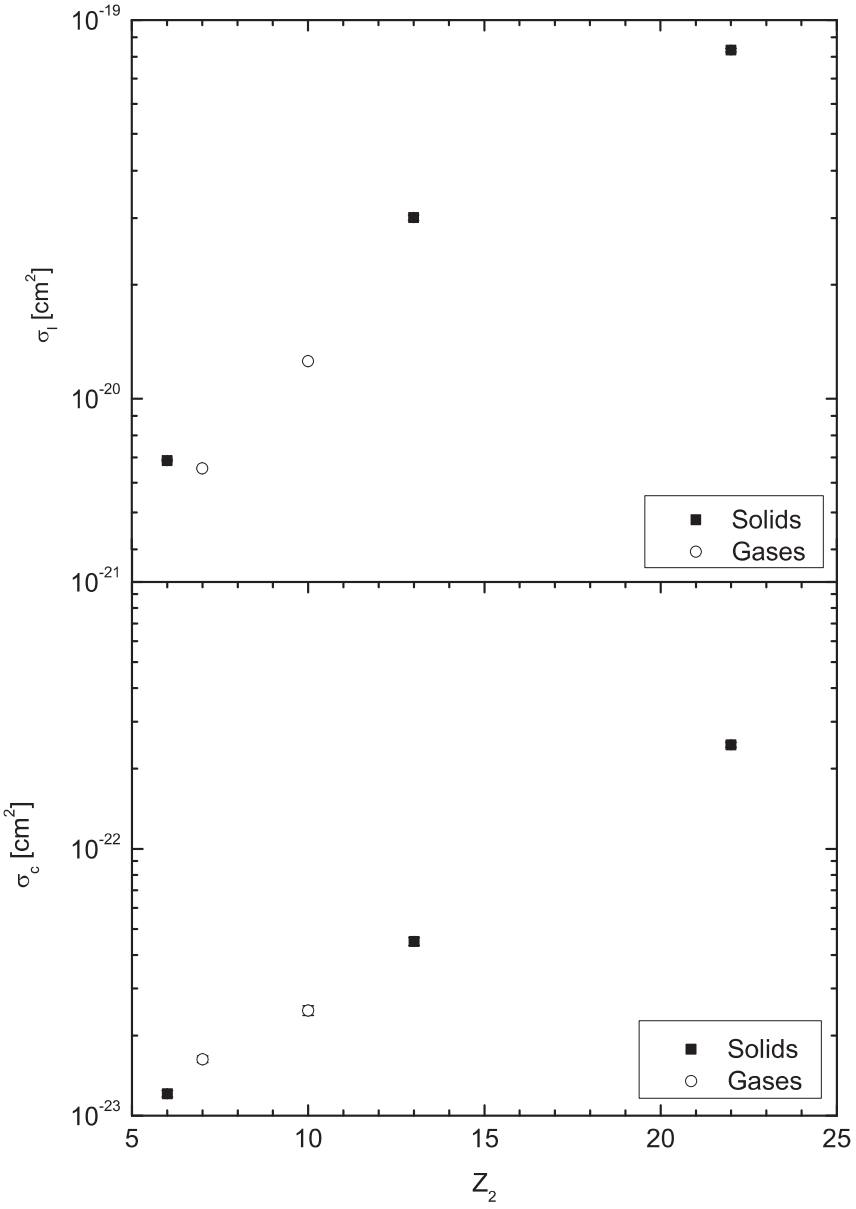

Figure 4.5: Experimental electron loss cross sections σ_l (upper panel) and electron capture cross sections σ_c (lower panel) for Ni^{27+} impinging on different target materials at 200 MeV/u. The experimental error bars are within the symbols.

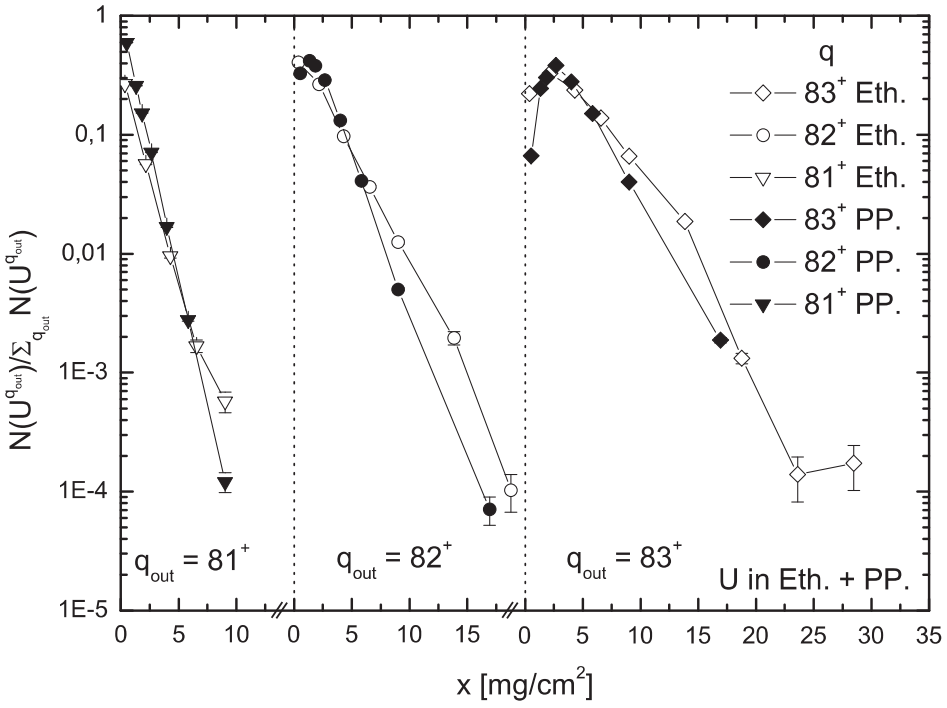

Figure 4.6: The fractions of U^{81+}, U^{82+} and U^{83+} ions for a U^{81+} incident beam at 200 MeV/u passing through ethylene gas and solid polypropylene as a function of target thickness. For better presentation the curves for U^{82+} and U^{83+} are shifted by 10 and 20 mg/cm^2, respectively. The value at the origin for gases are shifted by the influence of the windows of the gas cell.

4.1.2 Charge-Exchange Cross Sections

The capture and ionization cross sections are determined from the least square fits performed to the data. The ionization cross sections are determined from the slope of the fits and the capture cross sections are determined from the equilibrium value at large thicknesses. The extracted cross sections are listed in Appendix A.3 and A.4 for all measured materials. In figure 4.5 the capture and loss cross sections are plotted versus the target atomic number Z_2. The ionization cross sections per CH_2 group (dividing σ_l by 3 for polypropylene and by 2 for ethylene and polyethylene) show a clear gas-solid difference of 30 % which was already indicated by the different slopes of the charge state evolution in figure 4.1. The cross sections per CH_2 (both capture and loss) for polyethylene and polypropylene are identical within the experimental error, confirming that the chemical difference plays small role in the collisions between the nickel ions and the solid compounds. The mono-atomic materials also show a gas-solid difference. The gases (nitrogen and neon) clearly lie below the solids though the Z_2-dependence of the ionization cross sections masks the effect. How to remove this Z_2-dependence from the data will be discussed in the next chapter when the cross sections are compared with theoretical calculations.

The observed gas-solid difference in the ionization cross sections is not found in the capture cross sections shown in the same figure (lower graph). Again one has to take into account that the Z_2-dependence might mask a difference if present.

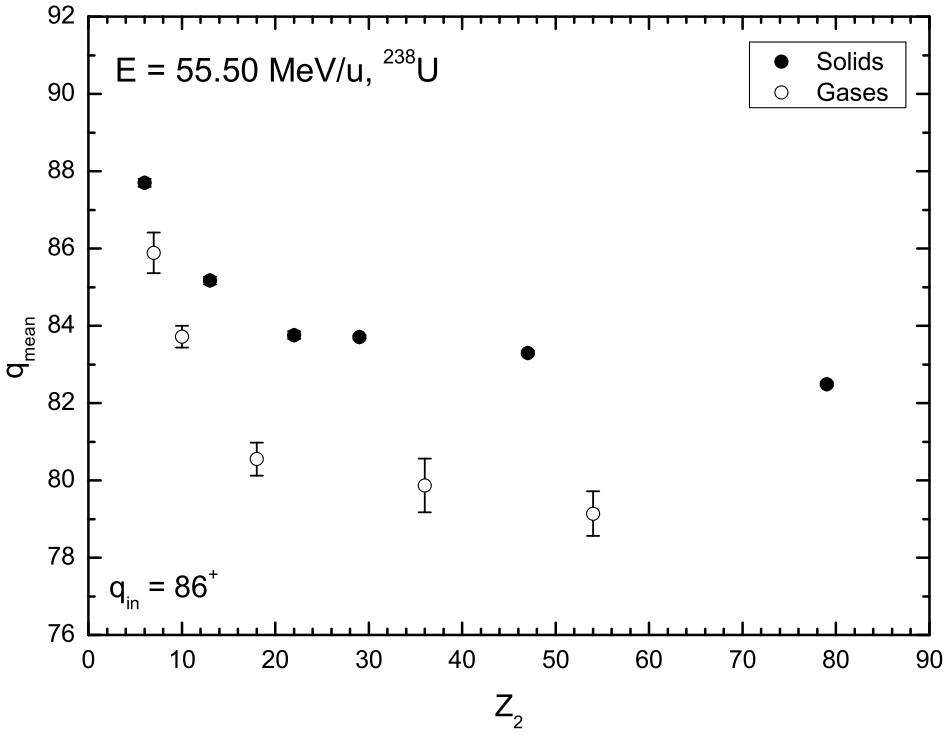

Figure 4.7: Mean charge states of U^{86+} ions passing through gases and solids as function of the target atomic number (Z_2). The mean charge states have been interpolated to the common exit energy 55.5 MeV/u. The large error bars for the gas targets are caused by charge-changing collisions in the windows. Note that not in all materials equilibrium was reached.

4.2 Results for Uranium Projectiles

4.2.1 Uranium CSD in Ethylene and Polypropylene

In figure 4.9 the measured charge-state distribution of U^{81+} at 200 MeV/u penetrating ethylene and polypropylene is shown as a function of the target thickness. The measurements were restricted to charge state below 89 due to background.

In figure 4.6 only the evolution of the charges 81^+, 82^+ and 83^+ is shown. In gases the values are shifted due to the stripping in the windows of the gas cell. Decoupling of the gas cell windows with the matrix formalism wasn't done since it would require measurements of the charge-state distribution with 10 or more incoming charge states of uranium in order to construct the complete matrix for the windows. Therefore the curves for U^{82+} and U^{83+} do not start at 1. The charge 81 corresponds to sodium-like uranium. This is somewhat similar to H-like nickel, since the K- and L-shells are completely filled and are harder to ionize. We observe that the slope of the evolution of the 81^+ charge state is smaller in ethylene compared to polypropylene. This means that the ionization rate is smaller in the gas than in the solid. Hence the 'effective' ionization cross section is smaller in ethylene than in polypropylene and thereby we have a gas-solid effect present as in the case of H-like nickel projectile. Similar conclusions are found for the charge states 82^+ and 83^+ (see figure 4.6). Which partial ionization

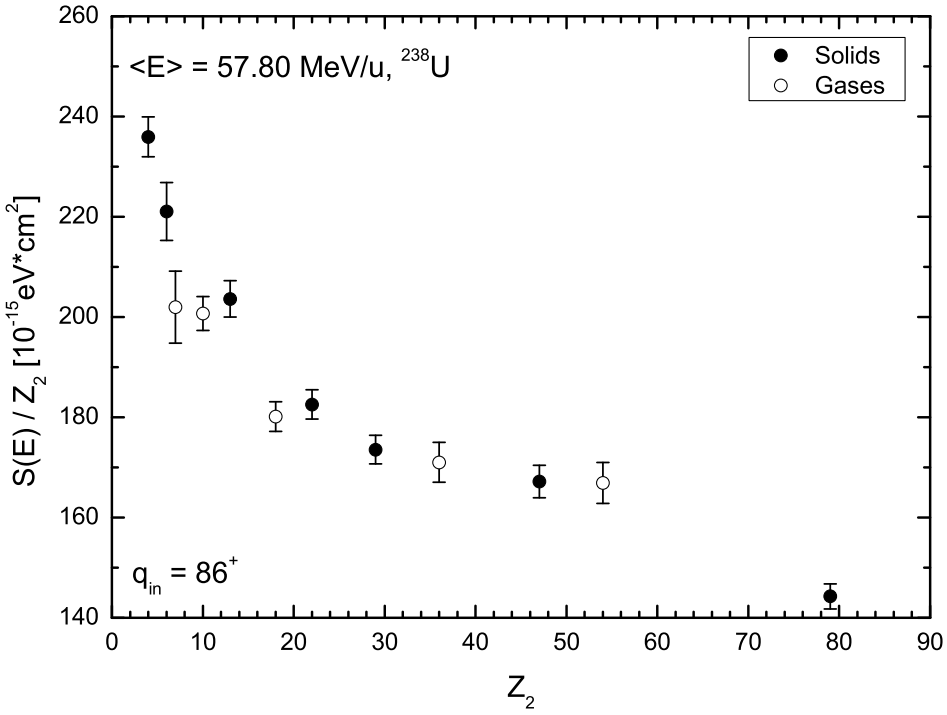

Figure 4.8: Non-equilibrium stopping cross sections per target electron of uranium ions ($q_{in} = 86^+$) in gases and solids. The stopping cross sections have been interpolated to the mean energy $\langle E \rangle = 58.70$ MeV/u in order to compare the results at the same velocity (see Appendix C.2).

cross sections display the gas-solid effect is not possible to determine because of the multitude of charge states present.

4.2.2 Mean Charge and Stopping Force

In figure 4.7 the experimental mean charges are shown for 55.50 MeV/u. The incoming charge state was 86^+. The mean charges have been interpolated to a common energy of 55.50 MeV/u in order to compare the results in different materials. This was done by plotting the mean charge of uranium for each target material as function of the thickness and performing a linear fit to the data. A detailed list of the measured targets and mean charges can be found in Appendix B.1. The effect of the windows have been subtracted in figure 4.6 in the same manner as explained in chapter 3. There is a clear gas-solid effect of roughly 4.7 % for targets with $Z_2 > 13$. Below $Z_2 \leq 13$ the effect is reduced. This could partially be due to a lower total number of charge states involved and still being closer to the initial charge state.

The energy loss obtained from the analysis of the magnetic rigidity of the beam was plotted as a function of target thickness and could be well approximated by a straight line as already discussed in chapter 3. The final charge states varied from one target to another but were always close to the mean charge. This influence due to the uncertainty of the magnetic rigidity measurement and the error of the target thickness determine the error of the stopping cross section for uranium ions. The maximum energy loss

was 15 % of the incident energy. Our experimental results, shown in figure 4.8, are given at an intermediate energy of $\langle E \rangle = 58.70$ MeV/u. Here, we see a gas-solid effect for the lighter materials and no effect for the heavier. This is in contradicts with [9] where the opposite effect was observed, i.e. a gas-solid effect for the heavier targets and no effect for the lighter ones. The initial measurements by Geissel and coworkers [7] display on the other hand a gas-solid effect similar to ours. Currently this difference is not understood. In the next chapter we will give a short argument for how large the gas-solid effect should be according to theory. A detailed list of the experimental stopping forces can be found in Appendix C.2 and C.3.

One has to note that the experimental stopping cross sections are non-equilibrium stopping cross sections. Our targets were so thin that we only covered the non-equilibrium region, only for the very heavy targets the equilibrium region was reached (see Appendix B.1). The incident charge state is the same in all materials and can partially explain the lower difference in energy loss. The absolute values of the stopping cross sections are quite accurate.

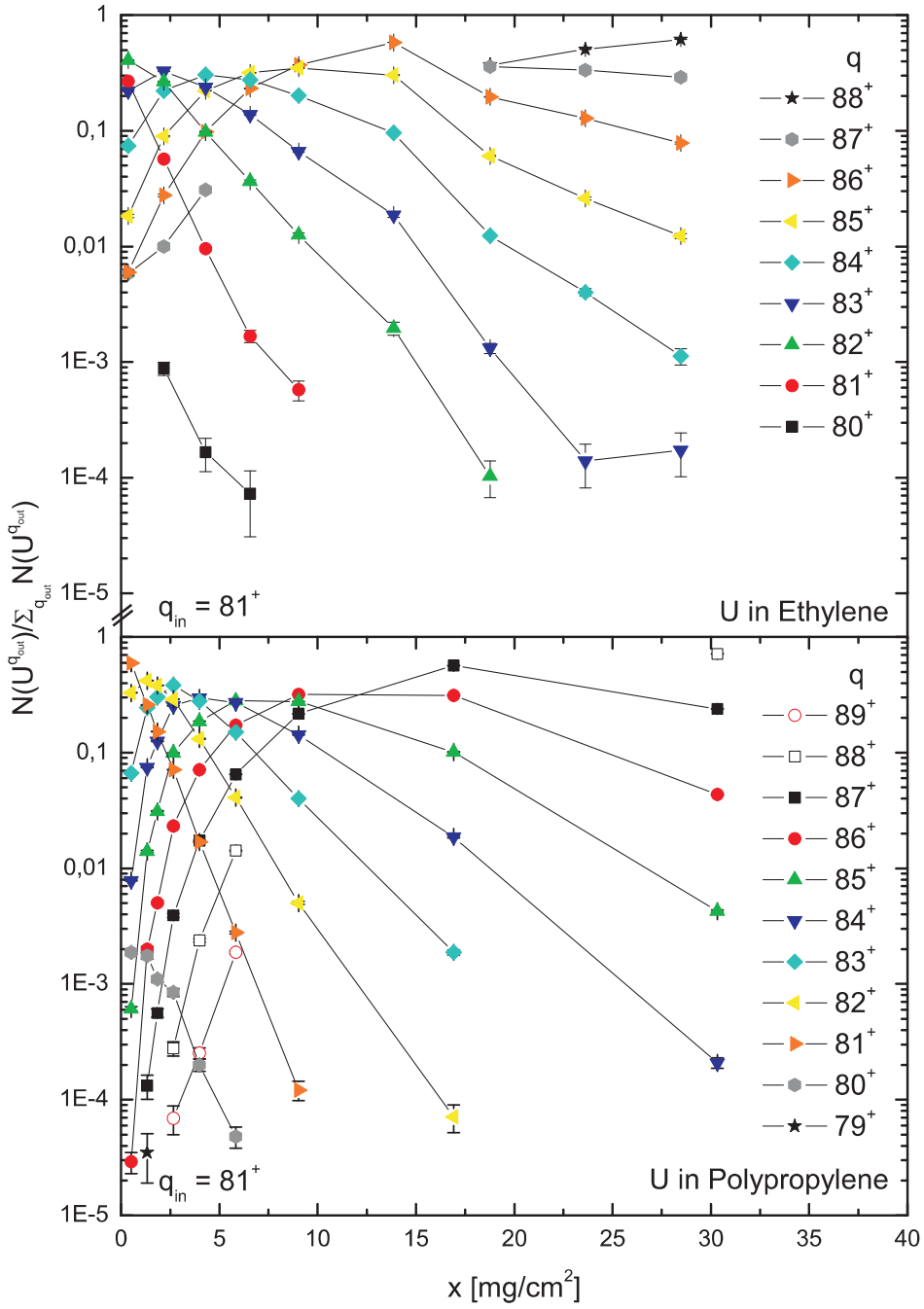

Figure 4.9: Experimental charge-state distribution for 200 MeV/u U^{81+} ions after penetration of ethylene (upper panel) and polypropylene (lower panel) q_{in} is the incident charge state. The data are connected with lines in order to guide the eye.

Chapter 5

Experimental Results Compared With Theory

5.1 Nickel Data

In the previous chapter we presented our experimental capture and ionization cross sections for a 200 MeV/u $Ni^{27+,28+}$ beams penetrating various materials. In order to make theoretical calculations of the capture and loss cross sections we need to determine what excited states contribute to the capture and ionization process, respectively. This requires first of all computation of the lifetimes of the excited states in Ni^{27+}. These have been calculated within the relativistic theory of Dirac for the $2s_{1/2}$, $2p_{1/2,3/2}$, $3s_{1/2}$ and $3p_{1/2,3/2}$ states and are shown in the table below [72]. The third column in table 5.1

Excited State	τ [s]	$\gamma \cdot \tau$ [s]
$2s_{1/2}$	$1.29 \cdot 10^{-9}$	$1.57 \cdot 10^{-9}$
$2p_{1/2}$	$2.58 \cdot 10^{-15}$	$3.14 \cdot 10^{-15}$
$2p_{3/2}$	$2.62 \cdot 10^{-15}$	$3.18 \cdot 10^{-15}$
$3s_{1/2}$	$2.37 \cdot 10^{-13}$	$2.88 \cdot 10^{-13}$
$3p_{1/2}$	$8.59 \cdot 10^{-15}$	$1.04 \cdot 10^{-14}$
$3p_{3/2}$	$8.62 \cdot 10^{-15}$	$1.05 \cdot 10^{-14}$

Table 5.1: Lifetimes of excited states τ in Ni^{27+} [72], γ is the relativistic Lorentz factor.

shows the relativistic corrected lifetime at 200 MeV/u. The lifetimes must be compared with the collision time for charge-changing. From this comparison we can determine what states most likely will contribute to the capture and loss cross section. From the experimental cross sections we can easily get the mean free path length [13]

$$\lambda_i(E) = \frac{1}{N_t \sum_j \sigma_{ij}(E)}, \tag{5.1}$$

where E is the projectile energy and N_t is the target density. The collision time can be found by dividing the projectile velocity with the free mean path length. The travel time for a 200 MeV/u Ni^{27+} ion through a 32 mg/cm^2 carbon foil is roughly $8 \cdot 10^{-13}$ s. A list of the mean free paths lengths λ_i in the different target materials can be

found in Appendix A.4 for capture, loss and excitation. Comparison yields that for the solids both the $2s$ and $3s$ contribute but in the gases only the $2s$ state supersedes the collision time. Anholt [75] has formulated a theory for single electron capture and loss involving four states. Following Anholt, we consider four different low-lying states of nickel projectiles. The states we consider have either no electron (with a relative probability F_0), or just one electron in the $1s$ state (F_{1s}), $2s$ state (F_{2s}), or in the $2p$ states (F_{2p}). The electron can be captured into $1s$, $2s$ or $2p$ and later again be ionized from these states. For H-like ions the $1s$ electron can undergo a monopole excitation to the $2s$ state or a dipole excitation to the $2p$ state, while the 2s electron can be excited into the $2p$ state. In addition to the excitations one-electron states may also decay to some lower level either by radiative decay or collision de-excitation. All these processes must be taken into account in order to determine the capture and loss cross sections. Within this model, the population dynamics of the 1s, 2s and 2p states is described by the system of rate equations [75]

$$\begin{aligned}
\frac{1}{N_t}\frac{dF_0}{dx}(x) &= -(\sigma_{1s}^{cap}+\sigma_{2s}^{cap}+\sigma_{2s}^{cap})F_0(x)+\sigma_{1s}^{ion}F_{1s}(x)+\sigma_{2s}^{ion}F_{2s}(x) \\
&\quad +\sigma_{2p}^{ion}F_{2p}(x) \\
\frac{1}{N_t}\frac{dF_{1s}}{dx}(x) &= \sigma_{1s}^{cap}F_0(x)-(\sigma_{1s}^{ion}+\sigma_{1s\to 2s}^{exc}+\sigma_{1s\to 2p}^{exc})F_{1s}(x)+\sigma_{2s\to 1s}^{dec}F_{2s}(x) \\
&\quad +\sigma_{2p\to 1s}^{dec}F_{2p}(x) \\
\frac{1}{N_t}\frac{dF_{2s}}{dx}(x) &= \sigma_{2s}^{cap}F_0(x)+\sigma_{1s\to 2s}^{exc}F_{1s}(x)-(\sigma_{2s}^{ion}+\sigma_{2s\to 2p}^{exc}+\sigma_{2s\to 1s}^{dec})F_{2s}(x) \\
&\quad +\sigma_{2p\to 2s}^{dec}F_{2p}(x) \\
\frac{1}{N_t}\frac{dF_{2p}}{dx}(x) &= \sigma_{2p}^{cap}F_0(x)+\sigma_{1s\to 2p}^{exc}F_{1s}(x)+\sigma_{2s\to 2p}^{exc}F_{2s}(x) \\
&\quad -(\sigma_{2p}^{ion}+\sigma_{2p\to 1s}^{dec}+\sigma_{2p\to 2s}^{dec})F_{2p}(x),
\end{aligned} \tag{5.2}$$

where x denotes the thickness of the target, N_t the target atom density, and where $F_0(x)+F_{1s}(x)+F_{2s}(x)+F_{2p}(x)=1$. The $\sigma_{i\to j}^{dec}$ and $\sigma_{i\to j}^{exc}$ are the decay and excitation cross sections, respectively. As mentioned above, the excited one-electron states may decay both, by the radiative decay as well as due to a collisional de-excitation. The (electron) decay cross sections are therefore given in terms of the radiative transition rates $\Gamma_{i\to j}$ and the excitation cross sections $\sigma_{j\to i}^{exc}$ [75]

$$\begin{aligned}
\sigma_{2s\to 1s}^{dec} &= \frac{\Gamma_{2s\to 1s}}{N\beta c\gamma}+\sigma_{1s\to 2s}^{exc} \\
\sigma_{2p\to 1s}^{dec} &= \frac{\Gamma_{2p\to 1s}}{N\beta c\gamma}+\frac{1}{3}\sigma_{1s\to 2p}^{exc} \\
\sigma_{2p\to 2s}^{dec} &= \frac{\Gamma_{2p\to 2s}}{N\beta c\gamma}+\frac{1}{3}\sigma_{2s\to 2p}^{exc}.
\end{aligned} \tag{5.3}$$

With our experimental setup we could only distinguish between bare ions (with probability $G_0=F_0$) and ions with just one electron ($G_1=F_{1s}+F_{2s}+F_{2p}$) after passing through the target. The rate equation for such a system can be found from

the above equations and one finds

$$\begin{aligned}\frac{1}{N_t}\frac{dG_0}{dx}(x) &= -\sigma_c G_0(x) + \sigma_l G_1(x) \\ \frac{1}{N_t}\frac{dG_1}{dx}(x) &= \sigma_c G_0(x) - \sigma_l G_1(x),\end{aligned} \tag{5.4}$$

where σ_c and σ_l are the 'effective' capture and loss cross sections. These are given by [13]

$$\sigma_c = \sigma_{1s}^{cap} + \sigma_{2s}^{cap} + \sigma_{2s}^{cap}, \tag{5.5}$$

and

$$\sigma_l = \frac{\sigma_{1s}^{ion} F_{1s}(x) + \sigma_{2s}^{ion} F_{2s}(x) + \sigma_{2p}^{ion} F_{2p}(x)}{F_{1s}(x) + F_{2s}(x) + F_{2p}(x)}. \tag{5.6}$$

As can be seen from the above equations. The capture cross section is just the sum of the capture cross sections into the three states. The ionization cross section on the other hand depends on the relative population of the excited states $F_{1s}(x)$, $F_{2s}(x)$ and $F_{2p}(x)$, respectively and more importantly the target thickness. The relative populations are obtained by integrating the system (5.2). As discussed by Anholt [75], such an integration can be performed analytically if the $2s \rightarrow 2p$ excitation cross section ($\sigma_{2s\rightarrow 2p}^{exc}$) is assumed to be very large compared to all other cross sections and hence, the relative population of the $2s$ and $2p$ levels equilibrates according to the level multiplicity $F_{2p}/F_{2s} = 3$. Then the four-state model reduces to a three-state model which can be solved exactly [59]. Using the equilibrium ratio Anholt derives an analytical expression for the ionization cross section

$$\begin{aligned}\sigma_l = \sigma_c \Bigg[& \frac{\frac{3}{4}\sigma_{2p\rightarrow 1s}^{dec}\sigma_c + \tilde{\sigma}_2^{ion}\sigma_{1s}^{cap}}{\frac{3}{4}\sigma_{2p\rightarrow 1s}^{dec}\sigma_{1s}^{ion} + (\sigma_{1s}^{ion} + \sigma_{1s\rightarrow 2s}^{exc} + \sigma_{1s\rightarrow 2p}^{exc})\tilde{\sigma}_2^{ion}} \times \\ & \left(1 + \frac{\sigma_{1s\rightarrow 2s}^{exc} + \sigma_{1s\rightarrow 2p}^{exc}}{\frac{3}{4}\sigma_{2p\rightarrow 1s}^{dec} + \tilde{\sigma}_2^{ion}}\right) + \frac{\sigma_{2s}^{cap} + \sigma_{2p}^{cap}}{\frac{3}{4}\sigma_{2p\rightarrow 1s}^{dec} + \tilde{\sigma}_2^{ion}}\Bigg]^{-1},\end{aligned} \tag{5.7}$$

where the notation $\tilde{\sigma}_2^{ion} = (\sigma_{2s}^{ion} + 3\sigma_{2p}^{ion})/4$ for the effective ionization cross section from the $n = 2$ levels has been introduced.

5.1.1 Numerical Calculations

In this section we discuss the numerical calculations that have been performed in order to evaluate equation (5.7). The numbers for the individual cross sections (decay, excitation etc.) are given in appendix D. The numerical work for the excitation, ionization and REC cross sections have been provided by Surzhykov and Fritzsche [1]. NRC cross sections were kindly provided by Shevelko [2].

The ionization cross sections have been calculated within the framework of the plane-wave Born approximation including the proper screening corrections as discussed by Voitkiv in [76]. Similar to the ionization, the excitation cross sections have been calculated within the framework of the relativistic plane-wave Born approximation

inducting the screening corrections. The decay cross sections are evaluated as given in equation (5.3). The radiative decay rates $\Gamma_{i\to f}$ have been calculated within the Dirac's relativistic theory; they take the values

$$\begin{aligned} \Gamma_{2s\to 1s} &= \Gamma^{M1}_{2s\to 1s} + \Gamma^{E1E1}_{2s\to 1s} = 4.73 \times 10^9\, s^{-1} \\ \Gamma_{2p\to 1s} &= \Gamma^{E1}_{2p\to 1s} = 3.82 \times 10^{14}\, s^{-1} \\ \Gamma_{2p\to 2s} &= \Gamma^{E1}_{2p\to 2s} = 2.80 \times 10^9\, s^{-1}. \end{aligned} \tag{5.8}$$

In general, the radiative $2s \to 1s$ and $2p \to 1s$ decay rates are negligible when compared with the collisional de-excitation cross sections in (5.3). For the $2p$ levels, in contrast, the $2p \to 1s$ radiative decay and the de-excitation cross section $\sigma^{exc}_{1s\to 2p}/3$ are of the same size.

Two basic electron capture processes may occur in ion-atom collisions: (i) the non-radiative electron capture (NRC), where the energy and momentum transfer in the collision is shared between the projectile, target and the captured electron and (ii) the radiative electron capture (REC), where the electron transfer is accompanied by the simultaneous emission of a photon, carrying away the excess energy and momentum. Therefore, both, NRC and REC charge transfer processes have to be taken into account to calculate the electron capture cross sections

$$\sigma^{cap}_i = \sigma^{REC}_i + \sigma^{NREC}_i. \tag{5.9}$$

The computation of the radiative recombination cross sections σ^{REC}_i within the framework of Dirac's relativistic theory has been discussed previously [73]. It requires the evaluation of the free-bound transition matrix elements for the electron-photon interaction. These matrix elements and all the recombination cross sections are calculated by using the DIRAC program [74] which has been developed by the theory group in Kassel for studying the properties and dynamical behavior of hydrogen-like ions. As seen from appendix D, the theoretical REC capture cross section scales with the nuclear charge of the target as

$$\sigma^{REC}_i(Z_2) \;=\; Z_2 \cdot \sigma^{REC}_i(Z_2 = 1) \tag{5.10}$$

and agrees with the discussion in chapter 2. The NRC scales with Z_2^5, and becomes rapidly important as the target atomic number Z_2 is increased. The NRC cross sections have been calculated with the CAPTURE code [55] with added density effect as described in [77].

5.1.2 Discussion

In figure 5.1 the experimental capture cross sections are compared with theoretical calculations. For the carbon and nitrogen targets the REC process is the dominant channel. For the heavier targets the NRC becomes the dominant channel. We have very good agreement between theory and experiment in the case of carbon and nitrogen. As mentioned in chapter 2 the REC process is directly coupled to the time-inverse photoelectric effect, hence can be calculated very precisely. At higher Z_2 we observe large disagreements between theory and experiment which is likely caused by the theoretical NRC contribution which is, as previously mentioned, difficult to calculate,

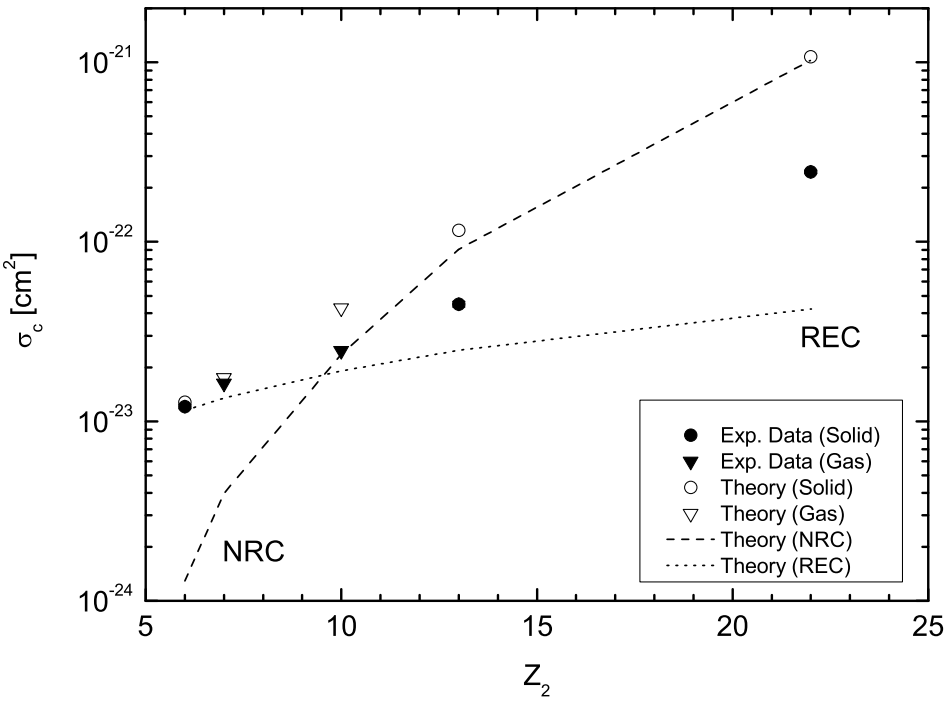

Figure 5.1: Experimental capture cross sections σ_c for Ni^{27+} impinging on different target materials at 200 MeV/u compared with theoretical calculations. The open symbols represent the theoretical calculations [73, 77]. The dashed and dotted lines represent the contributions from the NRC [77] and REC [73] processes, respectively.

nonetheless the disagreement motivates for further refinement and improvement of the theory. The results and calculations do not exhibit a gas-solid difference this is due to the large mean free path length of Ni^{28+} for the probability of electron capture (see Appendix A.3 and A.4). Hence, a gas-solid difference cannot be present for Ni ions at these projectile energies. This conclusion is supported by previous investigations [77] as mentioned earlier.

In chapter 2 it was mentioned that the ionization cross section scales with $(Z_2^2 + Z_2)$ within the first-order Born approximation. We have in figure 5.2 divided the ionization cross sections for the monoatomic materials with this factor and it is observed that the reduced cross sections are divided into two groups. The reduced ionization cross sections are now independent of Z_2. The solids lie approximately 40 % above the gases which demonstrates the presence of a gas-solid effect in ionization. The theoretical calculations also predicts a gas-solid difference. Very good agreement is achieved for the gases (within 3 %). This good agreement illustrates the fact that for the gas targets more than 99 % of the hydrogen-like Ni ions are occurring, due to the large mean free path length, in the ground 1s state [1]. The situation is quite different for the solid targets (Z_2 = 6, 10 and 22) which have much higher atom densities compared to the gas targets. The higher atom densities result in a 6-11 % population of the excited ion states and, hence, cause an increase of the ionization cross sections. The deviation between theory and experiment in the case of carbon is currently not understood. The theory does predict a gas-solid difference as we have observed in the experiment. This

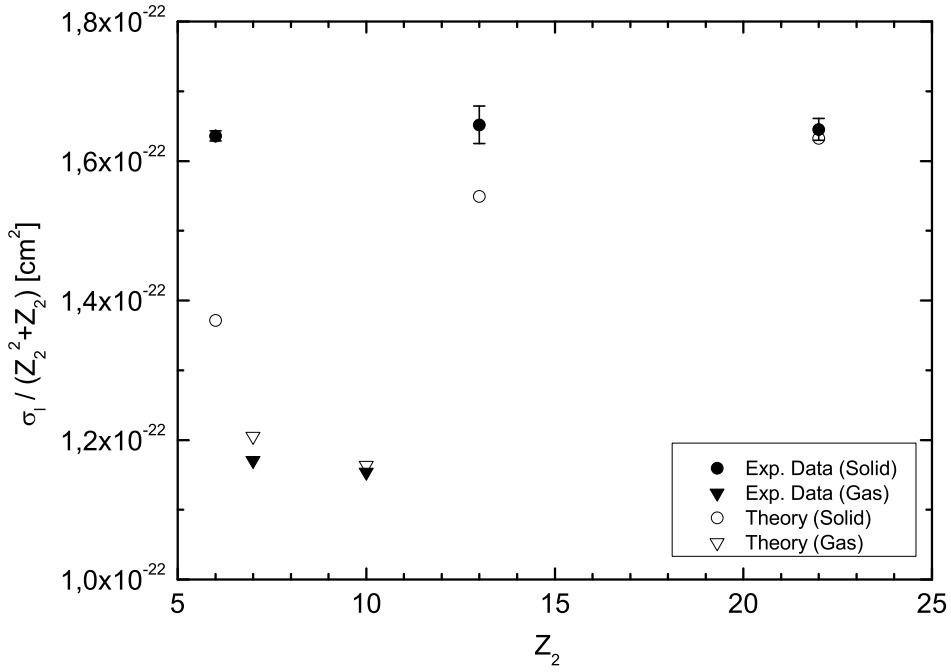

Figure 5.2: Normalized ionization cross sections σ_l for Ni^{27+} impinging on different target materials at 200 MeV/u. The data are compared with theoretical calculations.

is our main conclusion.

The presence of a gas-solid difference in the ionization cross sections both in the monoatomic matarials and the compounds is a proof of the Bohr-Lindhard model [61]. The large density of the solids compared to the gases increases the number of excited electrons in the projectile and the shorter path length in the solids between two subsequent collisions prevent de-excitation of the electrons. Hence, the ionization cross section when passing through the solid is enhanced. The experimental conditions exclude any Auger de-excitation after penetration of the solids thereby the Betz-Grodzin model [62] cannot be applied to this situation.

So far the discussion has avoided comparing our experimental cross sections for the compound materials with theory. This has been intentional since calculation in molecular targets is much more complicated than for elements mainly due to the increased complexity of the target wave function. Currently only a few codes can calculate relativistic wave functions but these codes are developed for chemical problems and therefore cannot be applied to our situation. A simple approximation could be used by assuming that the superposition principle is valid, i.e. the cross section for ethylene for example is the sum of 2 carbons and 4 hydrogens. At this point it is to risky to use this assumption since theory and experiment for carbon do not agree. Therefore, the experimental cross sections for ethylene, polyethylene and ethylene are presented without comparison with theory. The conclusion we can draw from our measurements is that there is a gas-solid difference in ionization of roughly 30 % between ethylene and the solid polymers. The chemical difference between the polymers plays no significant role in ionization or in capture.

5.2 Uranium Data

GLOBAL [70] takes into account up to 28 charge states. The capture and ionization cross sections are calculated as described in chapter 2. Solving the rate equation for the charge-state distribution is done by the Runge-Kutta method. The ETACHA code [78] can also calculate charge-statr distributions of ions up to 28 electrons distributed over the $n = 1$, 2, and 3 principal shells. Determination of the cross sections is done in a similar manner as in GLOBAL. The main difference between the two codes is that ETACHA takes the excitation into higher states into account (even for $n \geq 3$) and the decay rates of these states are also included. This feature is important to model the gas-solid effect.

5.2.1 Mean Charge

In figure 5.3 our experimental mean charges are compared with calculated mean equilibrium charge calculations. The GLOBAL code agrees quite well with our experimental data for the solids. For the gases the mean charge is strongly overestimated especially for xenon which seems like an artifact of the code. The mean charges from the ETACHA code do not agree with the experimental results this behavior has been reported before for other projectile and target combinations [79]. For both gases and solids it widely overestimates the mean charge (caused by including excitations to higher levels). But the calculation does predict a gas-solid difference for the heavier targets though the magnitude of the effect is somewhat smaller. Both codes approach a constant mean charge in the solids like the experiment. Also both codes show higher mean charge for the lighter targets. Part of the disagreement between GLOBAL and experiment is most likely caused by the fact that GLOBAL is adjusted for energies above 100 MeV/u [70] although the code is still applicable down to 30 MeV/u but the results will be less accurate. The ETACHA code has been reported to be well applicable at energies around 10 MeV/u and for light projectiles [79] such as neon ions for example. The main conclusion at this point is that these codes need further refinement.

5.2.2 Stopping Force

Figure 5.4 shows our measured stopping cross sections compared with the predictions of the PASS code [4], ATIMA [5] code and the tables of Hubert *et al.* [6]. The calculations have been done in the frozen charge state mode with $q_1 = q_{mean}$, where q_{mean} are the experimental mean charges scaled up to the energy 57.80 MeV/u in the same manner as explained in the previous chapter. In the case of beryllium the mean value could not be extracted in the experiment, the standard Thomas-Fermi mean charge has been used instead in the calculation. Our experimental stopping cross sections do only exhibit a gas-solid difference for the light materials, carbon and nitrogen. This is completely opposite to what was observed in figure 5.3. Why the experimental data have a complete opposite behavior is currently not understood. From the observed difference in the mean charge a significant difference in energy loss is expected. At 60.23 MeV/u we are in the Bohr region, $\kappa \sim 3.91$ [31], the impact parameter for the closest approach $b = 2Z_1e^2/mv^2 \simeq 0.046$Å is larger than the L-shell

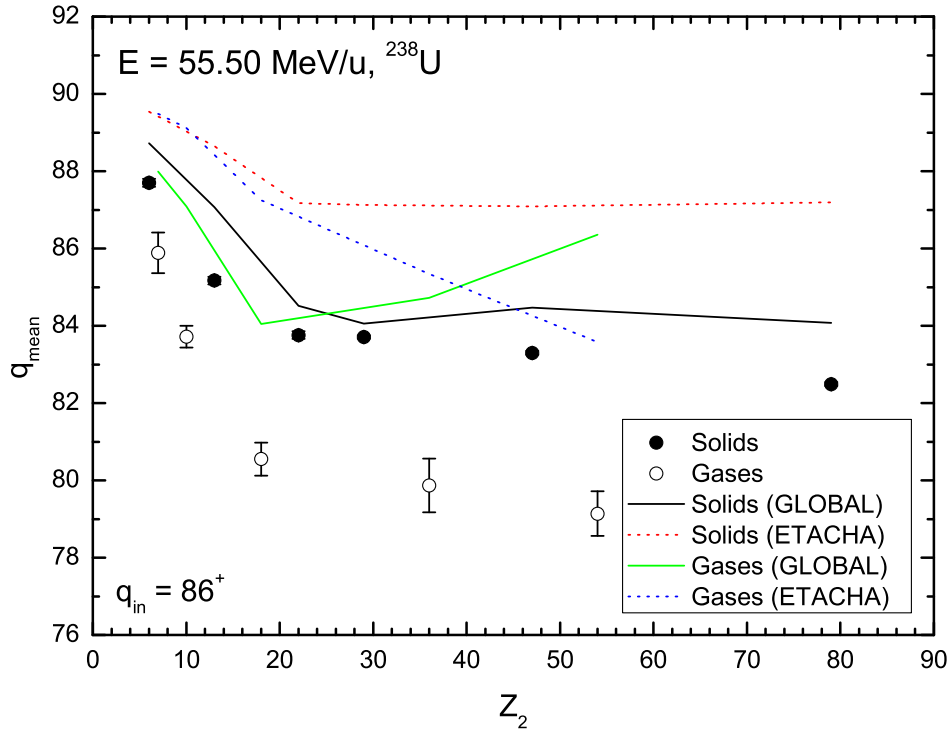

Figure 5.3: Experimental mean charges compared for 55.5 MeV/u ^{238}U ions with predictions from ETACHA [78] and GLOBAL [70] codes. The incident charge (q_{in}) was 86^{+}.

radius $a_L = a_0 n^2/Z_1 \simeq 0.023$Å of the projectile (uranium has its L-shell partially filled in all target materials). A rough estimate of the screening radius can be derived from [32]. Setting q_1/Z_1 to 0.9 one obtains a screening radius $a_{sc} \simeq 0.012$Å. From this one may conclude that the projectile behaves like a point charge, i.e. the stopping cross section is proportional to q_1^2. Therefore, one would expect a gas-solid effect from 9 to 10 % in the stopping cross section.

The following holds for equilibrium stopping cross sections

$$S_{mean} = \sum_J P_J S(q_J) \neq S(q_{mean}), \tag{5.11}$$

but in the region were our measurements took place this difference has previously [80] been found to be insignificant in the binary theory in the case of uranium ions penetrating carbon. The theoretical predictions from PASS (using $S_{mean} = S(q_{mean})$) lie systematically below the experimental ones this is due to omitting the contribution from electron capture to the stopping force. This was motivated due to artifacts which can be ascribed to the model underlying the current implementation of the PASS code. The beryllium calculation is very low compared to the experimental result which is mostly likely caused by the Thomas-Fermi mean charge used. The ATIMA [5] calculations also lie systematically (projectile excitation not included) below the experimental results. In the ATIMA calculation the mean-charge formula from Pierce and Blann [81] is used

$$q_{mean} = Z_1 \left(1 - e^{-0.95\, v/Z_1^{2/3} v_0}\right). \tag{5.12}$$

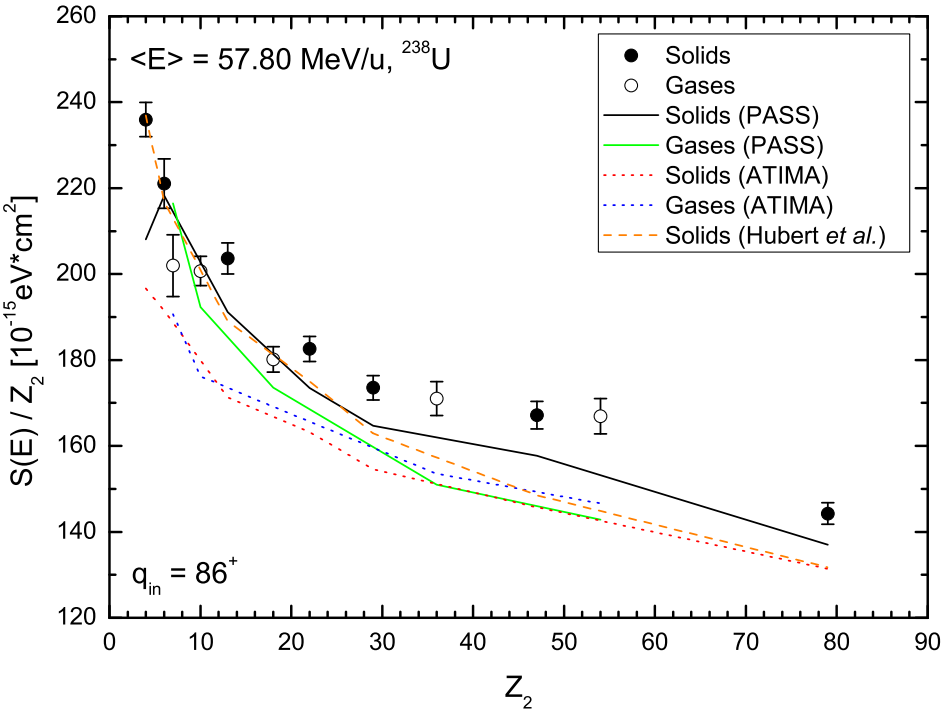

Figure 5.4: Experimental stopping cross sections compared with theoretical predictions from ATIMA and the PASS code. Note that the experimental $S(E)$ values are not equilibrium values (see Appendix C.2).

Like the Thomas-Fermi mean-charge formula (2.46) it holds no information about the density of the target and has no Z_2-dependence, hence it cannot predict a gas-solid difference. The Hubert *et al.* tables agree well with data for the light targets while for the heavier targets they are too low compared to the experimental data.

The PASS code does predict a gas-solid difference for the heavier targets (above copper) much like our experimental mean charge data do. But the difference is smaller than for the mean charge, hence demonstrating that the stopping force is not proportional q_1^2 and that argument given above is not completely valid. This has been shown for different heavy projectiles recently [80] over a wide energy region.

Appendix A

Nickel Data

A.1 Target List

Material	x [mg/cm^2]	Material	x [mg/cm^2]
C	4.10±0.04	Ti	0.54±0.01
C	6.31±0.02	Ti	0.83±0.02
C	10.41±0.06	Ti	1.31±0.03
C	13.18±0.30	Ti	2.20±0.05
C	23.54±0.37	Ti	5.23±0.17
C	32.13±0.36	Ti	6.06±0.19
N_2	0.06±0.00	Ti	7.43±0.22
N_2	0.92±0.00	Ti	8.78±0.14
N_2	3.72±0.01	Ti	14.01±0.31
N_2	9.87±0.02	Ti	25.86±0.44
N_2	19.49±0.04	$(C_2H_4)_n$	1.24±0.03
N_2	29.17±0.06	$(C_2H_4)_n$	2.47±0.05
N_2	38.72±0.08	$(C_2H_4)_n$	3.71±0.08
N_2	67.65±0.15	$(C_2H_4)_n$	5.94±0.12
Ne	0.06±0.00	$(C_2H_4)_n$	9.94±0.21
Ne	3.04±0.00	$(C_2H_4)_n$	12.41±0.26
Ne	5.94±0.01	$(C_2H_4)_n$	14.64±0.30
Ne	8.83±0.01	$(C_2H_4)_n$	17.92±0.37
Ne	14.61±0.02	$(C_2H_4)_n$	20.39±0.42
Ne	29.06±0.04	$(C_2H_4)_n$	22.85±0.47
Al	4.98±0.10	$(C_2H_4)_n$	24.09±0.50
Al	8.64±0.20	$(C_2H_4)_n$	32.79±0.68
Al	13.71±0.30	$(C_2H_4)_n$	40.77±0.85
Al	22.16±0.46	$(C_2H_4)_n$	51.70±1.07

Table A.1: List of measured target materials with their thicknesses.

Material	x [mg/cm^2]	Material	$x\pm$ [mg/cm^2]
$(C_2H_4)_n$	61.64±1.28	$(C_3H_6)_n$	30.33±0.63
$(C_2H_4)_n$	69.62±1.45	$(C_3H_6)_n$	38.22±0.79
$(C_3H_6)_n$	0.52±0.01	$(C_3H_6)_n$	45.34±0.94
$(C_3H_6)_n$	1.33±0.03	$(C_3H_6)_n$	49.85±1.04
$(C_3H_6)_n$	1.85±0.04	C_2H_4	0.52±0.00
$(C_3H_6)_n$	2.66±0.05	C_2H_4	2.10±0.01
$(C_3H_6)_n$	3.99±0.08	C_2H_4	5.05±0.02
$(C_3H_6)_n$	4.51±0.09	C_2H_4	7.91±0.03
$(C_3H_6)_n$	5.84±0.12	C_2H_4	10.64±0.03
$(C_3H_6)_n$	9.03±0.19	C_2H_4	17.09±0.06
$(C_3H_6)_n$	13.54±0.28	C_2H_4	22.66±0.07
$(C_3H_6)_n$	16.92±0.35	C_2H_4	28.31±0.09
$(C_3H_6)_n$	21.30±0.44	C_2H_4	35.39±0.12
$(C_3H_6)_n$	22.63±0.47	C_2H_4	46.05±0.15

Table A.2: List of measured target materials with their thicknesses.

A.2 Fractions

Material	x [mg/cm^2]	$N(Ni^{27+})/(N(Ni^{27+}) + N(Ni^{28+}))$
C	4.10±0.04	0.2641±0.0018
C	6.31±0.02	0.1080±0.0014
C	10.41±0.06	0.0294±0.0004
C	23.54±0.37	0.0020±0.0001
C	32.13±0.36	0.0018±0.0001
N_2	0.06±0.00	0.7387±0.0017
N_2	0.92±0.00	0.5764±0.0033
N_2	3.72±0.01	0.2640±0.0022
N_2	9.87±0.02	0.0453±0.0010
N_2	19.49±0.04	0.0052±0.0001
N_2	29.17±0.06	0.0026±0.0001
N_2	38.72±0.08	0.0025±0.0001
N_2	67.65±0.15	0.0025±0.0001

Table A.3: Measured charge-state fraction of 200 MeV/u Ni^{27+} after penetration of targets with various thicknesses.

Material	x [mg/cm^2]	$N(Ni^{27+})/(N(Ni^{27+})+N(Ni^{28+}))$	$N(Ni^{27+})/(N(Ni^{27+})+N(Ni^{28+}))$
Ne	0.06±0.00	0.7310±0.0017	-
Ne	3.04±0.00	0.2404±0.0013	-
Ne	5.94±0.01	0.0810±0.0009	-
Ne	8.83±0.01	0.0269±0.0006	-
Ne	14.61±0.02	0.0047±0.0001	-
Ne	29.06±0.04	0.0022±0.0001	-
Al	4.98±0.10	0.0364±0.0005	-
Al	8.64±0.20	0.0046±0.0001	-
Al	13.71±0.30	0.0016±0.0001	-
Al	22.16±0.46	0.0015±0.0001	-
Ti	0.54±0.01	0.5884±0.0015	-
Ti	0.83±0.02	0.4262±0.0016	-
Ti	1.31±0.03	0.2530±0.0011	-
Ti	2.20±0.05	0.0975±0.0008	-
Ti	5.23±0.17	0.0058±0.0001	-
Ti	8.78±0.14	0.0031±0.0001	-
Ti	14.01±0.31	0.0029±0.0001	-
$(C_2H_4)_n$	1.24±0.03	0.6893±0.0019	0.0007±0.0001
$(C_2H_4)_n$	2.47±0.05	0.4707±0.0020	0.0012±0.0001
$(C_2H_4)_n$	3.71±0.08	0.3344±0.0016	0.0015±0.0001
$(C_2H_4)_n$	5.94±0.12	0.1716±0.0012	0.0018±0.0001
$(C_2H_4)_n$	9.94±0.21	0.0536±0.0006	0.0022±0.0002
$(C_2H_4)_n$	12.41±0.26	0.0270±0.0005	0.0020±0.0002
$(C_2H_4)_n$	14.64±0.30	0.0143±0.0004	0.0022±0.0002
$(C_2H_4)_n$	17.92±0.37	0.0071±0.0002	0.0022±0.0002
$(C_2H_4)_n$	20.39±0.42	0.0044±0.0002	0.0023±0.0002
$(C_2H_4)_n$	22.85±0.47	0.0033±0.0002	0.0020±0.0002
$(C_2H_4)_n$	24.09±0.50	0.0030±0.0002	0.0021±0.0002
$(C_2H_4)_n$	32.79±0.68	0.0021±0.0002	0.0025±0.0001
$(C_2H_4)_n$	40.77±0.85	0.0026±0.0001	0.0027±0.0001
$(C_2H_4)_n$	51.70±1.07	0.0030±0.0001	0.0022±0.0002

Table A.4: Measured charge-state fraction of Ni^{27+} after penetration of targets with various thicknesses with an incident 200 MeV/u Ni^{27+} beam (third column) and an incident 200 MeV/u Ni^{28+} beam (fourth column), respectively.

Material	x [mg/cm^2]	$N(\mathrm{Ni}^{27+})/(N(\mathrm{Ni}^{27+})+N(\mathrm{Ni}^{28+}))$	$N(\mathrm{Ni}^{27+})/(N(\mathrm{Ni}^{27+})+N(\mathrm{Ni}^{28+}))$
$(C_2H_4)_n$	61.64±1.28	0.0030±0.0002	0.0027±0.0002
$(C_2H_4)_n$	69.62±1.45	0.0030±0.0002	0.0023±0.0002
$(C_3H_6)_n$	0.52±0.01	0.8734±0.0009	0.0004±0.0001
$(C_3H_6)_n$	1.33±0.03	0.6912±0.0017	0.0008±0.0001
$(C_3H_6)_n$	1.85±0.04	0.6013±0.0021	0.0010±0.0001
$(C_3H_6)_n$	2.66±0.05	0.4773±0.0023	0.0013±0.0001
$(C_3H_6)_n$	3.99±0.08	0.3242±0.0023	0.0016±0.0001
$(C_3H_6)_n$	4.51±0.09	0.2833±0.0021	0.0017±0.0001
$(C_3H_6)_n$	5.84±0.12	0.1987±0.0023	0.0019±0.0001
$(C_3H_6)_n$	9.03±0.19	0.0835±0.0012	0.0019±0.0001
$(C_3H_6)_n$	13.54±0.28	0.0192±0.0004	0.0022±0.0001
$(C_3H_6)_n$	16.92±0.35	0.0081±0.0002	0.0025±0.0001
$(C_3H_6)_n$	21.30±0.44	0.0039±0.0002	0.0021±0.0001
$(C_3H_6)_n$	22.63±0.47	0.0033±0.0002	0.0023±0.0001
$(C_3H_6)_n$	30.33±0.63	0.0023±0.0001	0.0023±0.0001
$(C_3H_6)_n$	38.22±0.79	0.0022±0.0001	0.0023±0.0002
$(C_3H_6)_n$	45.34±0.94	0.0021±0.0001	0.0026±0.0002
$(C_3H_6)_n$	49.85±1.04	0.0023±0.0001	0.0025±0.0002
C_2H_4	0.52±0.00	0.8811±0.0009	0.0005±0.0000
C_2H_4	2.10±0.01	0.6216±0.0008	0.0012±0.0001
C_2H_4	5.05±0.02	0.3256±0.0006	0.0019±0.0001
C_2H_4	7.91±0.03	0.1663±0.0005	0.0025±0.0001
C_2H_4	10.64±0.03	0.0883±0.0004	0.0028±0.0001
C_2H_4	17.09±0.06	0.0206±0.0002	0.0027±0.0001
C_2H_4	22.66±0.07	0.0080±0.0001	0.0030±0.0001
C_2H_4	28.31±0.09	0.0041±0.0001	0.0031±0.0001
C_2H_4	35.39±0.12	0.0032±0.0001	0.0030±0.0001
C_2H_4	46.05±0.15	0.0029±0.0001	0.0030±0.0001

Table A.5: Measured charge-state fraction of Ni^{27+} after penetration of targets with various thicknesses with an incident 200 MeV/u Ni^{27+} beam (third column) and an incident 200 MeV/u Ni^{28+} beam (fourth column), respectively.

A.3 Capture Cross Sections

Material	Incident Charge	σ_c [cm^2]
C	27+	$1.21 \cdot 10^{-23} \pm 0.03 \cdot 10^{-23}$
N_2	27+	$1.63 \cdot 10^{-23} \pm 0.05 \cdot 10^{-23}$
Ne	27+	$2.71 \cdot 10^{-23} \pm 0.10 \cdot 10^{-23}$
Al	27+	$4.49 \cdot 10^{-23} \pm 0.15 \cdot 10^{-23}$
Ti	27+	$2.45 \cdot 10^{-22} \pm 0.55 \cdot 10^{-23}$
Ti*	27+	$2.39 \cdot 10^{-22} \pm 1.03 \cdot 10^{-23}$
Ti*	28+	$2.55 \cdot 10^{-22} \pm 1.59 \cdot 10^{-23}$
$(C_2H_4)_n$	27+	$2.87 \cdot 10^{-23} \pm 0.08 \cdot 10^{-23}$
$(C_2H_4)_n$	28+	$2.95 \cdot 10^{-23} \pm 0.21 \cdot 10^{-23}$
$(C_3H_6)^*_n$	27+	$4.48 \cdot 10^{-23} \pm 0.14 \cdot 10^{-23}$
$(C_3H_6)^*_n$	28+	$4.66 \cdot 10^{-23} \pm 0.20 \cdot 10^{-23}$
C_2H_4	27+	$2.89 \cdot 10^{-23} \pm 0.05 \cdot 10^{-23}$
C_2H_4	28+	$3.21 \cdot 10^{-23} \pm 0.23 \cdot 10^{-23}$

Table A.6: List of experimental capture cross sections for nickel ions at 200 MeV/u. The experimental errors correspond to one standard deviation. The marked data (*) are remeasured a year after the first experiment.

A.4 Ionization Cross Sections and Mean Free Path Length

Material	Incident Charge	σ_l [cm^2]
C	27+	$6.87 \cdot 10^{-21} \pm 0.03 \cdot 10^{-21}$
N_2	27+	$6.56 \cdot 10^{-21} \pm 0.03 \cdot 10^{-21}$
Ne	27+	$1.27 \cdot 10^{-20} \pm 0.01 \cdot 10^{-20}$
Al	27+	$3.01 \cdot 10^{-20} \pm 0.05 \cdot 10^{-20}$
Ti	27+	$8.32 \cdot 10^{-20} \pm 0.08 \cdot 10^{-20}$
Ti*	27+	$8.68 \cdot 10^{-20} \pm 0.09 \cdot 10^{-20}$
Ti*	28+	$9.10 \cdot 10^{-20} \pm 0.67 \cdot 10^{-20}$
$(C_2H_4)_n$	27+	$1.39 \cdot 10^{-20} \pm 0.01 \cdot 10^{-20}$
$(C_2H_4)_n$	28+	$1.28 \cdot 10^{-20} \pm 0.11 \cdot 10^{-20}$
$(C_3H_6)^*_n$	27+	$2.06 \cdot 10^{-20} \pm 0.01 \cdot 10^{-20}$
$(C_3H_6)^*_n$	28+	$2.03 \cdot 10^{-20} \pm 0.10 \cdot 10^{-20}$
C_2H_4	27+	$1.07 \cdot 10^{-20} \pm 0.01 \cdot 10^{-21}$
C_2H_4	28+	$1.08 \cdot 10^{-20} \pm 0.09 \cdot 10^{-20}$

Table A.7: List of experimental capture cross sections for nickel ions at 200 MeV/u. The experimental errors correspond to one standard deviation. The marked data (*) are remeasured a year after the first experiment.

Material	x [mg/cm^2] Thickness	ρ [mg/cm^3] Density	N [atoms/cm^3]	$\lambda_{27^+\to 28^+}$ [mg/cm^2] Loss	$\lambda_{28^+\to 27^+}$ [mg/cm^2] Capture	$\lambda_{1s\to 2s+2p}$ [mg/cm^2] Excitation
C	4.10–32.13	$2.27 \cdot 10^{3}$	$1.14 \cdot 10^{23}$	2.90	$1.65 \cdot 10^{3}$	6.78
N_2	0.06	$1.79 \cdot 10^{-3}$	$7.70 \cdot 10^{16}$	3.55	$1.43 \cdot 10^{3}$	6.29
N_2	0.92	$2.96 \cdot 10^{-2}$	$1.27 \cdot 10^{18}$	3.55	$1.43 \cdot 10^{3}$	6.29
N_2	3.72	$1.19 \cdot 10^{-1}$	$5.13 \cdot 10^{18}$	3.55	$1.43 \cdot 10^{3}$	6.29
N_2	9.87	$3.16 \cdot 10^{-1}$	$1.36 \cdot 10^{19}$	3.55	$1.43 \cdot 10^{3}$	6.29
N_2	19.49	$6.25 \cdot 10^{-1}$	$2.69 \cdot 10^{19}$	3.55	$1.43 \cdot 10^{3}$	6.29
N_2	29.17	$9.35 \cdot 10^{-1}$	$4.02 \cdot 10^{19}$	3.55	$1.43 \cdot 10^{3}$	6.29
N_2	38.72	1.24	$5.34 \cdot 10^{19}$	3.55	$1.43 \cdot 10^{3}$	6.29
N_2	67.65	2.17	$9.32 \cdot 10^{19}$	3.55	$1.43 \cdot 10^{3}$	6.29
Ne	0.06	$2.06 \cdot 10^{-3}$	$6.16 \cdot 10^{16}$	2.64	$1.23 \cdot 10^{3}$	4.80
Ne	3.04	$9.75 \cdot 10^{-2}$	$2.91 \cdot 10^{18}$	2.64	$1.23 \cdot 10^{3}$	4.80
Ne	5.94	$1.90 \cdot 10^{-1}$	$5.68 \cdot 10^{18}$	2.64	$1.23 \cdot 10^{3}$	4.80
Ne	8.83	$2.83 \cdot 10^{-1}$	$8.44 \cdot 10^{18}$	2.64	$1.23 \cdot 10^{3}$	4.80
Ne	14.61	$4.68 \cdot 10^{-1}$	$1.40 \cdot 10^{19}$	2.64	$1.23 \cdot 10^{3}$	4.80
Ne	29.06	$9.31 \cdot 10^{-1}$	$2.78 \cdot 10^{19}$	2.64	$1.23 \cdot 10^{3}$	4.80
Al	4.98–22.16	$2.70 \cdot 10^{3}$	$6.02 \cdot 10^{22}$	1.49	$9.97 \cdot 10^{2}$	4.45
Ti	0.54–25.86	$4.51 \cdot 10^{3}$	$5.67 \cdot 10^{22}$	0.96	$3.24 \cdot 10^{2}$	2.74
$(C_2H_4)_n$	1.24–69.62	$9.20 \cdot 10^{2}$	$1.97 \cdot 10^{22}$	3.34	$1.63 \cdot 10^{3}$	-
$(C_3H_6)_n$	0.54–49.85	$9.10 \cdot 10^{2}$	$1.30 \cdot 10^{22}$	3.39	$1.56 \cdot 10^{3}$	-
C_2H_4	0.52	$1.67 \cdot 10^{-2}$	$3.59 \cdot 10^{17}$	4.35	$1.61 \cdot 10^{3}$	-
C_2H_4	2.09	$6.73 \cdot 10^{-2}$	$1.44 \cdot 10^{18}$	4.35	$1.61 \cdot 10^{3}$	-
C_2H_4	5.04	$1.62 \cdot 10^{-1}$	$3.47 \cdot 10^{18}$	4.35	$1.61 \cdot 10^{3}$	-
C_2H_4	7.91	$2.54 \cdot 10^{-1}$	$5.45 \cdot 10^{18}$	4.35	$1.61 \cdot 10^{3}$	-
C_2H_4	10.64	$3.41 \cdot 10^{-1}$	$7.32 \cdot 10^{18}$	4.35	$1.61 \cdot 10^{3}$	-
C_2H_4	17.09	$5.48 \cdot 10^{-1}$	$1.18 \cdot 10^{19}$	4.35	$1.61 \cdot 10^{3}$	-
C_2H_4	22.66	$7.26 \cdot 10^{-1}$	$1.56 \cdot 10^{19}$	4.35	$1.61 \cdot 10^{3}$	-
C_2H_4	28.31	$9.07 \cdot 10^{-1}$	$1.95 \cdot 10^{19}$	4.35	$1.61 \cdot 10^{3}$	-
C_2H_4	35.39	1.13	$2.44 \cdot 10^{19}$	4.35	$1.61 \cdot 10^{3}$	-
C_2H_4	46.05	1.48	$3.17 \cdot 10^{19}$	4.35	$1.61 \cdot 10^{3}$	-

Table A.8: List of free mean path lengths λ_i for ionization (column 5), capture (column 6) and excitation (column 7), calculated with equation (5.1) and the tables presented in Appendix A.1, A.2 and D compared with the target thicknesses used in the experiment. The length of the gas call was 31.2 cm.

Appendix B

Uranium Data (Mean Charge)

B.1 Mean Charges of Uranium at (60.23 & 85.00) MeV/u

Material	x [mg/cm^2]	q_{mean}	Material	x [mg/cm^2]	q_{mean}
C	6.31±0.02	87.30±0.01	Ar	5.30±0.01	81.12±0.38
C	8.20±0.10	87.39±0.03	Ar	15.41±0.02	80.77±0.41
C	16.49±0.26	87.70±0.03	Ar	35.62±0.04	80.08±0.46
N_2	5.53±0.01	86.06±0.07	Ar	50.78±0.06	79.49±0.51
N_2	15.43±0.03	85.71±0.09	Ti	5.23±0.17	84.13±0.01
N_2	25.00±0.05	86.27±0.06	Ti	8.78±0.14	84.03±0.01
N_2	42.72±0.09	84.80±0.13	Ti	14.01±0.31	83.90±0.01
Ne	1.41±0.00	85.29±0.11	Ti	25.86±0.44	83.66±0.01
Ne	15.40±0.02	83.53±0.21	Ti	45.22±0.78	83.31±0.02
Ne	28.13±0.04	82.83±0.26	Cu	10.89±0.23	84.04±0.01
Ne	43.22±0.06	81.82±0.33	Cu	17.07±0.35	83.87±0.01
Al	4.98±0.10	85.75±0.01	Cu	30.34±0.63	83.54±0.02
Al	8.64±0.20	85.57±0.01	Cu	43.82±0.90	83.16±0.02
Al	22.16±0.46	85.07±0.02	Kr	8.00±0.00	80.47±0.43
Al	37.44±1.00	84.44±0.04	Kr	11.22±0.00	80.46±0.43

Table B.1: Measured mean charge states for incident 60.23 MeV/u U^{86+} ions in different target thicknesses.

Material	x [mg/cm^2]	q_{mean}	Material	x [mg/cm^2]	q_{mean}
Kr	32.47±0.01	79.94±0.48	Xe	17.64±0.01	79.67±0.50
Kr	53.83±0.01	79.33±0.62	Xe	67.54±0.04	77.36±0.71
Ag	11.03±0.29	83.69±0.01	Au	13.69±0.28	82.90±0.01
Ag	17.59±0.43	83.53±0.01	Au	22.13±0.46	82.70±0.01
Ag	35.80±0.74	83.07±0.02	Au	39.67±0.82	82.42±0.02
Ag	52.88±1.42	82.63±0.04	Au	65.01±1.34	81.74±0.03
Xe	9.38±0.01	79.81±0.50			

Table B.2: Measured mean charge states for incident 60.23 MeV/u U^{86+} ions in different target thicknesses.

Material	x [mg/cm^2]	q_{mean}	Material	x [mg/cm^2]	q_{mean}
$(C_3H_6)_n$	0.52±0.01	86.10±0.00	C_2H_4	3.71±0.01	86.18±0.07
$(C_3H_6)_n$	4.51±0.09	86.75±0.00	C_2H_4	10.82±0.04	86.36±0.06
$(C_3H_6)_n$	16.92±0.35	87.28±0.01	C_2H_4	25.06±0.08	86.78±0.04
$(C_3H_6)_n$	21.30±0.44	87.22±0.01	C_2H_4	35.79±0.12	87.06±0.03
$(C_3H_6)_n$	38.22±0.79	87.53±0.03	C_2H_4	39.42±0.13	87.83±0.01
C_2H_4	0.45±0.00	85.92±0.08			

Table B.3: Measured mean charge states for incident 60.23 MeV/u U^{86+} ions in different target thicknesses.

Material	x [mg/cm^2]	q_{mean}	Material	x [mg/cm^2]	q_{mean}
Be	4.50±0.07	82.81±0.05	Be	36.66±0.74	88.46±0.11
Be	9.32±0.15	85.08±0.07	C	7.54±0.12	85.94±0.05
Be	13.61±0.22	86.23±0.04	C	8.20±0.10	86.28±0.05
Be	17.68±0.28	86.93±0.05	C	16.49±0.26	88.06±0.06

Table B.4: Measured mean charge states for incident 85.00 MeV/u U^{73+} ions in different target thicknesses.

Appendix C

Uranium Data (Energy Loss)

C.1 Energy Losses of Uranium

Material	x [mg/cm^2]	E_{in} [MeV/u]	ΔE [MeV]
Be	6.98±0.14	60.23	416.50±11.30
Be	11.48±0.38	60.23	704.48±24.96
Be	22.19±0.45	60.23	1366.12±28.88
Be	36.66±0.74	60.23	2291.94±46.82
Be	4.50±0.07	85.00	208.85±3.36
Be	9.32±0.15	85.00	416.02±8.85
Be	13.61±0.22	85.00	624.75±11.26
Be	17.68±0.28	85.00	796.51±14.43
Be	22.19±0.45	85.00	1024.19±21.07
Be	36.66±0.74	85.00	1723.12±34.79
C	6.31±0.02	60.23	441.09±7.60
C	8.20±0.10	60.23	562.87±9.07
C	16.49±0.26	60.23	1117.01±18.47
C	7.54±0.12	85.00	352.24±7.62
C	8.20±0.10	85.00	407.77±6.31
C	13.18±0.30	85.00	621.18±16.70
C	16.49±0.26	85.00	832.21±14.48
C	23.32±0.38	85.00	1218.56±21.00
C	23.54±0.37	85.00	1225.70±22.32
C	32.13±0.36	85.00	1718.36±20.13

Table C.1: Experimental energy loss data (ΔE) for uranium ions penetrating various gases and solids. The target thicknesses are given in column 2 and the incident energy in column 3.

Material	x [mg/cm^2]	E_{in} [MeV/u]	ΔE [MeV]
N_2	5.53±0.01	60.23	360.17±17.07
N_2	15.43±0.03	60.23	1018.64±17.19
N_2	25.00±0.05	60.23	1393.09±17.35
N_2	42.72±0.09	60.23	2660.05±17.75
Ne	1.41±0.00	60.23	84.89±31.49
Ne	15.40±0.02	60.23	899.64±31.68
Ne	28.13±0.04	60.23	1660.65±31.73
Ne	43.22±0.06	60.23	2600.15±31.74
Ne	2.75±0.00	199.99	28.56±25.80
Ne	7.85±0.01	199.99	138.04±25.85
Ne	12.95±0.02	199.99	326.06±25.78
Ne	20.59±0.03	199.99	511.70±25.92
Al	4.98±0.10	60.23	289.89±9.62
Al	8.64±0.20	60.23	496.23±13.76
Al	22.16±0.46	60.23	1263.19±28.10
Al	37.44±1.00	60.23	2218.16±59.45
Al	4.98±0.10	199.99	188.02±13.27
Al	8.64±0.20	199.99	292.74±13.49
Al	13.71±0.30	199.99	426.02±14.55
Ar	5.30±0.01	60.23	259.90±17.18
Ar	15.41±0.02	60.23	732.25±17.09
Ar	35.62±0.04	60.23	1715.50±17.06
Ar	50.78±0.06	60.23	2480.91±17.12
Ar	2.93±0.00	199.99	19.04±25.80
Ar	7.98±0.01	199.99	111.86±25.83
Ar	13.03±0.02	199.99	283.22±25.81
Ar	20.59±0.03	199.99	454.58±25.83

Table C.2: Experimental energy loss data (ΔE) for uranium ions penetrating various gases and solids. The target thicknesses are given in column 2 and the incident energy in column 3.

Material	x [mg/cm^2]	E_{in} [MeV/u]	ΔE [MeV]
Ti	5.23±0.17	60.23	258.23±11.29
Ti	8.78±0.14	60.23	442.02±10.13
Ti	14.01±0.31	60.23	707.65±17.33
Ti	25.86±0.44	60.23	1295.91±23.39
Ti	45.22±0.78	60.23	2281.23±40.12
Ti	0.54±0.01	199.99	59.50±12.14
Ti	1.31±0.03	199.99	71.40±12.14
Ti	2.20±0.05	199.99	88.06±12.16
Ti	5.23±0.17	199.99	185.64±13.82
Cu	10.89±0.23	60.23	535.50±12.54
Cu	17.07±0.35	60.23	821.89±18.04
Cu	30.34±0.63	60.23	1453.39±30.59
Cu	43.82±0.90	60.23	2104.71±43.56
Kr	8.00±0.00	60.23	318.92±17.06
Kr	11.22±0.00	60.23	446.85±17.07
Kr	32.47±0.01	60.23	1299.48±16.96
Kr	53.83±0.01	60.23	2383.17±16.83
Ag	11.03±0.29	60.23	456.36±14.87
Ag	17.59±0.43	60.23	737.21±20.16
Ag	35.80±0.74	60.23	1480.36±33.35
Ag	52.88±1.42	60.23	2305.63±62.69

Table C.3: Experimental energy loss data (ΔE) for uranium ions penetrating various gases and solids. The target thicknesses are given in column 2 and the incident energy in column 3.

Material	x [mg/cm^2]	E_{in} [MeV/u]	ΔE [MeV]
Xe	9.38±0.01	60.23	333.20±17.08
Xe	17.64±0.01	60.23	624.75±17.04
Xe	42.60±0.03	60.23	1532.72±16.93
Xe	52.92±0.03	60.23	2153.90±17.08
Xe	67.54±0.04	60.23	2740.97±16.90
Au	13.69±0.28	60.23	471.84±11.84
Au	22.13±0.46	60.23	750.89±17.21
Au	39.67±0.82	60.23	1339.94±29.35
Au	65.01±1.34	60.23	2263.38±47.24
$(C_3H_6)_n$	0.52±0.01	60.23	35.7±7.76
$(C_3H_6)_n$	1.33±0.03	60.23	138.04±7.81
$(C_3H_6)_n$	2.66±0.05	60.23	207.06±8.49
$(C_3H_6)_n$	4.51±0.09	60.23	349.38±9.62
$(C_3H_6)_n$	9.03±0.19	60.23	749.70±16.20
$(C_3H_6)_n$	16.92±0.35	60.23	1330.90±28.23
$(C_3H_6)_n$	21.30±0.44	60.23	1692.97±34.87
$(C_3H_6)_n$	38.22±0.79	60.23	2949.61±61.72
$(C_3H_6)_n$	0.52±0.01	199.99	41.65±11.41
$(C_3H_6)_n$	1.33±0.03	199.99	69.02±12.24
$(C_3H_6)_n$	1.85±0.04	199.99	102.34±12.46
$(C_3H_6)_n$	2.66±0.05	199.99	118.41±12.62
$(C_3H_6)_n$	3.99±0.09	199.99	166.60±13.11
$(C_3H_6)_n$	5.84±0.12	199.99	222.93±13.74
$(C_3H_6)_n$	9.03±0.19	199.99	342.72±14.40
$(C_3H_6)_n$	16.92±0.35	199.99	597.38±17.97
$(C_3H_6)_n$	30.33±0.63	199.99	1130.50±25.56

Table C.4: Experimental energy loss data (ΔE) for uranium ions penetrating various gases and solids. The target thicknesses are given in column 2 and the incident energy in column 3.

Material	x [mg/cm^2]	E_{in} [MeV/u]	ΔE [MeV]
C_2H_4	0.45±0.00	60.23	49.39±17.25
C_2H_4	3.71±0.01	60.23	298.10±17.04
C_2H_4	10.82±0.04	60.23	869.59±17.19
C_2H_4	25.06±0.08	60.23	1775.88±17.78
C_2H_4	35.79±0.12	60.23	2474.81±18.55
C_2H_4	39.42±0.13	60.23	2591.82±18.78
C_2H_4	2.17±0.01	199.99	11.90±26.00
C_2H_4	4.3±0.01	199.99	864.26±26.16
C_2H_4	6.56±0.02	199.99	145.97±26.58
C_2H_4	9.03±0.03	199.99	226.10±25.86
C_2H_4	13.86±0.05	199.99	383.18±26.26
C_2H_4	18.77±0.06	199.99	591.43±26.44
C_2H_4	23.61±0.08	199.99	768.74±25.95
C_2H_4	28.47±0.09	199.99	947.24±26.48

Table C.5: Experimental energy loss data (ΔE) for uranium ions penetrating various gases and solids. The target thicknesses are given in column 2 and the incident energy in column 3.

C.2 Stopping Forces of Uranium Ions at 60.23 MeV/u

Material	E [MeV/u]	$x_{\min} - x_{\max}$ [mg/cm^2]	$-dE/dx$ [MeV/(mg/cm^2)]
Be	57.72	6.98±0.14 – 36.66±0.74	63.07±0.35
C	58.74	6.31±0.02 – 16.49±0.26	66.50±1.37
N_2	57.38	5.53±0.01 – 42.72±0.09	60.79±1.93
Ne	57.48	1.41±0.00 – 43.22±0.06	59.89±0.34
Al	57.99	4.98±0.10 – 37.44±1.00	59.08±0.46
Ar	57.59	5.30±0.01 – 50.78±0.06	48.87±0.18
Ti	58.14	5.23±0.17 – 45.22±0.78	50.52±0.09
Cu	57.37	10.89±0.23 – 43.82±0.90	47.69±0.16
Kr	58.36	8.00±0.00 – 53.83±0.01	44.24±0.74
Ag	57.61	11.03±0.29 – 52.88±1.42	43.86±0.48
Xe	57.13	9.38±0.01 – 67.54±0.04	41.34±0.77
Au	57.70	13.69±0.28 – 65.01±1.34	34.85±0.25
$(C_3H_6)_n$	58.27	0.52±0.01 – 38.22±0.79	77.65±0.54
C_2H_4	57.76	0.45±0.00 – 39.42±0.13	66.40±0.97

Table C.6: Experimental stopping forces (dE/dx) for incident U^{86+} ions at 60.23 MeV/u with the target thickness ranges (column 3) covered in the experiment. These data are shown in figure 4.8 and compared to theory in figure 5.4.

C.3 Stopping Forces of Uranium Ions at (85.00 & 199.99) MeV/u

Material	E [MeV/u]	$x_{\min} - x_{\max}$ [mg/cm^2]	$-dE/dx$ [MeV/(mg/cm^2)]
Be	83.34	4.50±0.07 – 36.66±0.74	47.18±0.60
C	83.09	7.54±0.12 – 32.13±0.36	54.75±1.10
Ne	199.46	2.75±0.00 – 20.59±0.03	27.49±1.23
Al	199.36	4.98±0.10 – 13.71±0.30	27.20±0.65
Ar	199.53	2.93±0.00 – 20.59±0.03	25.42±1.77
Ti	199.78	0.54±0.01 – 5.23±0.17	27.75±2.61
$(C_3H_6)_n$	199.34	0.52±0.01 – 30.33±0.63	36.05±0.44
C_2H_4	199.10	0.37±0.00 – 28.47±0.09	35.93±0.57

Table C.7: Experimental stopping forces (dE/dx) for incident U^{73+} ions at 85 MeV/u (C and Be) and for incident U^{81+} ions at 200.6 MeV/u with the target thickness ranges (column 3) covered in the experiment.

Appendix D

Theoretical Charge-Exchange Cross Sections

	$Z_2 = 6$	$Z_2 = 7$	$Z_2 = 10$	$Z_2 = 13$	$Z_2 = 22$
$\sigma^{exc}_{1s\to 2s}$	$3.04 \cdot 10^{-22}$	$4.02 \cdot 10^{-22}$	$7.82 \cdot 10^{-22}$	$1.23 \cdot 10^{-21}$	$3.44 \cdot 10^{-21}$
$\sigma^{exc}_{1s\to 2p}$	$3.82 \cdot 10^{-21}$	$4.80 \cdot 10^{-21}$	$9.05 \cdot 10^{-21}$	$1.30 \cdot 10^{-20}$	$3.76 \cdot 10^{-20}$
σ^{ion}_{1s}	$5.26 \cdot 10^{-21}$	6.74×10^{-21}	$1.28 \cdot 10^{-20}$	$2.36 \cdot 10^{-20}$	$6.75 \cdot 10^{-20}$
σ^{ion}_{2s}	$1.66 \cdot 10^{-20}$	$2.16 \cdot 10^{-20}$	$3.19 \cdot 10^{-20}$	$6.62 \cdot 10^{-20}$	$1.74 \cdot 10^{-19}$
σ^{ion}_{2p}	$1.99 \cdot 10^{-20}$	$2.59 \cdot 10^{-20}$	$3.82 \cdot 10^{-20}$	$7.94 \cdot 10^{-20}$	$2.07 \cdot 10^{-19}$
σ_l	$5.76 \cdot 10^{-21}$	$6.75 \cdot 10^{-21}$	$1.28 \cdot 10^{-20}$	$2.82 \cdot 10^{-20}$	$8.26 \cdot 10^{-20}$
σ^{REC}_{1s}	$1.01 \cdot 10^{-23}$	$1.18 \cdot 10^{-23}$	$1.67 \cdot 10^{-23}$	$2.18 \cdot 10^{-23}$	$3.69 \cdot 10^{-23}$
σ^{REC}_{2s}	$1.26 \cdot 10^{-24}$	$1.47 \cdot 10^{-24}$	$2.21 \cdot 10^{-24}$	$2.84 \cdot 10^{-24}$	$4.83 \cdot 10^{-24}$
σ^{REC}_{2p}	$1.36 \cdot 10^{-25}$	$1.58 \cdot 10^{-25}$	$2.31 \cdot 10^{-25}$	$3.06 \cdot 10^{-25}$	$5.14 \cdot 10^{-25}$
σ^{NRC}_{1s}	$1.24 \cdot 10^{-24}$	$2.58 \cdot 10^{-24}$	$1.54 \cdot 10^{-23}$	$6.00 \cdot 10^{-23}$	$7.06 \cdot 10^{-22}$
σ^{NRC}_{2s}	$0.98 \cdot 10^{-25}$	$1.96 \cdot 10^{-25}$	$1.15 \cdot 10^{-24}$	$0.44 \cdot 10^{-23}$	$4.70 \cdot 10^{-23}$
σ^{NRC}_{2p}	$2.95 \cdot 10^{-25}$	$5.88 \cdot 10^{-25}$	$3.46 \cdot 10^{-24}$	$1.31 \cdot 10^{-23}$	$1.41 \cdot 10^{-22}$
σ_c	$1.28 \cdot 10^{-23}$	$1.75 \cdot 10^{-23}$	$4.27 \cdot 10^{-23}$	$1.16 \cdot 10^{-22}$	$1.07 \cdot 10^{-21}$

Table D.1: Theoretical cross sections in cm^2 for excitation, ionization, REC and NRC of Ni^{27+} ions at 200 MeV/u calculated from various codes (see chapter 5 for discussion). The theoretical results are shown in figure 5.1 and 5.2.

Appendix E

Theoretical Stopping Forces

E.1 Theoretical Stopping Forces of Uranium Ions

Material	E [MeV/u]	q_{mean}	$-dE/dx$ [MeV/(mg/cm^2)]
Be	57.72	82.43 (TF)	55.64
C	58.74	87.26	65.69
N_2	57.38	86.10	65.30
Ne	57.48	84.35	57.70
Al	57.99	85.57	55.46
Ar	57.59	80.90	47.69
Ti	58.14	84.00	47.94
Cu	57.37	83.96	45.26
Kr	58.36	80.56	39.50
Ag	57.61	83.59	41.39
Xe	57.13	79.54	35.81
Au	57.70	82.83	33.11
$(C_3H_6)_n$	58.27	86.62	78.60
C_2H_4	57.76	86.20	78.45
Be	83.34	84.53	45.70
C	83.09	86.52	51.30
Ne	199.46	89.97 (TF)	30.35
Al	199.36	89.97 (TF)	28.94
Ar	199.53	89.97 (TF)	26.55
Ti	199.78	89.97 (TF)	26.06
$(C_3H_6)_n$	199.34	89.97 (TF)	38.91
C_2H_4	199.10	89.96 (TF)	38.93

Table E.1: List of theoretical stopping forces calculated with the PASS code. The experimental mean charge values are used as an input in this code. TF means that eq. (2.46) was used to calculate the mean charge. These theoretical results are shown in figure 5.4.

Bibliography

[1] A. Surzhykov, S. Fritzsche, Cross Section Calculations, private communications (2005).

[2] V. P. Shevelko, Cross Section Calculations, private communications (2005).

[3] P. Sigmund, A. Schinner, Europ. Phys. J. D 12 (2000) 425.

[4] P. Sigmund, A. Schinner, Nucl. Instr. and Meth. **B** 195 (2002) 64.

[5] H. Geissel, J. Kunzendorf, P. Malzacher, C. Scheidenberger, H. Weick, ATomic Interactions in MAtter, http://www-linux.gsi.de/∼weick/atima/, (2005).

[6] F. Hubert, R. Bimbot, H. Gauvin, Atomic Data & Nucl. Data Tables 46 (1990) 1.

[7] H. Geissel, Y. Laichter, W. F. W. Schneider, P. Armbruster, Phys. Lett. A 99 (1983) 77.

[8] N. O. Lassen, Mat. Fys. Medd. Dan. Vid. Selsk. 26 (5 & 12) (1951) 1.

[9] R. Bimbot, S. Barbey, T. Benfoughal, F. Clapier, M. Mirea, N. Pauwels, S. Pierre, M. F. Rivet, G. Fares, A. Hachem, R. Anne, Y. Georget, R. Hue, C. Tribouillard, Nucl. Instr. and Meth. **B** 107 (1996) 9.

[10] C. Scheidenberger, H. Geissel, H. H. Mikkelsen, F. Nickel, T. Brohm, H. Folger, H. Irnich, A. Magel, M. F. Mohar, G. Münzenberg, M. Pfützner, E. Roeckl, I. Schall, D. Schardt, K. H. Schmidt, W. Schwab, M. Steiner, T. Stöhlker, K. Sümmerer, D. J. Vieira, B. Voss, M. Weber, Phys. Rev. Lett. **73** (1994) 50.

[11] H. Geissel, C. Scheidenberger, Nucl. Instr. and Meth. **B** 136-138 (1998) 114.

[12] J. Lindhard, A. H. Sørensen, Phys. Rev. A **53** (1996) 2443.

[13] H. Weick, Ph.D. thesis, Einfluss der Umladung beim Abbremsen von Schwerionen im Energiebereich (100 - 1000) MeV/u, II. Physikalisches Institut, Justus-Liebig-Universität Gießen, (2000).

[14] N. Nankov, Ph.D. thesis, Untersuchung der Abbremsung von Schwerionen in Materie im Energiebereich (40 - 400) MeV/u, II. Physikalisches Institut, Justus-Liebig-Universität Gießen, (2002).

[15] M. Maier, Ph.D. thesis, New applications for slowing down of high-energy heavy ions, II. Physikalisches Institut, Justus-Liebig-Universität Gießen, (2004).

[16] C. J. Woods, C. J. Sofield, N. E. B. Cowern, M. Murrell, J. Draper, J. Phys. B: Mol. Phys. 17 (1984) 867.

[17] P. Sigmund, Charged-Particle Penetration and Radiation Effects : Introductory Theory (Chapters 1-4), Physics Department, Odense University, August (2000).

[18] J. J. Thomson, Philos. Mag. 23 (1912) 449.

[19] N. Bohr, Philos. Mag. 25 (1913) 10.

[20] M. Abramowitz, I. A. Stegun, Handbook of Mathematical Functions, Dover, New York, (1964).

[21] H. Bethe, Ann. Physik 5 (1930) 324.

[22] P. Sigmund, Phys. Rev. A **54** (1996) 3113.

[23] F. M. Smith, W. Birnbaum, W. H. Barkas, Phys. Rev. **91** (1953) 765.

[24] J. C. Ashley, R. H. Ritchie, W. Brandt, Phys. Rev. B **5** (1972) 2393.

[25] J. D. Jackson, R. L. McCarthy, Phys. Rev. B **6** (1972) 4131.

[26] J. Lindhard, Nucl. Instr. and Meth. 132 (1976) 1.

[27] A. Schinner, P. Sigmund, Nucl. Instr. and Meth. **B** 164-165 (2000) 220.

[28] J. A. Brinkman, J. Appl. Phys. **25** (1954) 961.

[29] G. Leibfried, Bestrahlungseffekte in Festkörpern, Teubner, Stuttgart, (1965).

[30] M. T. Robinson, Table of Classical Scattering Integrals, Tech. Rep. ORNL-4556 Oak Ridge National Laboratory, (1970).

[31] N. Bohr, Mat. Fys. Medd. Dan. Vid. Selsk. 18 (8) (1948) 1.

[32] P. Sigmund, Phys. Rev. A **56** (1997) 3681.

[33] W. Brandt, M. Kitagawa, Phys Rev. B **25** (1982) 5631.

[34] P. Sigmund, Phys. Rev. A **26** (1982) 2497.

[35] M. C. Walske, Phys. Rev. **88** (1952) 1283.

[36] M. C. Walske, Phys. Rev. **101** (1956) 940.

[37] P. Sigmund, Europ. Phys. J. D 12 (2000) 111.

[38] H. H. Andersen, H. Simonsen, H. Sørensen, Nucl. Phys. **A125** (1969) 171.

[39] K. W. Hill, E. Merzbacher, Phys. Rev. A **9** (1974) 156.

[40] H. H. Mikkelsen, P. Sigmund, Phys. Rev. A **40** (1989) 101.

[41] P. Sigmund, A. Schinner, Nucl. Instr. and Meth. **B** 212 (2003) 110.

[42] H. Bethe, Z. Phys. 76 (1932) 293.

[43] E. Clementi and C. Roetti, Atomic Data & Nucl. Data Tables 14 (1974) 177.

[44] F. Herman and S. Skillman, Atomic Structure Calculations, Prentice Hall, New Jersey, (1963).

[45] P. Sigmund, L. G. Glazov, Europ. Phys. J. D 23 (2003) 211.

[46] E. D. Palik, Electronic Handbook of Optical Constants of Solids - Version 1.0, SciVision, Academic Press, (2000).

[47] B. L. Henke, E. M. Gullikson, J. C. Davies, At. Data and Nucl. Data Tab. **54** (1993) 181.

[48] J. Berkowitz, Photoadsorption and Photoelectron Spectroscopy, Academic Press, New York, (1979).

[49] J. Berkowitz, Atomic and Molecular Photoadsorption, Absolute total cross sections, Academic Press, San Diego, (2002).

[50] G. Williams, Electron Binding Energies, http://xray.uu.se/hypertext/EBind Energies.html, (1995).

[51] M. Stobbe, Ann. Phys. **7** (1930) 661.

[52] A. Ichihara, T. Shirai, J. Eichler, Phys. Rev. A **49** (1994) 1875.

[53] R. Abrines, I. C. Percival, Proc. Phys. Soc. Lond. **88** (1966) 861.

[54] R. Abrines, I. C. Percival, Proc. Phys. Soc. Lond. **88** (1966) 873.

[55] V. P. Shevelko, Sov. Phys.-JETP **71** (2001) 20.

[56] Dž. Belkić, R. Gayet, A. Salin, Comput. Phys. Commun. 32 (1984) 385.

[57] W. E. Meyerhof, R. Anholt, J. Eichler, H. Gould, Ch. Munger, J. Alonso, P. Thieberger, H. E. Wegner, Phys. Rev. A **32** (1985) 3291.

[58] H.-D. Betz, Rev. Mod. Phys. **44** (1972) 465.

[59] S. K. Allison, Rev. Mod. Phys. **30** (1958) 1137.

[60] P. Sigmund, Nucl. Instr. and Meth. **B** 69 (1992) 113.

[61] N. Bohr, J. Lindhard, Mat. Fys. Medd. Dan. Vid. Selsk. 28 (7) (1954) 1.

[62] H.-D. Betz, L. Grodzin, Phys. Rev. Lett. **25** (1970) 211.

[63] P. Sigmund, A. Fettouhi, A. Schinner, Nucl. Instr. and Meth. **B** 209 (2003) 19.

[64] K. Blasche, D. Böhne, B. Franzke, H. Prange, IEEE Trans. on Nucl. Sci., Ns-32(5) (1985) 2657.

[65] H. Geissel, P. Armbruster, K.-H. Behr, A. Brünle, K. H. Burkhard *et al.*, Nucl. Instr. and Meth. **B** 70 (1992) 286.

[66] H. Wollnik, Optics of Charged Particles, Academic Press, Orlando, Florida, (1987).

[67] H. Wollnik, B. Hartmann, M. Berz, AIP Conference Proceedings; ed. C. R. Eminhizer, **177** (1988) 74.

[68] William R. Leo, Techniques for nuclear and particle physics experiments : a how-to approach, Springer, Berlin, (1987).

[69] R. C. Reid, J. M. Rausnitz, B. E. Poling, The Properties of Gases and Liquids, McGraw-Hill, New York, (1987).

[70] C. Scheidenberger, Th. Stöhlker, W. E. Meyerhof, H. Geissel, P. H. Mokler, B. Blank, Instr. and Meth. **B** 142 (1998) 441.

[71] D. Bazin, O. Tarasov, M. Lewitowicz, O. Sorlin, Instr. and Meth. **A** 482 (2002) 307.

[72] A. Surzhykov, S. Fritzsche, Lifetime Calculations, private communications (2004).

[73] A. Surzhykov, S. Fritzsche, Th. Stöhlker, J. Phys. B: At. Mol. Opt. Phys. **35** (2002) 3713.

[74] A. Surzhykov, S. Fritzsche, P. Koval, Comput. Phys. Commun. 165 (2005) 139.

[75] R. Anholt, Phys. Rev. A **31** (1985) 3579.

[76] A. B. Voitkiv, Phys. Rep. **392** (2004) 191.

[77] V. P. Shevelko, O. Rosmej, H. Tawara, I. Yu. Tolstikhina, J. Phys. B: At. Mol. Opt. Phys. **37** (2003) 201.

[78] J. P. Rozet, C. Stéphan, D. Vernhet, J. Phys. B: At. Mol. Opt. Phys. **35** (2002) 3713.

[79] A. Blazevic, Ph.D. thesis, Hochauflösende Schichtanalytik mit hochenergetischen schweren Ionen, Hahn-Meitner-Institut, Freien Universität Berlin, (1999).

[80] A. Fettouhi, H. Geissel, A. Schinner, P Sigmund, Nucl. Instr. and Meth. **B** 245 (2006) 22.

[81] T.E. Pierce, M. Blann, Phys. Rev. **173** (1968) 390.

Acknowledgement

First of all I want to thank Professor Hans Geissel for the opportunity to perform this experiment and to join the IONAS group at the II. Physikalisches Institut at the University of Gießen.

Secondly I thank Professor Peter Sigmund with him this work initially started and without him this work would not have been possible and for the fruitful discussions, suggestions and help with this work. Special thanks go to Ph. D. Mauricio Portillo and Dr. Hidemi Ogawa for their hard work and help in planning and setting up the experiments and for the pictures used throughout this thesis. Many thanks to Dr. Helmut Weick and Dipl. Phys. Ronja K. Knöbel for teaching me how to analyze the recorded data and for the fruitful discussions concerning the analysis and for taking the time to read my thesis and for providing the calculations done with the GICO code.

The group of people which are essential in any experiment at the FRS I especially mention here. These are the technicians at the FRS (Adolf Brünle, Karl-Heinz Behr and Karlheinz Burkard), the GSI workshop (Kalliopi Dermati and D. Henras) and the Target Lab staff (Birgit Kindler, Bettina Lommel and Jutta Steiner). Without them things such as preparation of targets, experimental setup, gas cell construction, gas supplies and much more would all not have smoothly gone. Many thanks to all the people from the IONAS group, FRS group and RISING group for participating the experiments and making it such a success and interesting experience.

A very special thanks to Dipl. Phys. Zheng Wang, Dipl. Phys. Martin Petrick, Dipl. Phys. Timo Dickel and Dr. Wolfgang R. Plaß for making my stay here in Gießen so enjoyable and for the interesting discussions (not always about physics) we have had.

A very very special thanks go out to my parents for making it possible for me to move to Germany and for their love and support especially during the rough times and to my brother and sister for being there when needed.